Title
Transcriptional Correlates of Homeostatic Plasticity and Neuronal Diversity at the Neuromuscular Junction

Author
Cypranowska, Caroline Amelia

Publication Date
2020

Peer reviewed|Thesis/dissertation

Transcriptional Correlates of Homeostatic Plasticity and Neuronal Diversity at the Neuromuscular Junction

By

Caroline A Cypranowska

A dissertation submitted in partial satisfaction of the

requirements for the degree of

Doctor of Philosophy

in

Molecular and Cell Biology

in the

Graduate Division

of the

University of California, Berkeley

Committee in charge:

Professor Ehud Y. Isacoff, Chair

Professor John Ngai

Professor Ahmet Yildiz

Professor Daniel Fletcher

Spring 2020

Abstract

Transcriptional Correlates of Homeostatic Plasticity and Neuronal Diversity at the Neuromuscular Junction

Caroline Amelia Cypranowska

Doctor of Philosophy in Molecular and Cell Biology

University of California, Berkeley

Professor Ehud Isacoff, Chair

Synapses are specialized intercellular junctions between a neuron and its target that allows for rapid communication between cells. Neurons and their synapses have multiple adaptive mechanisms to stabilize communication in response to a barrage of different environmental challenges. While there is an enormous body of literature on the mechanisms of these phenomena from a functional standpoint, less is known about (1) how these processes are orchestrated at the genetic level and (2) how differences in neuron type inform the capacity to enact such mechanisms.

To address these questions I turn to the *Drosophila* larval neuromuscular junction (NMJ). The *Drosophila* NMJ is a model glutamatergic synapse in which a motor neuron communicates with the body wall muscles to control motor output. Each muscle fiber receives input from two different types of glutamatergic neurons, each of which has unique physiological properties. Previous work has shown that blocking the receipt of glutamate by the downstream muscle by genetic mutation results in a retrograde homeostatic mechanism that potentiates synaptic transmission in a manner specific to neuronal subtype. The molecular and genetic determinants of this process are a mystery in the field, opening up even more questions about how gene expression can control a neuron's capacity to adapt to imbalances in network activity and synaptic strength.

In this dissertation, I use the tools of functional genomics to investigate different homeostatic mechanisms at this model synapse and to characterize transcriptional diversity within *Drosophila* larval motor neurons. First, I demonstrate that specific loss of key proteins in synaptic transmission in motor neurons induces homeostatic compensation, which features an increase in activity and altered expression of proteins that contribute to neuronal firing. Second, I show that mutation of a gene involved in the organization of the muscular cytomatrix mimics a classic model of presynaptic homeostatic potentiation. This new model also has alterations in cell-adhesion molecules which may be causal for this mode of homeostasis. Finally, I characterize the transcriptional diversity of glutamatergic motor neurons in this system, revealing that the expression of ion channels and activity regulated genes is correlated with temporal identity.

Table of Contents

Appendix 1: Identification of housekeeping genes in *Drosophila melanogaster* tissues for the normalization of RNA-sequencing data sets

List of Figures

Supplementary Figure 5.1 *p*-value distributions of edgeR and DESeq2 DE testing by normalization method

List of Tables

Acknowledgments

During my time in the Molecular and Cell Biology graduate program, I have had the honor of meeting and working with a lot of talented, hard-working, and supportive faculty, post-docs, graduate students and staff. I have gratitude for each person with whom I have interacted with along this intellectual journey. A graduate degree is not a solo venture, and each of you have helped me make this summit.

Firstly, I would like to thank the entire Molecular and Cell Biology graduate program, former head of the graduate program, Matt Welch, and the members of my committee, John Ngai, Ahmet Yildiz, and Dan Fletcher. Thank you for making time to advise me and guiding me through this phase of my academic career.

I owe a tremendous debt of gratitude to my dissertation advisor, Ehud Isacoff, for taking me on as a graduate student and supporting my scientific vision. Udi deserves my utmost appreciation for taking a chance on me, for giving me the freedom to blaze my own trail on good days and bad days, and helping me when I lost my way.

I would like to thank my peers in the Isacoff lab for your camaraderie and invaluable advice over these many long years. They are the best colleagues anyone can ask for. My comrades in the fly team, Zachary Newman, Adam Hoagland, Krisha Aghi, Dariya Bakshinskaya, Ryan Schultz, and Julia Bleier, deserve a special commendation for taking me seriously, pulling strings for last-minute favors, and making time to discuss free-wheeling scientific ideas. I owe thanks to undergraduate students, Nadia Rahimian and Shivali Baveja, for making me a better mentor and a better scientist. I will miss our lab's rowdy ski trips (and other adventures and misadventures outdoors) when I do move on to the next step of my career.

I have had the luck and pleasure of receiving support from friends and colleagues outside of the Isacoff lab. In particular, I'd thank Michael Sanchez, for rallying the troops and teaching me the meaning of discipline, Diya Das, for her friendship and helping me out when I've taken on more responsibilities than I thought I could manage, and Akemi Kunibe, for her heartfelt advice and introducing me to the wonders of the backcountry. I also like to thank Jordan Berg, Mark Grabiner, Victor Pinho, and Amanda Van Hoesen for being my sounding board outside of the laboratory.

Exploring the wild outdoors has been a saving grace for dealing with the difficult moments of graduate school. I want to thank those of you who have shared it with me, in particular, Michael Novak, Anna Fryjoff-Hung, Lawrence Sim, Sarah Hillenbrand, Nathan Gadye, Arik Gadye, Eric Davila, Amber Davila, Shae Selix, Caleb Miller-Miro, Chelsea Miller-Miro, Zachary Reiss-Davis, Kristen Ray, Alanna Kwoka, and Vihang Mehta. Our expeditions together require a great deal of trust and cohesion, and I want to thank you for extending that to me.

I would like to thank my family for their support throughout my career. My parents, Clement and Corinne, deserve credit for encouraging me in scientific inquiry from a young age. I would also like to thank my mother-in-law, Sarah, and my aunt, Judy, for lending me their kind ears through thick and thin.

A great deal of this dissertation would not be possible without one Zachary Newman. I have had the pleasure of working alongside Zach since I was an undergraduate student at Berkeley. He has been a great scientific mentor and friend, and I have been lucky to have his unwavering support through all kinds of ups and downs. Thank you for believing in me and my potential.

Finally, I can never repay my husband, Levi Gadye, for the sacrifices he made to help me in my pursuit of science. Levi is my best friend, partner in crime, partner in belaying, hiking buddy, snowboarding buddy, armchair scientific advisor, and much, much more. Thank you for supporting me through tears when I thought all was lost, through 10 hour bleary-eyed drives on highway 395, through -30°C winds in the pursuit of turns on the slopes, through altitude sickness and broken bones, through endless miles of scree fields and impenetrable manzanita, through thousands of mosquito bites, and through the many all-nighters I pulled while writing this text.

I am still far from unflappable, but I have come out the other side of this undertaking with more equanimity and fortitude than I thought possible.

Chapter 1:
Functional and genetic characterization of homeostatic plasticity

Introduction

Homeostasis is a critical feature of life, and neuronal activity is no exception. Mounting evidence in the field has shown that homeostatic signaling mechanisms work to maintain the fidelity and efficacy of synaptic transmission in response to environmental challenges. These signaling mechanisms, broadly classified as homeostatic synaptic plasticity, alter presynaptic and postsynaptic function to stabilize baseline activity. A major goal of the field is to identify the molecular components of these signaling mechanisms, and shed light on the physiological limits of synaptic transmission.

1.1 Classical models of synaptic plasticity and synaptic homeostasis

The ability of a synapse to modulate the strength of its connections, known as synaptic plasticity, has long been thought as an important mechanism for learning and memory (Hebb, 1949). The description of long-term potentiation (LTP) by Bliss and Lomo was a key piece of evidence in this regard, in no small part due to the fact that this robust, activity-dependent increase in synaptic strength was observed in the hippocampus, itself a region of the brain identified clinically as a key region in memory formation (Bliss and Lomo, 1973; Scoville and Milner, 1957)(Figure 1.1A). Long-term depression (LTD) was discovered later as an opposing process, by which disuse selectively weakens synapses (Lynch et al., 1977)(Figure 1.1A). However, this leads to a troubling set of observations. In the paradigm of LTP, neurons that fire action potentials (APs) would more effectively depolarize their postsynaptic partners, leading to an unchecked positive feedback loop. Similarly, unchecked LTD could lead to loss of information flow entirely. Neural circuits therefore need a regulatory mechanism to constrain these destabilizing forces and maintain neural activity within physiologically tolerable levels (Abbott and Nelson, 2000; Miller and MacKay, 1994). Homeostatic plasticity serves to stabilize these forces.

There are two essential features of homeostatic systems: 1) a set-point from which deviation can be measured by the system and 2) an effector with the capacity to alter the observed parameter. In the context of neuronal function, one can imagine a panoply of set-points and effector mechanisms, operating at the scale of individual synapses or across entire networks of neurons. One such model, called the sliding threshold model, posits that the threshold for invoking LTP or LTD is adjusted by prior neuronal activity (Bear et al., 1987; Bienenstock et al., 1982). Specifically, this model predicts that prolonged periods of intense neural activity raise the threshold for LTP induction, while periods of weak activity lowers this threshold (Figure 1.1B). Experiments on the developing visual cortex and barrel cortex have shown that sensory deprivation lowers the threshold for LTP at these synapses, lending support for this model (Guo et al., 2012; Hardingham et al., 2008; Kirkwood et al., 1996). The converse is also true, as increasing sensory input to the visual cortex has been shown to favor the induction of LTD (Quinlan et al., 1999).

While the sliding threshold model addresses the stabilization of synaptic strength, it does not address the stabilization of firing rate or network activity. Total ablation of firing with tetrodotoxin (TTX) boosts the postsynaptic response, while increasing firing by pharmacological

blockade of inhibition curbs the postsynaptic response (O'Brien et al., 1998; Turrigiano et al., 1998). Postsynaptic sites can compensate for aberrant presynaptic transmission by increasing or decreasing gain to maintain an average firing rate, a phenomenon known as synaptic scaling (Figure 1.1C). Synaptic scaling differs from the sliding threshold model in that it appears to work globally across all synapses of a given neuron. TTX blockade experiments in cultured neurons demonstrate that most synapses will experience an increase in gain, regardless of how those inputs might have been used prior to TTX application. The sliding threshold model stands in contrast to this, working in a synapse-specific manner. Even if synaptic gain is increased or decreased globally, individual synapses that receive subthreshold input will undergo LTD and those that surpass the threshold will undergo LTP.

What the sliding threshold model and synaptic scaling have in common is that they both act primarily at the postsynaptic end in response to changes in presynaptic activity. Perturbing the receipt of neurotransmission at the postsynaptic end induces a different form of homeostatic compensation that acts at the presynaptic end. These mechanisms, collectively known as presynaptic homeostatic plasticity, alter the efficiency of presynaptic neurotransmitter release. One form of such plasticity, known as presynaptic homeostatic potentiation (PHP), was first observed clinically in the neuromuscular junction (NMJ) of myasthenia gravis patients (Cull-Candy et al., 1980). This study found that muscle weakness associated with myasthenia gravis is due to reduced postsynaptic response to individual vesicles of the neurotransmitter acetylcholine (Cull-Candy et al., 1980). Surprisingly, Cull-Candy et al. observed a compensatory increase in acetylcholine release from the motor neuron that restored overall postsynaptic currents to normal levels (Figure 1.2B). This same surge in AP-evoked neurotransmitter release has been observed in the NMJs of rat, mouse, and *Drosophila* models, and mammalian central nervous system (CNS) synapses (Petersen et al., 1997; Plomp et al., 1992; Wang et al., 2010).

Presynaptic homeostatic plasticity also encompasses mechanisms that prevent runaway excitation. Presynaptic silencing was first described in dissociated hippocampal neurons cultured in elevated K+ concentrations (Moulder et al., 2004, 2006). Presynaptic silencing features a decrease in the number of synaptic vesicles primed for release and reduced probability of synaptic vesicle release (Moulder et al., 2004) (Figure 1.2C). Overexpression of the vesicular glutamate transporter (VGlut) in *Drosophila* motor neurons increases the amount of neurotransmitter packaged into each vesicle, eliciting an exaggerated response to an individual vesicle at the postsynapse without changing overall excitatory input (Daniels et al., 2004). Similar to presynaptic silencing, this presynaptic homeostatic depression (PHD) model features a decrease in the number of synaptic vesicles released per AP (Daniels et al., 2004; Li et al., 2018) (Figure 1.2D). Unlike PHP mechanisms that potentiate neurotransmission, neither presynaptic silencing nor PHD appear to be dependent on postsynaptic receptor activation (Li et al., 2018; Moulder et al., 2006).

Since presynaptic silencing and PHD does not require postsynaptic dysfunction, they are likely cell-autonomous mechanisms. Thus, presynaptic silencing and PHD cannot simply be the reversal of processes invoked in presynaptic homeostatic potentiation regimes. This asymmetry poses an interesting challenge for the field. What molecular components enact PHP and PHD?

Do these pathways have unique set points and effector pathways? How can a neuron orchestrate the balance of these plasticity programs? How do interacting neurons influence this balance?

1.2 The *Drosophila* neuromuscular junction as a model system for presynaptic homeostatic plasticity

PHP has been studied extensively in the NMJ of the 3rd instar *Drosophila melanogaster* larva (Davis et al., 1998; DiAntonio et al., 1999; Frank et al., 2006; Newman et al., 2017; Petersen et al., 1997), however there has been little consideration of the role of the connected CNS circuits in these processes. The *Drosophila* central nervous system (CNS) is an attractive model due to the multitude of electrophysiological, genetic, molecular, and anatomical tools with which to probe the system. Approximately 77% of human disease-causing genes have *Drosophila* cognates (Reiter et al., 2001; Rubin et al., 2000), and many neurodevelopmental disorders and neurodegenerative diseases have established models in fly (Chan and Bonini, 2000; Ugur et al., 2016).

Since the introduction of the fillet preparation (Jan and Jan, 1976a), which provides access to both the motor neuron axons and the body wall muscles (Figure 1.3 A), a wellspring of discoveries have been made in neuronal development, axonal transport and pathfinding, synaptic plasticity, short and long-term homeostasis and muscle development (Budnik and Ruiz-Canada, 2006; Collins and DiAntonio, 2007; Frank et al., 2013; Keshishian et al., 1996).

Control over the *Drosophila* NMJ system has been expanded by a wealth of genetic tools including large collections of mutants, P-element transformation tools (Rubin and Spradling, 1982; Spradling and Rubin, 1982), phiC31 integrases (Bateman et al., 2006; Bischof et al., 2007; Groth et al., 2004; Markstein et al., 2008), CRISPR-Cas9 (Bassett and Liu, 2014; Bassett et al., 2015; Gratz et al., 2015), and RNA interference (RNAi) lines (Dietzl et al., 2007; Ni et al., 2008, 2009; Perkins et al., 2015). Even greater cell-specificity and temporal-specificity has been granted by the advent of the Gal4-UAS system (Brand and Perrimon, 1993), GeneSwitch Gal4 (Nicholson et al., 2008), Gal80ts (McGuire et al., 2003), the lexA-lexAop system (Lai and Lee, 2006), and the split-Gal4 system (Pfeiffer et al., 2010). Further advances in optical detection of neuronal activity, using postsynaptically localized genetically encoded Ca2+ sensors (GCaMPs), improve the spatial resolution of detecting synaptic transmission over traditional electrophysiological methods (Newman et al., 2017; Peled and Isacoff, 2011; Peled et al., 2014). All of these tools, combined with ease of culture and short generation times, have made the fruit fly NMJ an excellent model for interrogating synaptic function.

1.2.1 The organization of the *Drosophila* NMJ

During early CNS development, neuroblasts delaminate from the neuroectoderm and undergo a series of division that give rise to motor neurons (MNs), in addition to an assortment of interneurons and glia (Broadus et al., 1995; Doe, 1992; Hartenstein and Campos-Ortega, 1984; Landgraf et al., 1997). During embryonic neurogenesis, newly born MNs extend their axons towards the body wall muscles to find their postsynaptic partners (Figure 1.3 B). These MN axons are bundled into three tracts as they exit the ventral nerve cord (VNC), where the MN cell

bodies reside (Hoang and Chiba, 2001). These anatomical patterns are highly stereotyped. Neuroblasts and their progeny lie in well-characterized patterns within each hemisegment of the embryonic VNC, and clonal analysis and dye-injection techniques have allowed researchers to identify the axonal targets of the vast majority of MNs (Doe, 1992; Hoang and Chiba, 2001; Landgraf et al., 1997; Schmid et al., 1999) (Figure 1.3 B). These MNs innervate approximately 30 muscle fibers per hemisegment in a repeating pattern (Crossley, 1978), allowing similar synapses to be observed in a single specimen (Figure 1.3 B). The muscle fibers targeted by these MNs are large and easy to identify, making this an attractive system for electrophysiological analysis.

Pioneering studies of the *Drosophila* NMJ found that the most abundant class of MN, the type I MN, supplied the main excitatory inputs to the muscle using the neurotransmitter glutamate (Jan and Jan, 1976a, 1976b; Johansen et al., 1989). The remaining neurons belong to the type II and type III classes, which primarily release monoamines and peptides respectively (Cantera and Nässel, 1992; Gorczyca et al., 1993; Monastirioti et al., 1995).

Type I MNs have been subject to the greatest experimental interrogation, as they share many molecular and structural similarities to mammalian CNS synapses (Budnik and Ruiz-Canada, 2006). Two classes of boutons are observed within the type I MN class, named type Ib (big) and Is (small) (Figure 1.3 C). Type Ib boutons are identified by their larger, more elaborate subsynaptic reticulum (SSR) compared to type Is boutons, both of which can be visualized with immunofluorescence staining against postsynaptic scaffolding proteins such as Discs large (Dlg) (Broadie and Bate, 1993; Chen and Featherstone, 2005; Zito et al., 1999) (Figure 1.3 D). In addition to differences in morphology, type Ib and Is MNs show differences in innervation patterns and physiological function. Each type Ib MN typically innervates one muscle, while type Is MNs innervate multiple muscles (Hoang and Chiba, 2001; Kim et al., 2009). Electrophysiological probing of these MNs reveal that type Ib MNs provide tonic excitatory drive to their targets, while type Is MNs have phasic firing patterns (Atwood and Klose, 2009; Atwood et al., 1997; Choi et al., 2004; Lnenicka and Keshishian, 2000; Schaefer et al., 2010).

1.2.2 Synaptic plasticity and homeostasis at the *Drosophila* NMJ

The diversity of physiological phenotypes and the experimental accessibility of the *Drosophila* NMJ has led to an explosion of research into the molecular and cellular mechanisms of synaptic plasticity, including homeostatic plasticity. Acute forms of plasticity, including depression and facilitation, have been observed in the *Drosophila* NMJ. These forms of plasticity act presynaptically and are dependent on AP frequency (Fioravante and Regehr, 2011; Zucker and Regehr, 2002).

Synaptic vesicle exocytosis from the presynapse is a probabilistic phenenomenon, and the response at the postsynapse can be described formally by the equation: $n * P_r * q$ (Schneggenburger et al., 2002). Here n represents the number of sites from which a vesicle can be released, known as active zones (AZs), P_r represents the probability with which a vesicle can be released, and q represents the quantal size, a reflection of the total amount of neurotransmitter in a single vesicle. Presynaptic modes of plasticity largely alter these parameters. In these

classical models of plasticity, high frequency stimulation is thought to cause high P_r synapses to depress, that is their P_r diminishes over the course of the stimulation regime. Facilitation, on the other hand, describes an observed increase in P_r after stimulation of low P_r synapses. These two forms of plasticity have been observed in convergent Ib and Is MNs in *Drosophila*, where Ib inputs facilitate under the same conditions that Is inputs depress (Kurdyak et al., 1994; Lnenicka and Keshishian, 2000; Lu et al., 2016).

PHP similarly appears to be input-specific. Early descriptions of PHP in the *Drosophila* NMJ have shown that engagement of this process occurs normally in development as the motor neuron and muscle fiber grow, but also in response to acute blockade or genetic manipulation of the postsynaptic glutamate receptors (Davis, 2006, 2013; Davis and Goodman, 1998; Davis and Müller, 2015; Frank, 2014). Results of these experiments suggest that reduced postsynaptic depolarization is communicated in a retrograde fashion to the MN to increase presynaptic release, therefore maintaining appropriate synaptic drive (Paradis et al., 2001). One such genetic model for PHP, in which one class of postsynaptic ionotropic glutamate receptor (*GluRIIA*) bears a loss-of-function mutation ($GluRIIA^{SP16}$), has been shown to reduce quantal size, as measured by the miniature excitatory postsynaptic potentials (mEPSP) of the muscle (Petersen et al., 1997). However, the overall excitatory postsynaptic potential (EPSP) remains similar to wild-type controls, making EPSP amplitude the presumed set-point of the system (Petersen et al., 1997). This indicates that the process of PHP must be modulating either n or P_r to compensate for the reduced size of q, according to the equation put forth by Schneddeger et al. However, such electrophysiological methods of measuring synaptic function are largely blind to which inputs are altered by PHP. Optical recording of synaptic activity using postsynaptically localized GCaMPs have allowed researchers to assign postsynaptic response to individual AZs within a bouton (Peled and Isacoff, 2011; Peled et al., 2014). Such experiments have now demonstrated that this form of PHP occurs at Ib inputs and not at Is inputs, despite their proximity and convergence onto the same muscle fiber (Newman et al., 2017).

What is the nature of this retrograde signal that appears to act specifically at Ib terminals? A few molecular components of this signaling pathway have been identified, although largely at the postsynaptic end of the NMJ. Postsynaptic Ca2+/calmodulin-dependent protein kinase II (CaMKII) inhibition is required for an increase in presynaptic T-bars at the AZ, a phenomenon also observed in the *GluRIIA* null model of PHP (Haghighi et al., 2003). Furthermore, inhibition of postsynaptic CaMKII has been shown to recapitulate PHP-induced increases in P_r in Ib terminals specifically (Newman et al., 2017). Additionally, postsynaptic activation of target of rapamycin (TOR) or its downstream effector S6 ribosomal protein kinase (S6K) mediates the expression of *GluRIIA*-dependent homeostasis (Penney et al., 2012). Known retrograde signaling mechanisms, including the BMP pathway (Goold and Davis, 2007; Haghighi et al., 2003) and the Sema-2b/PlexB pathway (Orr et al., 2017), have been shown to be required for this process. However, it is unclear if these signaling pathways are instructive or permissive signals of PHP (Marqués and Zhang, 2006).

Bidirectionality is a key feature of homeostatic systems, and thus PHD can be used to interrogate the limits of homeostatic plasticity. Presynaptic homeostatic depression can be induced by overexpression of VGlut, which results in an increase in mEPSP amplitude and a concomitant

reduction in quantal content ($q * n$) to restore EPSP amplitudes (Gaviño et al., 2015; Li et al., 2018). However, since the expression of PHD does not appear to require *GluRIIA* receptor activation, distinct molecular mechanisms must be mediating the expression of PHD and PHP.

How a neuron can balance acute forms of plasticity with homeostatic processes remains an open question. Activation of postsynaptic ionotropic glutamate receptors (iGluRs) has been shown to be crucial for the recovery from presynaptic depression (Kauwe and Isacoff, 2013). This process occurs rapidly, as activation of a light-gated iGluR (LiGluR) improves recovery within minutes of optical stimulation (Kauwe and Isacoff, 2013). This process is dependent on postsynaptic inhibition of CaMKII and presynaptic activation of cyclic AMP (cAMP) (Kauwe and Isacoff, 2013), the latter which enhances recruitment of vesicles from reserve pools in the axon terminal to the readily-releasable pool (RRP) (Kuromi and Kidokoro, 2000). However, the necessary and sufficient molecular determinants of PHP remain elusive.

1.3 A functional genomics view into synaptic plasticity and homeostasis

Current electrophysiological and optical tools allow for synaptic function to be described in exquisite detail. However, such methods are low-throughput. The identification of molecular signaling mechanisms in this way requires testing candidate genes one by one. Functional genomics methods, which include methods as diverse as fluorescence *in situ* hybridization (FISH) and RNA-sequencing (RNA-seq), have the capacity to test thousands of hypotheses at once (Geschwind and Konopka, 2009). While spatial and temporal resolution is limited, such information can be used to generate specific and detailed hypotheses for the workings of plastic and metaplastic mechanisms, providing a formidable complement to functional studies. The discovery-oriented methods of functional genomics have been embraced by disease-focused fields of research, as such information can be used to uncover potential etiological mechanisms or new therapeutic targets (Nagasaka et al., 2005; Nishimura et al., 2007; Tang et al., 2001; Thomas et al., 2008).

The aim of functional genomics is to understand the relationship between phenotype and genotype by understanding how such genes are translated, transcribed, or epigenetically-regulated. Improvements in sequencing technologies and decreases in cost of preparing samples over the past few decades has led to research on the molecular basis of neuronal diversity (Cahoy et al., 2008; Lobo et al., 2006; Sugino et al., 2006) and synaptogenesis (Emes et al., 2008). Data from experiments are valuable not only in their original publication, but also in their availability to the public in databases like the Gene Expression Omnibus. Access to these data sets allows other researchers to analyze and combine pre-existing data sets to formulate new hypotheses. The most comprehensive and thorough resource of gene expression patterns at single-cell resolution in both mouse and human brain is the Allen Brain Atlas (Hawrylycz et al., 2012; Hodge et al., 2019; Lein et al., 2007; Tasic et al., 2016, 2018), and has already spawned new analyses of the data (Bakken et al., 2018; Coe et al., 2019; Kalmbach et al., 2018).

Within the past decade, improvements in sensitivity of RNA-seq experiments have allowed researchers to prepare libraries from smaller and smaller samples (Combs and Eisen, 2013, 2015;

Lott et al., 2011), including sequencing libraries from individual cells (Hashimshony et al., 2012; Islam et al., 2011; Ramsköld et al., 2012; Sasagawa et al., 2013; Tang et al., 2009). This is a major technological breakthrough, as experimenters can now overcome the limitations of studying gene expression changes in an ensemble of cells. In this section, we explore the canon of functional genomics experiments in the field of neurobiology and the emerging body of work utilizing single-cell RNA-sequencing (scRNA-seq) to investigate neuronal diversity.

1.3.1 Linking neuronal activity and plasticity to gene expression

The role of calcium in AP-evoked synaptic vesicle exocytosis and many forms of both pre- and postsynaptic plasticity has been long appreciated by neurobiologists (Regehr, 2012; Südhof, 2013; Zucker, 1999). However, interest in the role of calcium in the regulation of gene expression began in studies of the response of quiescent fibroblasts to stimulation by growth factors. Exposing 3T3 fibroblasts to platelet-derived growth factor leads to a spike in the expression of a proto-oncogene, *c-fos*, within minutes of stimulation (Greenberg and Ziff, 1984). Subsequent experiments in rat pheochromocytoma-derived PC12 cells have shown that the activation of nicotinic acetylcholine receptors also results in a transient, calcium-dependent rise in *c-fos* transcription (Greenberg et al., 1986). Greenberg et al. also observed that this effect could be recapitulated by depolarization, which allows calcium entry through L-type voltage-gated calcium channels. Increased *c-fos* transcription has been observed in the CNS of mice and rats after seizure activity (Morgan et al., 1987; Saffen et al., 1988), spinal cord neurons after tactile stimulation (Hunt et al., 1987), and in the suprachiasmatic nucleus after optical stimulation (Rusak et al., 1990). This raised the possibility that calcium-dependent changes in gene expression may have specialized roles in neuronal function. Altered synaptic plasticity and learning deficits in a *c-fos* mutant mouse model provides further support for this idea (Fleischmann et al., 2003).

Investigations of the role of cyclic AMP (cAMP) on gene expression provide a separate line of evidence that neuronal activity could influence gene expression. Montminy et al. identified a cAMP-responsive element (CRE) that regulated the mRNA levels of somatostatin in 3T3 and PC12 cells (Montminy et al., 1986a, 1986b). Elevation of cAMP leads to the phosphorylation of a CRE binding protein (CREB), which leads to the activation of transcription (Gonzalez and Montminy, 1989). CREB serves as a point of convergence for both cAMP-dependent and calcium-dependent changes in gene expression, as Greenberg and colleagues later found that increased *c-fos* expression was mediated the binding of a calcium-responsive element to CREB (Sheng et al., 1991).

Hundreds of genes involved in plasticity have since been identified in the neurons of a variety of model organisms after induction of LTP (Nedivi et al., 1993), activation of NMDA receptors (Cole et al., 1989; Hong et al., 2004), electroconvulsive seizure protocols (Altar et al., 2004; Guan et al., 2005), genetic manipulations modeling neurological disease (Bateup et al., 2013; Sando et al., 2012), and optogenetic stimulation (Chen et al., 2016). Genes identified in these studies include *Arc*, a protein involved in AMPA receptor trafficking and synaptic scaling (Chowdhury et al., 2006; Lyford et al., 1995; Rial Verde et al., 2006; Shepherd et al., 2006), *cpg15*, a GPI-anchored membrane protein that enhances dendritic outgrowth and synapse

maturation (Cantallops et al., 2000; Nedivi et al., 1998), and *homer1*, a synaptic scaffolding protein whose mRNA is subject to activity-dependent processing (Bottai et al., 2002). Even known activity-regulated genes, such as BDNF, were found to be CREB dependent (Shieh et al., 1998; Tao et al., 1998).

Calcium-dependent gene regulation has sparked interest in the idea of synapse-to-nucleus communication (Ch'ng and Martin, 2011; Deisseroth et al., 2003). Some evidence suggests that the mode of calcium entry can influence which genetic programs are activated in a neuron (Bading et al., 1993; Lerea and McNamara, 1993). While elucidating the differences between these pathways could be an essential link in understanding the relationship between gene expression and neuronal activity, it remains poorly understood. Indeed, signaling cascades of this ilk may be the key to understanding how neurons coordinate the various programs of homeostatic plasticity. The upshot of all of this is that the hypothesis-generating approach of functional genomics will continue to be useful, and will hopefully clarify the muddier aspects of mechanistic understanding.

1.3.2 Single-cell RNA-sequencing and deconvolution of neuronal cell types

Observing changes in gene expression and translation of gene products has provided insight into the molecular mechanisms and potential therapeutic targets of neurodevelopmental disorders such as Fragile X syndrome (Ceolin et al., 2017; Kong et al., 2014; Shu et al., 2019), Rett syndrome (Gogliotti et al., 2018; Sanfeliu et al., 2019), Angelman syndrome (Gabel et al., 2015; Lopez et al., 2017), and autism spectrum disorders (Bateup et al., 2013; Lanz et al., 2013; Mattei et al., 2017; Oskvig et al., 2012). However, it is often useful to understand how genetic perturbations or pharmacological manipulations affect specific types of neurons. The burgeoning field of single-cell transcriptomics is beginning to bridge this gap.

Researchers in stem cell biology, cancer biology, and immunology have led the charge with the application of this technology (Grün et al., 2015; Islam et al., 2011; Klein et al., 2015; Navin et al., 2011; Patel et al., 2014; Ramsköld et al., 2012; Shalek et al., 2013, 2014; Treutlein et al., 2014). Neurobiologists have quickly joined the ranks, and have used scRNA-seq to identify sub-classes of retinal ganglion cells and amacrine cells in the retina (Macosko et al., 2015), new types of GABAergic cells in mouse visual cortex (Tasic et al., 2016), new markers of cell type for neurons and glia of the primary somatosensory cortex and the CA1 region of the hippocampus (Zeisel et al., 2015), and new genes involved in dendritic targeting in *Drosophila* olfactory projection neurons (Li et al., 2017). However, the deconvolution of cell types using RNA-sequencing data poses an interesting challenge. Separation of cells into distinct populations often relies on dimensionality-reduction methods and unsupervised clustering using a subset of genes with the greatest variance across the entire data set. Do these genes reflect genuine differences in cell type? If so, how can investigators identify relevant gene expression changes according to developmental state, activity, or environmental variables?

The combination of lineage tracing and scRNA-seq has helped greatly in identifying gene programs involved in stem cell differentiation and tissue homeostasis (Fletcher et al., 2017; Gadye et al., 2017; Llorens-Bobadilla et al., 2015; Trapnell et al., 2014; Zhong et al., 2018).

However, the key to understanding how homeostatic and metaplastic programs operate in specific types of neurons will require the integration of gene expression data with functional and anatomical data. Indeed, new work seeks to identify genes in the context of neuronal activity (Lacar et al., 2016; Tyssowski et al., 2018; Wu et al., 2017), cell morphology (Cadwell et al., 2016), electrophysiological properties (Cadwell et al., 2016; Fuzik et al., 2016), and disease states (Hook et al., 2018; Mathys et al., 2019; Velmeshev et al., 2019).

Such experiments have already begun to upend dogma in the field of neurobiology. Neurons have been classically categorized by their expression of fast-acting neurotransmitters, which was previously assumed to be mutually exclusive (Dale, 1935). scRNA-seq experiments have provided evidence of co-expression of multiple fast-acting neurotransmitters (Allen et al., 2019; Granger et al., 2018; Poulin et al., 2020; Zeisel et al., 2015) and neuropeptides (Chen et al., 2017; Croset et al., 2018; Smith et al., 2019). Single-cell transcriptomics has opened new and exciting avenues for the study of synaptic plasticity, and the project of disentangling neuronal types and their capacity to adapt has only just begun.

Summary of dissertation

In the following chapters, I present RNA-sequencing data of purified populations of *Drosophila* larval motor neurons to generate new hypotheses about the genetic mechanisms of presynaptic homeostatic plasticity. In **Chapter 2**, I utilize RNAi constructs against critical presynaptic active zone components, which phenocopy presynaptic silencing models, to investigate how motor neurons compensate for this genetic insult. I have found that knockdown of these genes results in gene expression changes that increase excitability. In **Chapter 3**, I utilize a transgenic fly line bearing an insertion in *Msp300*, which phenocopies the classic *GluRIIA*$^{-/-}$ model of presynaptic homeostatic plasticity. I show that these motor neurons enact similar anterograde genetic programs as the presynaptic silencing model, but also downregulate ECM-interacting proteins and other enzymes known to post-translationally modify AZ components. I propose a new model of presynaptic homeostatic plasticity that integrates my findings with that of previous functional and structural studies. In **Chapter 4**, I present a single-cell RNA-seq survey of type I motor neurons. I show that the neurons cluster into spatiotemporal groups which are correlated with markers of activity.

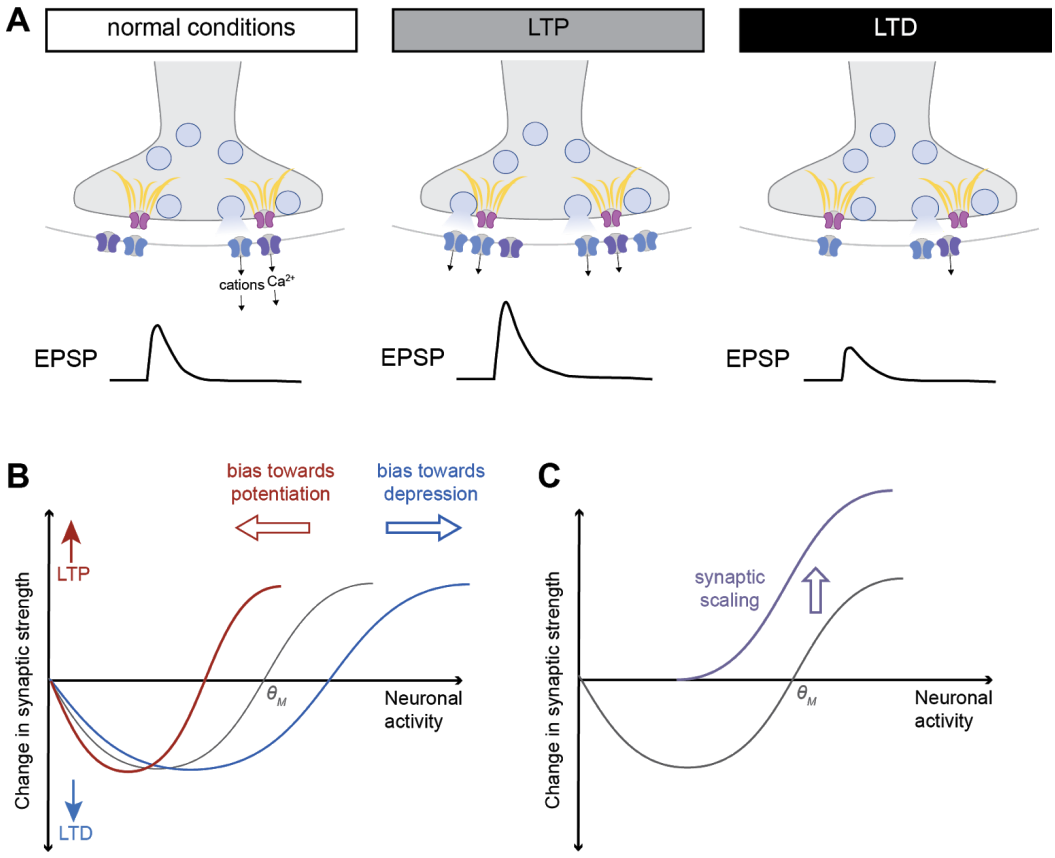

Figure 1.1) Models of synaptic plasticity and their regulation by homeostatic plasticity and metaplasticity. **A**) Synaptic responses under normal conditions, during long-term potentiation (LTP), and long-term depression (LTD). Under normal conditions AP-firing leads to depolarization of the presynaptic terminal through voltage-gated calcium channels (magenta), leading vesicles of neurotransmitter (light blue circles) docked at presynaptic release sites (yellow scaffold) to be released. Neurotransmitter binding to postsynaptic ionotropic receptors (blue and purple) lead to Ca^{2+} and other cations into the postsynaptic neuron. LTP results in enhanced excitatory postsynaptic potentials (EPSP) as a result of increased trafficking of ionotropic neurotransmitter receptors to the postsynaptic membrane. LTD results in decreased EPSP amplitudes. **B**) Sliding threshold model. Neuronal activity resulting in weak Ca^{2+} influx and recruitment of the postsynaptic neuron (red curve) slides the threshold (θ_M) for LTP towards lower neuronal activities, while too much activity (blue curve) increases θ_M. **C**) Synaptic scaling model. Chronic inactivity increases the postsynaptic response after the relief of AP blockade (purple curve).

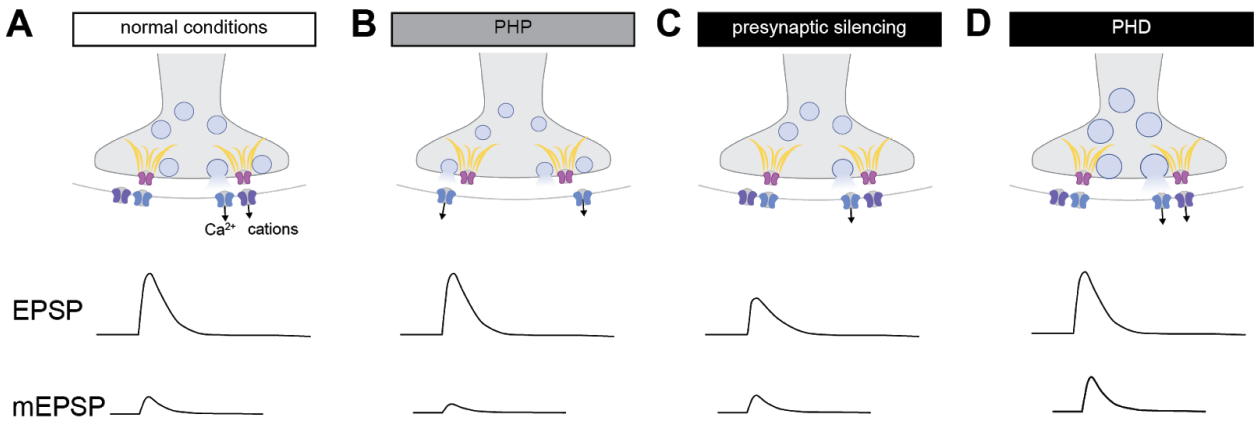

Figure 1.2) Models of presynaptic homeostatic plasticity. **A**) Normal presynaptic release and postsynaptic response. **B**) Model of presynaptic homeostatic potentiation (PHP). Loss of postsynaptic ionotropic neurotransmitter receptors results in decreased postsynaptic response to a single vesicle of neurotransmitter (miniature EPSP) but no overall change in the total EPSP. EPSP amplitude is stabilized by an increase in the probability of vesicular release per AP. **C**) Model of synaptic silencing. Increased firing leads to fewer docked vesicles and a smaller EPSP with no change in the mEPSP. **D**) Model of presynaptic homeostatic depression (PHD). Overexpression of neurotransmitter transporters results in larger vesicles and an increase in the mEPSP, but no change in the overall EPSP. EPSP amplitude is stabilized by a decrease in the probability of vesicular release per AP.

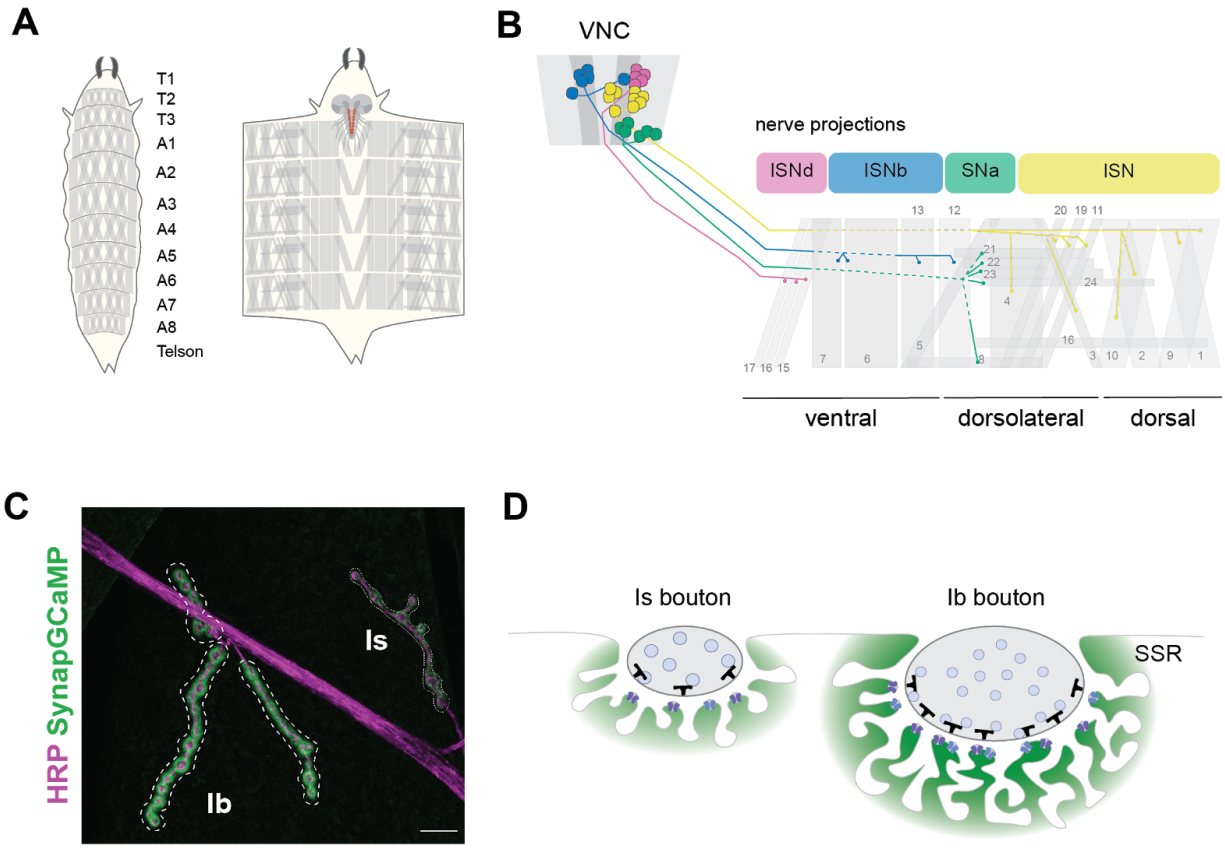

Figure 1.3) Organization of the *Drosophila* NMJ. **A)** Body plan of the third instar larva. *Left*, segments of the intact 3rd instar larva. Segments T1-T3 correspond to the thorax, while segments A1-A9 (telson) correspond to the abdomen. *Right*, diagram of the fillet preparation. **B)** Arrangement of MN cell bodies in the VNC and their projections to the body wall muscles. The intersegmental nerve (ISN, yellow) contains projections to the dorsal muscle segments (1, 2, 3, 4, 9, 10, 11, 19, 20). The segmental nerve A (SNa, green) contains projections to the lateral external muscles (8, 21, 22, 23, 24). The ISNb (blue) and ISNd (pink) branches project to the ventral muscles (ISNb: 6, 7, 12, 13; ISNd: 15, 16, 17). The transverse nerve and SNc nerve are not shown. **C)** Confocal fluorescence microscopy image of the muscle 4 Ib and Is boutons. The SynapGCaMP signal, localized to the SSR, has been amplified with an anti-GFP antibody (green). Axons are visualized with anti-Hrp-Cy3 (magenta). Scale bar, 10 µm. Ib boutons are outlined with the large dotted lines, and Is boutons are outlined with the small dotted line. **D)** Side-on view of type I boutons. Is boutons have larger vesicles (blue circles) and fewer AZs (black Ts), while Ib boutons have smaller vesicles and more AZs. The muscle SSR (green) is more elaborated at the Ib NMJ relative to the Is, and has a greater density of postsynaptic iGluRs (purple, gray, and blue). Fly iGluRs are composed of either GluRIIA or GluRIIB subunits, in addition to the required GluRIIC, GluRIID, or GluRIIE subunits.

References

Abbott, L.F., and Nelson, S.B. (2000). Synaptic plasticity: taming the beast. Nat. Neurosci. *3 Suppl*, 1178–1183.

Allen, A.M., Neville, M.C., Birtles, S., Croset, V., Treiber, C.D., Waddell, S., and Goodwin, S.F. (2019). A single-cell transcriptomic atlas of the adult Drosophila ventral nerve cord.

Altar, C.A., Laeng, P., Jurata, L.W., Brockman, J.A., Lemire, A., Bullard, J., Bukhman, Y.V., Young, T.A., Charles, V., and Palfreyman, M.G. (2004). Electroconvulsive seizures regulate gene expression of distinct neurotrophic signaling pathways. J. Neurosci. *24*, 2667–2677.

Atwood, H.L., and Klose, M.K. (2009). Comparative biology of invertebrate neuromuscular junctions.

Atwood, H.L., Karunanithi, S., Georgiou, J., and Charlton, M.P. (1997). Strength of synaptic transmission at neuromuscular junctions of crustaceans and insects in relation to calcium entry. Invert. Neurosci. *3*, 81–87.

Bading, H., Ginty, D.D., and Greenberg, M.E. (1993). Regulation of gene expression in hippocampal neurons by distinct calcium signaling pathways. Science *260*, 181–186.

Bakken, T.E., Hodge, R.D., Miller, J.A., Yao, Z., Nguyen, T.N., Aevermann, B., Barkan, E., Bertagnolli, D., Casper, T., Dee, N., et al. (2018). Single-nucleus and single-cell transcriptomes compared in matched cortical cell types. PLoS One *13*, e0209648.

Bassett, A.R., and Liu, J.-L. (2014). CRISPR/Cas9 and genome editing in Drosophila. J. Genet. Genomics *41*, 7–19.

Bassett, A.R., Kong, L., and Liu, J.-L. (2015). A genome-wide CRISPR library for high-throughput genetic screening in Drosophila cells. J. Genet. Genomics *42*, 301–309.

Bateman, J.R., Lee, A.M., and Wu, C.-T. (2006). Site-specific transformation of Drosophila via phiC31 integrase-mediated cassette exchange. Genetics *173*, 769–777.

Bateup, H.S., Johnson, C.A., Denefrio, C.L., Saulnier, J.L., Kornacker, K., and Sabatini, B.L. (2013). Excitatory/inhibitory synaptic imbalance leads to hippocampal hyperexcitability in mouse models of tuberous sclerosis. Neuron *78*, 510–522.

Bear, M.F., Cooper, L.N., and Ebner, F.F. (1987). A physiological basis for a theory of synapse modification. Science *237*, 42–48.

Bienenstock, E.L., Cooper, L.N., and Munro, P.W. (1982). Theory for the development of neuron selectivity: orientation specificity and binocular interaction in visual cortex. J. Neurosci. *2*, 32–48.

Bischof, J., Maeda, R.K., Hediger, M., Karch, F., and Basler, K. (2007). An optimized transgenesis system for Drosophila using germ-line-specific phiC31 integrases. Proc. Natl. Acad. Sci. U. S. A. *104*, 3312–3317.

Bliss, T.V., and Lomo, T. (1973). Long-lasting potentiation of synaptic transmission in the dentate area of the anaesthetized rabbit following stimulation of the perforant path. J. Physiol. *232*, 331–356.

Bottai, D., Guzowski, J.F., Schwarz, M.K., Kang, S.H., Xiao, B., Lanahan, A., Worley, P.F., and Seeburg, P.H. (2002). Synaptic activity-induced conversion of intronic to exonic sequence in Homer 1 immediate early gene expression. J. Neurosci. *22*, 167–175.

Brand, A.H., and Perrimon, N. (1993). Targeted gene expression as a means of altering cell fates and generating dominant phenotypes. Development *118*, 401–415.

Broadie, K., and Bate, M. (1993). Innervation directs receptor synthesis and localization in Drosophila embryo synaptogenesis. Nature *361*, 350–353.

Broadus, J., Skeath, J.B., Spana, E.P., Bossing, T., Technau, G., and Doe, C.Q. (1995). New neuroblast markers and the origin of the aCC/pCC neurons in the Drosophila central nervous system. Mech. Dev. *53*, 393–402.

Budnik, V., and Ruiz-Canada, C. (2006). The Fly Neuromuscular Junction: Structure and Function, Volume 75 - 1st Edition (Elsevier Academic Press).

Cadwell, C.R., Palasantza, A., Jiang, X., Berens, P., Deng, Q., Yilmaz, M., Reimer, J., Shen, S., Bethge, M., Tolias, K.F., et al. (2016). Electrophysiological, transcriptomic and morphologic profiling of single neurons using Patch-seq. Nat. Biotechnol. *34*, 199–203.

Cahoy, J.D., Emery, B., Kaushal, A., Foo, L.C., Zamanian, J.L., Christopherson, K.S., Xing, Y., Lubischer, J.L., Krieg, P.A., Krupenko, S.A., et al. (2008). A transcriptome database for astrocytes, neurons, and oligodendrocytes: a new resource for understanding brain development and function. J. Neurosci. *28*, 264–278.

Cantallops, I., Haas, K., and Cline, H.T. (2000). Postsynaptic CPG15 promotes synaptic maturation and presynaptic axon arbor elaboration in vivo. Nat. Neurosci. *3*, 1004–1011.

Cantera, R., and Nässel, D.R. (1992). Segmental peptidergic innervation of abdominal targets in larval and adult dipteran insects revealed with an antiserum against leucokinin I. Cell Tissue Res. *269*, 459–471.

Ceolin, L., Bouquier, N., Vitre-Boubaker, J., Rialle, S., Severac, D., Valjent, E., Perroy, J., and Puighermanal, E. (2017). Cell Type-Specific mRNA Dysregulation in Hippocampal CA1 Pyramidal Neurons of the Fragile X Syndrome Mouse Model. Front. Mol. Neurosci. *10*, 340.

Chan, H.Y., and Bonini, N.M. (2000). Drosophila models of human neurodegenerative disease.

Cell Death Differ. *7*, 1075–1080.

Chen, K., and Featherstone, D.E. (2005). Discs-large (DLG) is clustered by presynaptic innervation and regulates postsynaptic glutamate receptor subunit composition in Drosophila. BMC Biol. *3*, 1.

Chen, R., Wu, X., Jiang, L., and Zhang, Y. (2017). Single-Cell RNA-Seq Reveals Hypothalamic Cell Diversity. Cell Rep. *18*, 3227–3241.

Chen, X., Rahman, R., Guo, F., and Rosbash, M. (2016). Genome-wide identification of neuronal activity-regulated genes in Drosophila. Elife *5*.

Ch'ng, T.H., and Martin, K.C. (2011). Synapse-to-nucleus signaling. Curr. Opin. Neurobiol. *21*, 345–352.

Choi, J.C., Park, D., and Griffith, L.C. (2004). Electrophysiological and morphological characterization of identified motor neurons in the Drosophila third instar larva central nervous system. J. Neurophysiol. *91*, 2353–2365.

Chowdhury, S., Shepherd, J.D., Okuno, H., Lyford, G., Petralia, R.S., Plath, N., Kuhl, D., Huganir, R.L., and Worley, P.F. (2006). Arc/Arg3.1 interacts with the endocytic machinery to regulate AMPA receptor trafficking. Neuron *52*, 445–459.

Coe, B.P., Stessman, H.A.F., Sulovari, A., Geisheker, M.R., Bakken, T.E., Lake, A.M., Dougherty, J.D., Lein, E.S., Hormozdiari, F., Bernier, R.A., et al. (2019). Neurodevelopmental disease genes implicated by de novo mutation and copy number variation morbidity. Nat. Genet. *51*, 106–116.

Cole, A.J., Saffen, D.W., Baraban, J.M., and Worley, P.F. (1989). Rapid increase of an immediate early gene messenger RNA in hippocampal neurons by synaptic NMDA receptor activation. Nature *340*, 474–476.

Collins, C.A., and DiAntonio, A. (2007). Synaptic development: insights from Drosophila. Curr. Opin. Neurobiol. *17*, 35–42.

Combs, P.A., and Eisen, M.B. (2013). Sequencing mRNA from cryo-sliced Drosophila embryos to determine genome-wide spatial patterns of gene expression. PLoS One *8*, e71820.

Combs, P.A., and Eisen, M.B. (2015). Low-cost, low-input RNA-seq protocols perform nearly as well as high-input protocols. PeerJ *3*, e869.

Croset, V., Treiber, C.D., and Waddell, S. (2018). Cellular diversity in the Drosophila midbrain revealed by single-cell transcriptomics. Elife *7*.

Crossley, A.C. (1978). The morphology and development of the Drosophila muscular system. Genetics and Biology of Drosophila.

Cull‐Candy, S.G., Miledi, R., and Trautmann, A. (1980). On the release of transmitter at normal, myasthenia gravis and myasthenic syndrome affected human end‐plates. The Journal of.

Dale, H. (1935). Pharmacology and Nerve-Endings. Proc. R. Soc. Med. *28*, 319–332.

Daniels, R.W., Collins, C.A., Gelfand, M.V., Dant, J., Brooks, E.S., Krantz, D.E., and DiAntonio, A. (2004). Increased expression of the Drosophila vesicular glutamate transporter leads to excess glutamate release and a compensatory decrease in quantal content. J. Neurosci. *24*, 10466–10474.

Davis, G.W. (2006). Homeostatic control of neural activity: from phenomenology to molecular design. Annu. Rev. Neurosci. *29*, 307–323.

Davis, G.W. (2013). Homeostatic signaling and the stabilization of neural function. Neuron *80*, 718–728.

Davis, G.W., and Goodman, C.S. (1998). Genetic analysis of synaptic development and plasticity: homeostatic regulation of synaptic efficacy. Curr. Opin. Neurobiol. *8*, 149–156.

Davis, G.W., and Müller, M. (2015). Homeostatic control of presynaptic neurotransmitter release. Annu. Rev. Physiol. *77*, 251–270.

Davis, G.W., DiAntonio, A., Petersen, S.A., and Goodman, C.S. (1998). Postsynaptic PKA controls quantal size and reveals a retrograde signal that regulates presynaptic transmitter release in Drosophila. Neuron *20*, 305–315.

Deisseroth, K., Mermelstein, P.G., Xia, H., and Tsien, R.W. (2003). Signaling from synapse to nucleus: the logic behind the mechanisms. Curr. Opin. Neurobiol. *13*, 354–365.

DiAntonio, A., Petersen, S.A., Heckmann, M., and Goodman, C.S. (1999). Glutamate receptor expression regulates quantal size and quantal content at the Drosophila neuromuscular junction. J. Neurosci. *19*, 3023–3032.

Dietzl, G., Chen, D., Schnorrer, F., Su, K.-C., Barinova, Y., Fellner, M., Gasser, B., Kinsey, K., Oppel, S., Scheiblauer, S., et al. (2007). A genome-wide transgenic RNAi library for conditional gene inactivation in Drosophila. Nature *448*, 151–156.

Doe, C.Q. (1992). Molecular markers for identified neuroblasts and ganglion mother cells in the Drosophila central nervous system. Development *116*, 855–863.

Emes, R.D., Pocklington, A.J., Anderson, C.N.G., Bayes, A., Collins, M.O., Vickers, C.A., Croning, M.D.R., Malik, B.R., Choudhary, J.S., Armstrong, J.D., et al. (2008). Evolutionary expansion and anatomical specialization of synapse proteome complexity. Nat. Neurosci. *11*, 799–806.

Fioravante, D., and Regehr, W.G. (2011). Short-term forms of presynaptic plasticity. Curr. Opin.

Neurobiol. *21*, 269–274.

Fleischmann, A., Hvalby, O., Jensen, V., Strekalova, T., Zacher, C., Layer, L.E., Kvello, A., Reschke, M., Spanagel, R., Sprengel, R., et al. (2003). Impaired long-term memory and NR2A-type NMDA receptor-dependent synaptic plasticity in mice lacking c-Fos in the CNS. J. Neurosci. *23*, 9116–9122.

Fletcher, R.B., Das, D., Gadye, L., Street, K.N., Baudhuin, A., Wagner, A., Cole, M.B., Flores, Q., Choi, Y.G., Yosef, N., et al. (2017). Deconstructing Olfactory Stem Cell Trajectories at Single-Cell Resolution. Cell Stem Cell *20*, 817–830.e8.

Frank, C.A. (2014). Homeostatic plasticity at the Drosophila neuromuscular junction. Neuropharmacology *78*, 63–74.

Frank, C.A., Kennedy, M.J., Goold, C.P., Marek, K.W., and Davis, G.W. (2006). Mechanisms underlying the rapid induction and sustained expression of synaptic homeostasis. Neuron *52*, 663–677.

Frank, C.A., Wang, X., Collins, C.A., Rodal, A.A., Yuan, Q., Verstreken, P., and Dickman, D.K. (2013). New approaches for studying synaptic development, function, and plasticity using Drosophila as a model system. J. Neurosci. *33*, 17560–17568.

Fuzik, J., Zeisel, A., Máté, Z., Calvigioni, D., Yanagawa, Y., Szabó, G., Linnarsson, S., and Harkany, T. (2016). Integration of electrophysiological recordings with single-cell RNA-seq data identifies neuronal subtypes. Nat. Biotechnol. *34*, 175–183.

Gabel, H.W., Kinde, B., Stroud, H., Gilbert, C.S., Harmin, D.A., Kastan, N.R., Hemberg, M., Ebert, D.H., and Greenberg, M.E. (2015). Disruption of DNA-methylation-dependent long gene repression in Rett syndrome. Nature *522*, 89–93.

Gadye, L., Das, D., Sanchez, M.A., Street, K., Baudhuin, A., Wagner, A., Cole, M.B., Choi, Y.G., Yosef, N., Purdom, E., et al. (2017). Injury Activates Transient Olfactory Stem Cell States with Diverse Lineage Capacities. Cell Stem Cell *21*, 775–790.e9.

Gaviño, M.A., Ford, K.J., Archila, S., and Davis, G.W. (2015). Homeostatic synaptic depression is achieved through a regulated decrease in presynaptic calcium channel abundance. Elife *4*.

Geschwind, D.H., and Konopka, G. (2009). Neuroscience in the era of functional genomics and systems biology. Nature *461*, 908–915.

Gogliotti, R.G., Fisher, N.M., Stansley, B.J., Jones, C.K., Lindsley, C.W., Conn, P.J., and Niswender, C.M. (2018). Total RNA Sequencing of Rett Syndrome Autopsy Samples Identifies the M4 Muscarinic Receptor as a Novel Therapeutic Target. J. Pharmacol. Exp. Ther. *365*, 291–300.

Gonzalez, G.A., and Montminy, M.R. (1989). Cyclic AMP stimulates somatostatin gene

transcription by phosphorylation of CREB at serine 133. Cell *59*, 675–680.

Goold, C.P., and Davis, G.W. (2007). The BMP ligand Gbb gates the expression of synaptic homeostasis independent of synaptic growth control. Neuron *56*, 109–123.

Gorczyca, M., Augart, C., and Budnik, V. (1993). Insulin-like receptor and insulin-like peptide are localized at neuromuscular junctions in Drosophila. J. Neurosci. *13*, 3692–3704.

Granger, A.J., Wang, W., Robertson, K., El-Rifai, M., Zanello, A., Bistrong, K., Saunders, A., Chow, B., Nuñez, V., Gu, C., et al. (2018). Target-specific co-transmission of acetylcholine and GABA from a subset of cortical VIP+ interneurons.

Gratz, S.J., Rubinstein, C.D., Harrison, M.M., Wildonger, J., and O'Connor-Giles, K.M. (2015). CRISPR-Cas9 Genome Editing in Drosophila. Curr. Protoc. Mol. Biol. *111*, 31.2.1–31.2.20.

Greenberg, M.E., and Ziff, E.B. (1984). Stimulation of 3T3 cells induces transcription of the c-fos proto-oncogene. Nature *311*, 433–438.

Greenberg, M.E., Ziff, E.B., and Greene, L.A. (1986). Stimulation of neuronal acetylcholine receptors induces rapid gene transcription. Science *234*, 80–83.

Groth, A.C., Fish, M., Nusse, R., and Calos, M.P. (2004). Construction of transgenic Drosophila by using the site-specific integrase from phage phiC31. Genetics *166*, 1775–1782.

Grün, D., Lyubimova, A., Kester, L., Wiebrands, K., Basak, O., Sasaki, N., Clevers, H., and van Oudenaarden, A. (2015). Single-cell messenger RNA sequencing reveals rare intestinal cell types. Nature *525*, 251–255.

Guan, Z., Saraswati, S., Adolfsen, B., and Littleton, J.T. (2005). Genome-wide transcriptional changes associated with enhanced activity in the Drosophila nervous system. Neuron *48*, 91–107.

Guo, Y., Huang, S., de Pasquale, R., McGehrin, K., Lee, H.-K., Zhao, K., and Kirkwood, A. (2012). Dark exposure extends the integration window for spike-timing-dependent plasticity. J. Neurosci. *32*, 15027–15035.

Haghighi, A.P., McCabe, B.D., Fetter, R.D., Palmer, J.E., Hom, S., and Goodman, C.S. (2003). Retrograde control of synaptic transmission by postsynaptic CaMKII at the Drosophila neuromuscular junction. Neuron *39*, 255–267.

Hardingham, N., Wright, N., Dachtler, J., and Fox, K. (2008). Sensory deprivation unmasks a PKA-dependent synaptic plasticity mechanism that operates in parallel with CaMKII. Neuron *60*, 861–874.

Hartenstein, V., and Campos-Ortega, J.A. (1984). Early neurogenesis in wild-type Drosophila melanogaster. Wilehm Roux Arch Dev Biol *193*, 308–325.

Hashimshony, T., Wagner, F., Sher, N., and Yanai, I. (2012). CEL-Seq: single-cell RNA-Seq by multiplexed linear amplification. Cell Rep. *2*, 666–673.

Hawrylycz, M.J., Lein, E.S., Guillozet-Bongaarts, A.L., Shen, E.H., Ng, L., Miller, J.A., van de Lagemaat, L.N., Smith, K.A., Ebbert, A., Riley, Z.L., et al. (2012). An anatomically comprehensive atlas of the adult human brain transcriptome. Nature *489*, 391–399.

Hebb, D.O. (1949). The organization of behavior; a neuropsychological theory. *335*.

Hoang, B., and Chiba, A. (2001). Single-cell analysis of Drosophila larval neuromuscular synapses. Dev. Biol. *229*, 55–70.

Hodge, R.D., Bakken, T.E., Miller, J.A., Smith, K.A., Barkan, E.R., Graybuck, L.T., Close, J.L., Long, B., Johansen, N., Penn, O., et al. (2019). Conserved cell types with divergent features in human versus mouse cortex. Nature *573*, 61–68.

Hong, S.J., Li, H., Becker, K.G., Dawson, V.L., and Dawson, T.M. (2004). Identification and analysis of plasticity-induced late-response genes. Proc. Natl. Acad. Sci. U. S. A. *101*, 2145–2150.

Hook, P.W., McClymont, S.A., Cannon, G.H., Law, W.D., Morton, A.J., Goff, L.A., and McCallion, A.S. (2018). Single-Cell RNA-Seq of Mouse Dopaminergic Neurons Informs Candidate Gene Selection for Sporadic Parkinson Disease. Am. J. Hum. Genet. *102*, 427–446.

Hunt, S.P., Pini, A., and Evan, G. (1987). Induction of c-fos-like protein in spinal cord neurons following sensory stimulation. Nature *328*, 632–634.

Islam, S., Kjällquist, U., Moliner, A., Zajac, P., Fan, J.-B., Lönnerberg, P., and Linnarsson, S. (2011). Characterization of the single-cell transcriptional landscape by highly multiplex RNA-seq. Genome Res. *21*, 1160–1167.

Jan, L.Y., and Jan, Y.N. (1976a). Properties of the larval neuromuscular junction in Drosophila melanogaster. J. Physiol. *262*, 189–214.

Jan, L.Y., and Jan, Y.N. (1976b). L-glutamate as an excitatory transmitter at the Drosophila larval neuromuscular junction. J. Physiol. *262*, 215–236.

Johansen, J., Halpern, M.E., Johansen, K.M., and Keshishian, H. (1989). Stereotypic morphology of glutamatergic synapses on identified muscle cells of Drosophila larvae. J. Neurosci. *9*, 710–725.

Kalmbach, B.E., Buchin, A., Long, B., Close, J., Nandi, A., Miller, J.A., Bakken, T.E., Hodge, R.D., Chong, P., de Frates, R., et al. (2018). h-Channels Contribute to Divergent Intrinsic Membrane Properties of Supragranular Pyramidal Neurons in Human versus Mouse Cerebral Cortex. Neuron *100*, 1194–1208.e5.

Kauwe, G., and Isacoff, E.Y. (2013). Rapid feedback regulation of synaptic efficacy during

high-frequency activity at the Drosophila larval neuromuscular junction. Proc. Natl. Acad. Sci. U. S. A. *110*, 9142–9147.

Keshishian, H., Broadie, K., Chiba, A., and Bate, M. (1996). The drosophila neuromuscular junction: a model system for studying synaptic development and function. Annu. Rev. Neurosci. *19*, 545–575.

Kim, M.D., Wen, Y., and Jan, Y.-N. (2009). Patterning and organization of motor neuron dendrites in the Drosophila larva. Dev. Biol. *336*, 213–221.

Kirkwood, A., Rioult, M.C., and Bear, M.F. (1996). Experience-dependent modification of synaptic plasticity in visual cortex. Nature *381*, 526–528.

Klein, A.M., Mazutis, L., Akartuna, I., Tallapragada, N., Veres, A., Li, V., Peshkin, L., Weitz, D.A., and Kirschner, M.W. (2015). Droplet barcoding for single-cell transcriptomics applied to embryonic stem cells. Cell *161*, 1187–1201.

Kong, S.W., Sahin, M., Collins, C.D., Wertz, M.H., Campbell, M.G., Leech, J.D., Krueger, D., Bear, M.F., Kunkel, L.M., and Kohane, I.S. (2014). Divergent dysregulation of gene expression in murine models of fragile X syndrome and tuberous sclerosis. Mol. Autism *5*, 16.

Kurdyak, P., Atwood, H.L., Stewart, B.A., and Wu, C.F. (1994). Differential physiology and morphology of motor axons to ventral longitudinal muscles in larval Drosophila. J. Comp. Neurol. *350*, 463–472.

Kuromi, H., and Kidokoro, Y. (2000). Tetanic stimulation recruits vesicles from reserve pool via a cAMP-mediated process in Drosophila synapses. Neuron *27*, 133–143.

Lacar, B., Linker, S.B., Jaeger, B.N., Krishnaswami, S.R., Barron, J.J., Kelder, M.J.E., Parylak, S.L., Paquola, A.C.M., Venepally, P., Novotny, M., et al. (2016). Nuclear RNA-seq of single neurons reveals molecular signatures of activation. Nat. Commun. *7*, 11022.

Lai, S.-L., and Lee, T. (2006). Genetic mosaic with dual binary transcriptional systems in Drosophila. Nat. Neurosci. *9*, 703–709.

Landgraf, M., Bossing, T., Technau, G.M., and Bate, M. (1997). The origin, location, and projections of the embryonic abdominal motorneurons of Drosophila. J. Neurosci. *17*, 9642–9655.

Lanz, T.A., Guilmette, E., Gosink, M.M., Fischer, J.E., Fitzgerald, L.W., Stephenson, D.T., and Pletcher, M.T. (2013). Transcriptomic analysis of genetically defined autism candidate genes reveals common mechanisms of action. Mol. Autism *4*, 45.

Lein, E.S., Hawrylycz, M.J., Ao, N., Ayres, M., Bensinger, A., Bernard, A., Boe, A.F., Boguski, M.S., Brockway, K.S., Byrnes, E.J., et al. (2007). Genome-wide atlas of gene expression in the adult mouse brain. Nature *445*, 168–176.

Lerea, L.S., and McNamara, J.O. (1993). Ionotropic glutamate receptor subtypes activate c-fos transcription by distinct calcium-requiring intracellular signaling pathways. Neuron *10*, 31–41.

Li, H., Horns, F., Wu, B., Xie, Q., Li, J., Li, T., Luginbuhl, D.J., Quake, S.R., and Luo, L. (2017). Classifying Drosophila Olfactory Projection Neuron Subtypes by Single-Cell RNA Sequencing. Cell *171*, 1206–1220.e22.

Li, X., Goel, P., Wondolowski, J., Paluch, J., and Dickman, D. (2018). A Glutamate Homeostat Controls the Presynaptic Inhibition of Neurotransmitter Release. Cell Rep. *23*, 1716–1727.

Llorens-Bobadilla, E., Zhao, S., Baser, A., Saiz-Castro, G., Zwadlo, K., and Martin-Villalba, A. (2015). Single-Cell Transcriptomics Reveals a Population of Dormant Neural Stem Cells that Become Activated upon Brain Injury. Cell Stem Cell *17*, 329–340.

Lnenicka, G.A., and Keshishian, H. (2000). Identified motor terminals in Drosophila larvae show distinct differences in morphology and physiology. J. Neurobiol. *43*, 186–197.

Lobo, M.K., Karsten, S.L., Gray, M., Geschwind, D.H., and Yang, X.W. (2006). FACS-array profiling of striatal projection neuron subtypes in juvenile and adult mouse brains. Nat. Neurosci. *9*, 443–452.

Lopez, S.J., Dunaway, K., Islam, M.S., Mordaunt, C., Vogel Ciernia, A., Meguro-Horike, M., Horike, S.-I., Segal, D.J., and LaSalle, J.M. (2017). UBE3A-mediated regulation of imprinted genes and epigenome-wide marks in human neurons. Epigenetics *12*, 982–990.

Lott, S.E., Villalta, J.E., Schroth, G.P., Luo, S., Tonkin, L.A., and Eisen, M.B. (2011). Noncanonical compensation of zygotic X transcription in early Drosophila melanogaster development revealed through single-embryo RNA-seq. PLoS Biol. *9*, e1000590.

Lu, Z., Chouhan, A.K., Borycz, J.A., Lu, Z., Rossano, A.J., Brain, K.L., Zhou, Y., Meinertzhagen, I.A., and Macleod, G.T. (2016). High-Probability Neurotransmitter Release Sites Represent an Energy-Efficient Design. Curr. Biol. *26*, 2562–2571.

Lyford, G.L., Yamagata, K., Kaufmann, W.E., Barnes, C.A., Sanders, L.K., Copeland, N.G., Gilbert, D.J., Jenkins, N.A., Lanahan, A.A., and Worley, P.F. (1995). Arc, a growth factor and activity-regulated gene, encodes a novel cytoskeleton-associated protein that is enriched in neuronal dendrites. Neuron *14*, 433–445.

Lynch, G.S., Dunwiddie, T., and Gribkoff, V. (1977). Heterosynaptic depression: a postsynaptic correlate of long-term potentiation. Nature *266*, 737–739.

Macosko, E.Z., Basu, A., Satija, R., Nemesh, J., Shekhar, K., Goldman, M., Tirosh, I., Bialas, A.R., Kamitaki, N., Martersteck, E.M., et al. (2015). Highly Parallel Genome-wide Expression Profiling of Individual Cells Using Nanoliter Droplets. Cell *161*, 1202–1214.

Markstein, M., Pitsouli, C., Villalta, C., Celniker, S.E., and Perrimon, N. (2008). Exploiting position effects and the gypsy retrovirus insulator to engineer precisely expressed transgenes.

Nat. Genet. *40*, 476–483.

Marqués, G., and Zhang, B. (2006). Retrograde signaling that regulates synaptic development and function at the Drosophila neuromuscular junction. Int. Rev. Neurobiol. *75*, 267–285.

Mathys, H., Davila-Velderrain, J., Peng, Z., Gao, F., Mohammadi, S., Young, J.Z., Menon, M., He, L., Abdurrob, F., Jiang, X., et al. (2019). Single-cell transcriptomic analysis of Alzheimer's disease. Nature *570*, 332–337.

Mattei, D., Ivanov, A., Ferrai, C., Jordan, P., Guneykaya, D., Buonfiglioli, A., Schaafsma, W., Przanowski, P., Deuther-Conrad, W., Brust, P., et al. (2017). Maternal immune activation results in complex microglial transcriptome signature in the adult offspring that is reversed by minocycline treatment. Transl. Psychiatry *7*, e1120.

McGuire, S.E., Le, P.T., Osborn, A.J., Matsumoto, K., and Davis, R.L. (2003). Spatiotemporal rescue of memory dysfunction in Drosophila. Science *302*, 1765–1768.

Miller, K.D., and MacKay, D.J.C. (1994). The Role of Constraints in Hebbian Learning. Neural Comput. *6*, 100–126.

Monastirioti, M., Gorczyca, M., Rapus, J., Eckert, M., White, K., and Budnik, V. (1995). Octopamine immunoreactivity in the fruit fly Drosophila melanogaster. J. Comp. Neurol. *356*, 275–287.

Montminy, M.R., Low, M.J., Tapia-Arancibia, L., Reichlin, S., Mandel, G., and Goodman, R.H. (1986a). Cyclic AMP regulates somatostatin mRNA accumulation in primary diencephalic cultures and in transfected fibroblast cells. J. Neurosci. *6*, 1171–1176.

Montminy, M.R., Sevarino, K.A., Wagner, J.A., Mandel, G., and Goodman, R.H. (1986b). Identification of a cyclic-AMP-responsive element within the rat somatostatin gene. Proc. Natl. Acad. Sci. U. S. A. *83*, 6682–6686.

Morgan, J.I., Cohen, D.R., Hempstead, J.L., and Curran, T. (1987). Mapping patterns of c-fos expression in the central nervous system after seizure. Science *237*, 192–197.

Moulder, K.L., Meeks, J.P., Shute, A.A., Hamilton, C.K., de Erausquin, G., and Mennerick, S. (2004). Plastic elimination of functional glutamate release sites by depolarization. Neuron *42*, 423–435.

Moulder, K.L., Jiang, X., Taylor, A.A., Olney, J.W., and Mennerick, S. (2006). Physiological activity depresses synaptic function through an effect on vesicle priming. J. Neurosci. *26*, 6618–6626.

Nagasaka, Y., Dillner, K., Ebise, H., Teramoto, R., Nakagawa, H., Lilius, L., Axelman, K., Forsell, C., Ito, A., Winblad, B., et al. (2005). A unique gene expression signature discriminates familial Alzheimer's disease mutation carriers from their wild-type siblings. Proc. Natl. Acad.

Sci. U. S. A. *102*, 14854–14859.

Navin, N., Kendall, J., Troge, J., Andrews, P., Rodgers, L., McIndoo, J., Cook, K., Stepansky, A., Levy, D., Esposito, D., et al. (2011). Tumour evolution inferred by single-cell sequencing. Nature *472*, 90–94.

Nedivi, E., Hevroni, D., Naot, D., Israeli, D., and Citri, Y. (1993). Numerous candidate plasticity-related genes revealed by differential cDNA cloning. Nature *363*, 718–722.

Nedivi, E., Wu, G.Y., and Cline, H.T. (1998). Promotion of dendritic growth by CPG15, an activity-induced signaling molecule. Science *281*, 1863–1866.

Newman, Z.L., Hoagland, A., Aghi, K., Worden, K., Levy, S.L., Son, J.H., Lee, L.P., and Isacoff, E.Y. (2017). Input-Specific Plasticity and Homeostasis at the Drosophila Larval Neuromuscular Junction. Neuron *93*, 1388–1404.e10.

Ni, J.-Q., Markstein, M., Binari, R., Pfeiffer, B., Liu, L.-P., Villalta, C., Booker, M., Perkins, L., and Perrimon, N. (2008). Vector and parameters for targeted transgenic RNA interference in Drosophila melanogaster. Nat. Methods *5*, 49–51.

Ni, J.-Q., Liu, L.-P., Binari, R., Hardy, R., Shim, H.-S., Cavallaro, A., Booker, M., Pfeiffer, B.D., Markstein, M., Wang, H., et al. (2009). A Drosophila resource of transgenic RNAi lines for neurogenetics. Genetics *182*, 1089–1100.

Nicholson, L., Singh, G.K., Osterwalder, T., Roman, G.W., Davis, R.L., and Keshishian, H. (2008). Spatial and temporal control of gene expression in Drosophila using the inducible GeneSwitch GAL4 system. I. Screen for larval nervous system drivers. Genetics *178*, 215–234.

Nishimura, Y., Martin, C.L., Vazquez-Lopez, A., Spence, S.J., Alvarez-Retuerto, A.I., Sigman, M., Steindler, C., Pellegrini, S., Schanen, N.C., Warren, S.T., et al. (2007). Genome-wide expression profiling of lymphoblastoid cell lines distinguishes different forms of autism and reveals shared pathways. Hum. Mol. Genet. *16*, 1682–1698.

O'Brien, R.J., Kamboj, S., Ehlers, M.D., Rosen, K.R., Fischbach, G.D., and Huganir, R.L. (1998). Activity-dependent modulation of synaptic AMPA receptor accumulation. Neuron *21*, 1067–1078.

Orr, B.O., Fetter, R.D., and Davis, G.W. (2017). Retrograde semaphorin-plexin signalling drives homeostatic synaptic plasticity. Nature *550*, 109–113.

Oskvig, D.B., Elkahloun, A.G., Johnson, K.R., Phillips, T.M., and Herkenham, M. (2012). Maternal immune activation by LPS selectively alters specific gene expression profiles of interneuron migration and oxidative stress in the fetus without triggering a fetal immune response. Brain Behav. Immun. *26*, 623–634.

Paradis, S., Sweeney, S.T., and Davis, G.W. (2001). Homeostatic control of presynaptic release

is triggered by postsynaptic membrane depolarization. Neuron *30*, 737–749.

Patel, A.P., Tirosh, I., Trombetta, J.J., Shalek, A.K., Gillespie, S.M., Wakimoto, H., Cahill, D.P., Nahed, B.V., Curry, W.T., Martuza, R.L., et al. (2014). Single-cell RNA-seq highlights intratumoral heterogeneity in primary glioblastoma. Science *344*, 1396–1401.

Peled, E.S., and Isacoff, E.Y. (2011). Optical quantal analysis of synaptic transmission in wild-type and rab3-mutant Drosophila motor axons. Nat. Neurosci. *14*, 519–526.

Peled, E.S., Newman, Z.L., and Isacoff, E.Y. (2014). Evoked and spontaneous transmission favored by distinct sets of synapses. Curr. Biol. *24*, 484–493.

Penney, J., Tsurudome, K., Liao, E.H., Elazzouzi, F., Livingstone, M., Gonzalez, M., Sonenberg, N., and Haghighi, A.P. (2012). TOR is required for the retrograde regulation of synaptic homeostasis at the Drosophila neuromuscular junction. Neuron *74*, 166–178.

Perkins, L.A., Holderbaum, L., Tao, R., Hu, Y., Sopko, R., McCall, K., Yang-Zhou, D., Flockhart, I., Binari, R., Shim, H.-S., et al. (2015). The Transgenic RNAi Project at Harvard Medical School: Resources and Validation. Genetics *201*, 843–852.

Petersen, S.A., Fetter, R.D., Noordermeer, J.N., Goodman, C.S., and DiAntonio, A. (1997). Genetic analysis of glutamate receptors in Drosophila reveals a retrograde signal regulating presynaptic transmitter release. Neuron *19*, 1237–1248.

Pfeiffer, B.D., Ngo, T.-T.B., Hibbard, K.L., Murphy, C., Jenett, A., Truman, J.W., and Rubin, G.M. (2010). Refinement of tools for targeted gene expression in Drosophila. Genetics *186*, 735–755.

Plomp, J.J., van Kempen, G.T., and Molenaar, P.C. (1992). Adaptation of quantal content to decreased postsynaptic sensitivity at single endplates in alpha-bungarotoxin-treated rats. J. Physiol. *458*, 487–499.

Poulin, J.-F., Gaertner, Z., Moreno-Ramos, O.A., and Awatramani, R. (2020). Classification of Midbrain Dopamine Neurons Using Single-Cell Gene Expression Profiling Approaches. Trends Neurosci. *43*, 155–169.

Quinlan, E.M., Olstein, D.H., and Bear, M.F. (1999). Bidirectional, experience-dependent regulation of N-methyl-D-aspartate receptor subunit composition in the rat visual cortex during postnatal development. Proc. Natl. Acad. Sci. U. S. A. *96*, 12876–12880.

Ramsköld, D., Luo, S., Wang, Y.-C., Li, R., Deng, Q., Faridani, O.R., Daniels, G.A., Khrebtukova, I., Loring, J.F., Laurent, L.C., et al. (2012). Full-length mRNA-Seq from single-cell levels of RNA and individual circulating tumor cells. Nat. Biotechnol. *30*, 777–782.

Regehr, W.G. (2012). Short-term presynaptic plasticity. Cold Spring Harb. Perspect. Biol. *4*, a005702.

Reiter, L.T., Potocki, L., Chien, S., Gribskov, M., and Bier, E. (2001). A systematic analysis of human disease-associated gene sequences in Drosophila melanogaster. Genome Res. *11*, 1114–1125.

Rial Verde, E.M., Lee-Osbourne, J., Worley, P.F., Malinow, R., and Cline, H.T. (2006). Increased expression of the immediate-early gene arc/arg3.1 reduces AMPA receptor-mediated synaptic transmission. Neuron *52*, 461–474.

Rubin, G.M., and Spradling, A.C. (1982). Genetic transformation of Drosophila with transposable element vectors. Science *218*, 348–353.

Rubin, G.M., Yandell, M.D., Wortman, J.R., Gabor Miklos, G.L., Nelson, C.R., Hariharan, I.K., Fortini, M.E., Li, P.W., Apweiler, R., Fleischmann, W., et al. (2000). Comparative genomics of the eukaryotes. Science *287*, 2204–2215.

Rusak, B., Robertson, H.A., Wisden, W., and Hunt, S.P. (1990). Light pulses that shift rhythms induce gene expression in the suprachiasmatic nucleus. Science *248*, 1237–1240.

Saffen, D.W., Cole, A.J., Worley, P.F., Christy, B.A., Ryder, K., and Baraban, J.M. (1988). Convulsant-induced increase in transcription factor messenger RNAs in rat brain. Proc. Natl. Acad. Sci. U. S. A. *85*, 7795–7799.

Sando, R., 3rd, Gounko, N., Pieraut, S., Liao, L., Yates, J., 3rd, and Maximov, A. (2012). HDAC4 governs a transcriptional program essential for synaptic plasticity and memory. Cell *151*, 821–834.

Sanfeliu, A., Hokamp, K., Gill, M., and Tropea, D. (2019). Transcriptomic Analysis of Mecp2 Mutant Mice Reveals Differentially Expressed Genes and Altered Mechanisms in Both Blood and Brain. Front. Psychiatry *10*, 278.

Sasagawa, Y., Nikaido, I., Hayashi, T., Danno, H., Uno, K.D., Imai, T., and Ueda, H.R. (2013). Quartz-Seq: a highly reproducible and sensitive single-cell RNA sequencing method, reveals non-genetic gene-expression heterogeneity. Genome Biol. *14*, R31.

Schaefer, J.E., Worrell, J.W., and Levine, R.B. (2010). Role of intrinsic properties in Drosophila motoneuron recruitment during fictive crawling. J. Neurophysiol. *104*, 1257–1266.

Schmid, A., Chiba, A., and Doe, C.Q. (1999). Clonal analysis of Drosophila embryonic neuroblasts: neural cell types, axon projections and muscle targets. Development *126*, 4653–4689.

Schneggenburger, R., Sakaba, T., and Neher, E. (2002). Vesicle pools and short-term synaptic depression: lessons from a large synapse. Trends Neurosci. *25*, 206–212.

Scoville, W.B., and Milner, B. (1957). Loss of recent memory after bilateral hippocampal lesions. J. Neurol. Neurosurg. Psychiatry *20*, 11–21.

Shalek, A.K., Satija, R., Adiconis, X., Gertner, R.S., Gaublomme, J.T., Raychowdhury, R., Schwartz, S., Yosef, N., Malboeuf, C., Lu, D., et al. (2013). Single-cell transcriptomics reveals bimodality in expression and splicing in immune cells. Nature *498*, 236–240.

Shalek, A.K., Satija, R., Shuga, J., Trombetta, J.J., Gennert, D., Lu, D., Chen, P., Gertner, R.S., Gaublomme, J.T., Yosef, N., et al. (2014). Single-cell RNA-seq reveals dynamic paracrine control of cellular variation. Nature *510*, 363–369.

Sheng, M., Thompson, M.A., and Greenberg, M.E. (1991). CREB: a Ca(2+)-regulated transcription factor phosphorylated by calmodulin-dependent kinases. Science *252*, 1427–1430.

Shepherd, J.D., Rumbaugh, G., Wu, J., Chowdhury, S., Plath, N., Kuhl, D., Huganir, R.L., and Worley, P.F. (2006). Arc/Arg3.1 mediates homeostatic synaptic scaling of AMPA receptors. Neuron *52*, 475–484.

Shieh, P.B., Hu, S.C., Bobb, K., Timmusk, T., and Ghosh, A. (1998). Identification of a signaling pathway involved in calcium regulation of BDNF expression. Neuron *20*, 727–740.

Shu, H., Donnard, E., Liu, B., and Richter, J.D. (2019). Genetic Rescue of Fragile X Syndrome Links FMRP Deficiency to Codon Optimality-Dependent RNA Destabilization.

Smith, S.J., Sümbül, U., Graybuck, L.T., Collman, F., Seshamani, S., Gala, R., Gliko, O., Elabbady, L., Miller, J.A., Bakken, T.E., et al. (2019). Single-cell transcriptomic evidence for dense intracortical neuropeptide networks. Elife *8*.

Spradling, A.C., and Rubin, G.M. (1982). Transposition of cloned P elements into Drosophila germ line chromosomes. Science *218*, 341–347.

Südhof, T.C. (2013). Neurotransmitter release: the last millisecond in the life of a synaptic vesicle. Neuron *80*, 675–690.

Sugino, K., Hempel, C.M., Miller, M.N., Hattox, A.M., Shapiro, P., Wu, C., Huang, Z.J., and Nelson, S.B. (2006). Molecular taxonomy of major neuronal classes in the adult mouse forebrain. Nat. Neurosci. *9*, 99–107.

Tang, F., Barbacioru, C., Wang, Y., Nordman, E., Lee, C., Xu, N., Wang, X., Bodeau, J., Tuch, B.B., Siddiqui, A., et al. (2009). mRNA-Seq whole-transcriptome analysis of a single cell. Nat. Methods *6*, 377–382.

Tang, Y., Lu, A., Aronow, B.J., and Sharp, F.R. (2001). Blood genomic responses differ after stroke, seizures, hypoglycemia, and hypoxia: blood genomic fingerprints of disease. Ann. Neurol. *50*, 699–707.

Tao, X., Finkbeiner, S., Arnold, D.B., Shaywitz, A.J., and Greenberg, M.E. (1998). Ca2+ influx regulates BDNF transcription by a CREB family transcription factor-dependent mechanism. Neuron *20*, 709–726.

Tasic, B., Menon, V., Nguyen, T.N., Kim, T.K., Jarsky, T., Yao, Z., Levi, B., Gray, L.T., Sorensen, S.A., Dolbeare, T., et al. (2016). Adult mouse cortical cell taxonomy revealed by single cell transcriptomics. Nat. Neurosci. *19*, 335–346.

Tasic, B., Yao, Z., Graybuck, L.T., Smith, K.A., Nguyen, T.N., Bertagnolli, D., Goldy, J., Garren, E., Economo, M.N., Viswanathan, S., et al. (2018). Shared and distinct transcriptomic cell types across neocortical areas. Nature *563*, 72–78.

Thomas, E.A., Coppola, G., Desplats, P.A., Tang, B., Soragni, E., Burnett, R., Gao, F., Fitzgerald, K.M., Borok, J.F., Herman, D., et al. (2008). The HDAC inhibitor 4b ameliorates the disease phenotype and transcriptional abnormalities in Huntington's disease transgenic mice. Proc. Natl. Acad. Sci. U. S. A. *105*, 15564–15569.

Trapnell, C., Cacchiarelli, D., Grimsby, J., Pokharel, P., Li, S., Morse, M., Lennon, N.J., Livak, K.J., Mikkelsen, T.S., and Rinn, J.L. (2014). The dynamics and regulators of cell fate decisions are revealed by pseudotemporal ordering of single cells. Nat. Biotechnol. *32*, 381–386.

Treutlein, B., Brownfield, D.G., Wu, A.R., Neff, N.F., Mantalas, G.L., Espinoza, F.H., Desai, T.J., Krasnow, M.A., and Quake, S.R. (2014). Reconstructing lineage hierarchies of the distal lung epithelium using single-cell RNA-seq. Nature *509*, 371–375.

Turrigiano, G.G., Leslie, K.R., Desai, N.S., Rutherford, L.C., and Nelson, S.B. (1998). Activity-dependent scaling of quantal amplitude in neocortical neurons. Nature *391*, 892–896.

Tyssowski, K.M., DeStefino, N.R., Cho, J.-H., Dunn, C.J., Poston, R.G., Carty, C.E., Jones, R.D., Chang, S.M., Romeo, P., Wurzelmann, M.K., et al. (2018). Different Neuronal Activity Patterns Induce Different Gene Expression Programs. Neuron *98*, 530–546.e11.

Ugur, B., Chen, K., and Bellen, H.J. (2016). Drosophila tools and assays for the study of human diseases. Dis. Model. Mech. *9*, 235–244.

Velmeshev, D., Schirmer, L., Jung, D., Haeussler, M., Perez, Y., Mayer, S., Bhaduri, A., Goyal, N., Rowitch, D.H., and Kriegstein, A.R. (2019). Single-cell genomics identifies cell type-specific molecular changes in autism. Science *364*, 685–689.

Wang, X., Wang, Q., Engisch, K.L., and Rich, M.M. (2010). Activity-dependent regulation of the binomial parameters p and n at the mouse neuromuscular junction in vivo. J. Neurophysiol. *104*, 2352–2358.

Wu, Y.E., Pan, L., Zuo, Y., Li, X., and Hong, W. (2017). Detecting Activated Cell Populations Using Single-Cell RNA-Seq. Neuron *96*, 313–329.e6.

Zeisel, A., Muñoz-Manchado, A.B., Codeluppi, S., Lönnerberg, P., La Manno, G., Juréus, A., Marques, S., Munguba, H., He, L., Betsholtz, C., et al. (2015). Brain structure. Cell types in the mouse cortex and hippocampus revealed by single-cell RNA-seq. Science *347*, 1138–1142.

Zhong, S., Zhang, S., Fan, X., Wu, Q., Yan, L., Dong, J., Zhang, H., Li, L., Sun, L., Pan, N., et

al. (2018). A single-cell RNA-seq survey of the developmental landscape of the human prefrontal cortex. Nature *555*, 524–528.

Zito, K., Parnas, D., Fetter, R.D., Isacoff, E.Y., and Goodman, C.S. (1999). Watching a synapse grow: noninvasive confocal imaging of synaptic growth in Drosophila. Neuron *22*, 719–729.

Zucker, R.S. (1999). Calcium- and activity-dependent synaptic plasticity. Curr. Opin. Neurobiol. *9*, 305–313.

Zucker, R.S., and Regehr, W.G. (2002). Short-term synaptic plasticity. Annu. Rev. Physiol. *64*, 355–405.

Chapter 2:
Knockdown of release site stabilizing proteins results in transcriptional changes boosting excitability

This chapter contains co-authored material, representing a collaborative effort between myself, Zachary L. Newman, and Adam D. Hoagland. I contributed to the experimental design and execution of RNA-sequencing experiments, including VNC dissections, FACS, RNA-seq library preparation and quality control, and data analysis. Z.L.N. performed the SynapGCaMP recordings in the semi-intact larval preparation and optical quantal analysis. A.D.H. performed *in vivo* SynapGCaMP recordings, larval locomotion assay, and relevant data analysis.

Abstract

Stabilization of synaptic vesicle release sites is paramount for the fidelity of neurotransmission. However, less is known about the relationship between expression of SV release proteins and homeostatic mechanisms that compensate for such a perturbation in presynaptic function. We knockdown the expression of these proteins at the *Drosophila* NMJ with motor neuron-specific expression of dsRNAs against RIM-binding protein (Rbp) and Unc-13 (unc-13). We find that while activity-evoked neurotransmission is severely impaired, locomotion remains relatively normal. We find that diminished AP-evoked activity is compensated by an increase in neural activity and voltage-gated K+ channel expression.

Background

Homeostatic synaptic plasticity in neurons must balance excitability of the neuron with the efficiency and fidelity of synaptic transmission to maintain stable activity over a network of neurons (Turrigiano, 2012). These mechanisms are generally divided into postsynaptic or presynaptic mechanisms. While much is known about postsynaptic mechanisms of synaptic homeostasis, presynaptic mechanisms remain a challenge to study as presynaptic function is difficult to observe directly and must often be inferred from postsynaptic response. Thus, there is great interest in understanding how the function of molecular agents responsible for vesicle release at the presynapse might impact or be impacted by homeostatic programs.

The rapid release of synaptic vesicles (SVs) in response to neural activity is conducted at specialized domains in the presynaptic axon terminal known as active zones (AZs) (Südhof, 2012). The AZ cytomatrix facilitates docking and priming SV for rapid release upon action potential (AP) invasion and subsequent entry of Ca^{2+} via voltage-gated Ca^{2+} channels (VGCCs) (Südhof, 2012). Five key proteins form the core components of the AZ: RIM (Rab3-interacting molecule), unc-13, RIM-BP (Rbp), α-liprin, and ELKS proteins (Südhof, 2012). Two of these proteins, Rbp and unc-13, are primarily involved in vesicle docking and priming (Betz et al., 2001). However, recent experiments have shown that they also control the location and stability of SV release sites (Böhme et al., 2016; Liu et al., 2011; Reddy-Alla et al., 2017; Tang et al., 2016). We refer to these proteins as release site-stabilizing proteins (RSSPs).

As information regarding the molecular mechanism of RSSPs in SV release emerges, we became interested in the impact of RSSPs more broadly in neuronal function and on mechanisms of synaptic transmission resilience. Here, we describe the physiological and genetic consequences of RSSPs by knocking down expression with RNA interference in the *Drosophila* neuromuscular junction (NMJ). We find that, like previously characterized mutants, loss of RSSPs in the presynaptic motor neuron severely hampers AP-evoked neurotransmission without global alterations to locomotion. We find that compensation for such an extreme insult to synaptic function is mediated by an increase in neural activity via upregulation of voltage-gated K+ channels.

Results

Knockdown of RSSPs abrogates synaptic transmission at the NMJ but has no impact on global crawling behavior

Using traditional genetic tools to study the functional characteristics of RSSPs in *Drosophila* is challenging, as organism-wide loss of RSSPs is often lethal at the late embryonic stages (Aravamudan et al., 1999; Liu et al., 2011). Wishing to investigate the function of RSSPs in synaptic transmission, we knocked down expression in type I MNs with *UAS*-controlled dsRNA constructs against *Rbp* and *unc-13* using the motor-neuron specific *OK6-Gal4* line (Aberle et al., 2002; Sanyal, 2009). We found that these animals survive until the 3rd instar larval stage, allowing for characterization with electrophysiological and behavioral tools.

We functionally confirmed the loss of RSSPs by measuring AP-evoked transmission with optical quantal analysis. We accomplished this by expressing a postsynaptically-localized GCaMP6f sensor in the muscle (Newman et al., 2017). We found that knockdown of RSSPs (Rbp^{RNAi} data not shown) in motor neurons resulted in a 2.79-fold decrease in P_r in type Ib MNs and a 6.09-fold decrease in type Is MNs (Figure 2.1A). We observed reductions in quantal density (QD, area normalized quantal content) of similar magnitudes in each MN type (Figure 2.1B).

Reduction in AP-evoked release in RSSP knockdowns are in line with previous observations in *unc-13* null mutants and *Rbp* hypomorphs (Aravamudan et al., 1999; Liu et al., 2011). These mutants are also characterized by reduced locomotion. To assess the impact of RSSP loss by MN-specific knockdown, we devised an open field crawling test to assess locomotion over the course of a 10 minute trial. Larval crawling is well-described by a bimodal persistent random walk model, during which bouts of crawling along a continuous trajectory are punctuated by reorientation events (Günther et al., 2016). We applied this model to crawling trajectories of control and RSSP knockdown larvae. Shockingly, we found that the total distance traveled across the behavioral trial was unaltered in the RSSP knockdowns (Figure 2.1C). Similarly, we found no difference in time spent crawling along a continuous trajectory or during reorientation events between RSSP knockdowns and controls (Figure 2.1D).

RSSP loss in type I MNs results in an increase in presynaptic activity with no changes in postsynaptic Ca^{2+}

To determine whether or not this compensatory effect was occuring presynaptically or postsynaptically, we measured SynapGCaMP activity in intact, behaving larvae. We accomplished this by mounting 3rd instar larvae in a microfluidic chamber and restraining their crawling path to this space as described previously (Newman et al., 2017). In this experimental setup, spatially and temporally integrated ΔF/F values represent a measure of total postsynaptic response to excitatory drive. We found that RSSP knockdowns had similar postsynaptic response as *attP2* controls (Figure 2.1F). However, examining the ΔF/F traces of RSSP knockdowns, we found that they had greater excitatory drive, as measured by the amount of time spent at high ΔF/F values (>0.5 x $\Delta F/F_{max}$) (Figure 2.1G). We conclude from this that compensation induced by RSSP knockdown is presynaptic in origin.

RSSP loss results in altered expression of genes involved in membrane organization, peptidergic secretion, and neuronal remodeling

Wondering about what alterations are responsible for these apparent changes in synaptic transmission and neural activity, we devised a scheme to sequence the transcriptomes of type I MNs by expressing a nuclear mCherry reporter in the motor neuron-specific *OK6-Gal4* line and isolating mCherry-expressing cells by FACS (Figure 2.2A). We isolated RNA and prepared sequencing libraries from sorted cell samples. Principal component analysis of normalized libraries shows that the samples of each genotype cluster together, as expected. However, samples from *OK6>Rbp^{RNAi}(attP2)* and *OK6>unc-13^{RNAi}(attP2*) are located closer to each other on the first principal component (Figure 2.2B), indicating that the transcriptomes of RSSP knockdowns are more similar to each other than they are to controls.

We assessed the effectiveness of normalization by testing for differential expression of *UAS* transgenes and dsRNA-mediated knockdown as ground truths. While the *OK6>unc-13^{RNAi}(attP2)* samples have lower expression of the *UAS-Dcr-2* transgene, samples from all three genotypes have the similar expression of the *UAS-mCherry-NLS* reporter (Figure 2.2C-D). *OK6>Rbp^{RNAi}(attP2)* samples had a 2.5-fold decrease in *Rbp* expression compared to the *OK6>empty(attP2)* controls, while the *OK6>unc-13^{RNAi}(attP2)* samples had no difference in *Rbp* expression (Figure 2.2E). Curiously, both the *OK6>unc-13^{RNAi}(attP2)* and the *OK6>Rbp^{RNAi}(attP2)* had an approximately 2-fold decrease in *unc-13* expression (Figure 2.2F).

Intrigued by the finding that loss of *Rbp* resulted in a concomitant decrease in *unc-13*, we sought to broadly characterize the transcriptomic profile of each genotype. We found that the *OK6>Rbp^{RNAi}(attP2)* samples had a greater number (1311 vs 459) of DE genes compared to *OK6>unc-13^{RNAi}(attP2)* samples (Figure 2.3A). However, the majority of DE genes identified in the *OK6>unc-13^{RNAi}(attP2)* samples were also found to be differentially expressed in the *OK6>Rbp^{RNAi}(attP2)* (Figure 2.3A), suggesting that *Rbp* has an upstream genetic interaction with *unc-13*.

We next examined DE genes with increased expression in the context of presynaptic knockdown, and found that genes encoding neuropeptides were up-regulated in the *OK6>Rbp^{RNAi}(attP2)* and *OK6>unc-13^{RNAi}(attP2)* samples (Figure 2.3B-B', Tables 2.2-2.3). In *Drosophila* motor neurons, neuropeptides and other proteinaceous ligands (e.g. Wnt) are excreted from *Drosophila* motor neurons in large dense core vesicles or exosomes (Budnik et al., 2016; Richmond and Broadie, 2002). We also found that several genes in the tetraspanin family, which is broadly involved in membrane organization and trafficking, were up-regulated in the *OK6>Rbp^{RNAi}(attP2)* samples (Figure 2.3C, Table 2.2). Two of these tetraspanins were also up-regulated in the *OK6>unc-13^{RNAi}(attP2)* samples (Figure 2.3C', Table 2.3).

RSSP loss results in decreased expression of AZ structural components

Intrigued by the altered expression of genes involved in membrane dynamics, organization, and peptidergic signaling, we next asked how loss of either Rbp or unc-13 affects the expression of

other AZ components. We found decreased expression of *unc-13*, *cacophony* (*cac*), and *Rim* in both knockdown conditions, with *Rbp* and *straightjacket* (*stj*) down-regulated only in *OK6>Rbp^{RNAi}(attP2)* (Figure 2.4A-B). Since Rbp, unc-13, and RIM regulate coupling between synaptic vesicles (SVs) and Cac, decreased expression of these genes agrees with abrogation of AP-evoked release in the fillet preparation. Decreased *stj* expression is also concordant with our functional findings (Figure 2.4A), as *stj* mutants have impaired synaptic release and decreased expression of Cac (Dickman et al., 2008; Ly et al., 2008). Curiously, we noticed that loss of Rbp additionally results in increased expression of *complexin* (*cpx*), *Ras opposite* (*Rop*, mouse *Unc18*), *αSnap*, *comatose* (*comt*, mouse *Nsf*), and *Pka-C1* (Figure 2.4A). The protein products of each of these genes primarily act downstream of vesicle docking (Clary et al., 1990; Harrison et al., 1994; Ma et al., 2013; Söllner et al., 1993; Tang et al., 2006; Tolar and Pallanck, 1998).

Decreased RSSP expression results in decreased K+ channel expression

While it's possible that increased expression of some of these genes may compensate for impaired SV priming, these changes may not completely explain the resiliency of locomotion in RSSP knockdowns. Models of SV exocytosis suggest that priming, release site refractoriness, and attachment of vesicles to SNAREs near voltage-gated Ca^{2+} channels are the slowest steps of the SV release cycle (Pan and Zucker, 2009). In principle, increased levels of *Rop* and SNARE complex proteins (*comt* and *αSnap*) may boost priming and recovery from SV release, respectively. However, if docking is the rate-limiting step of SV exocytosis under RSSP knockdown, then increasing the efficiency of SV exocytosis downstream of this step would not result in a meaningful improvement in neurotransmission. This leaves us with two possible compensatory mechanisms that could result in normal locomotion: 1) increased firing inflates the number of opportunities for AP-evoked SV release or 2) the postsynapse increases its sensitivity to glutamate in response to reduced P_r. The latter of these two possibilities is less likely, as RSSP knockdowns have normal integrated postsynaptic calcium. We asked if the apparent increase in neural activity in the RSSP knockdown model can be explained by increased expression of voltage-gated ion channels.

We next examined differential expression of a complement of voltage-gated potassium channels and voltage-gated sodium channels, as these classes of ion channels are important determinants of excitability. We found that the delayed-rectifier *Shab* (Kv2) had ~60% expression in *OK6>Rbp^{RNAi}(attP2)* and *OK6>unc-13^{RNAi}(attP2)* samples compared to controls (Figure 2.5A-A'). While *Shaker* (*Sh*) expression at the mRNA level was unchanged across all genotypes, *Hyperkinetic* (*Hk*), which encodes the β subunit of the Sh (Kv1.1) channel, and *quiver* (*qvr*), a Ly6/GPI-anchored protein that regulates Sh expression, were down-regulated in both RSSP knockdowns (Figure 2.5A-A'). Similarly, *Shal* was not DE in either of RSSP knockdowns, but it's regulatory subunit, *SKIP* (Shal K+ channel interacting protein), is expressed at ~35% of controls (Figure 2.5A-A'). Expression of the voltage-gated sodium channel (*para*), it's auxiliary subunits (*tipE*, *Teh1*), or genetic regulators (*ps*) were unchanged in RSSP knockdowns (Figure 2.5B-B'). The biophysical properties of different voltage-gated K+ channels shape AP firing in motor neurons. Shab mediates K+ currents responsible for membrane repolarization after AP firing, while Sh and Shal mediate fast inactivating currents that increase the delay to first spike (Covarrubias et al., 1991; Peng and Wu, 2007). Thus, collective decrease in voltage-gated K+

channel would produce an increase in both resting membrane potential and spike initiation, biasing the motor neurons towards increased firing in RSSP knockdown.

Conclusions and Discussion

In these experiments, we characterize the functional and transcriptional consequences of presynaptic impairment by RNAi mediated knockdown of RSSPs. We find that while RSSP loss drastically reduces AP-evoked synaptic transmission in both type Ib and Is MNs, it has little impact on global locomotion behavior. These findings suggest that a homeostatic mechanism to allow relatively normal locomotion to occur despite impaired SV exocytosis. We characterized gene expression in RSSP knockdowns by RNA-sequencing and found decreased expression of voltage-gated K+ channels, which predict a bias towards excitability and may be an important element in compensating for RSSP loss.

Presynaptic silencing as a bidirectional regulatory pathway

Motor neuron-specific RSSP knockdown NMJs phenocopy the reduction of AP-evoked release in *unc-13* mutant synapses both in *Drosophila* and in mammals (Aravamudan et al., 1999; Augustin et al., 1999). This is thought to be the result of defects in synaptic vesicle priming, as application of α-latrotoxin, which stimulates vesicle exocytosis (Krasnoperov et al., 1997), to *Munc-13* mutant hippocampal neurons still results in SV release (Augustin et al., 1999). This functional phenotype is akin to another model of synaptic homeostasis known as presynaptic silencing. Presynaptic silencing was first observed in dissociated mammalian neurons after being cultured in elevated concentrations of extracellular K+ (Moulder et al., 2004, 2006). Elevated K+ concentrations result in chronic depolarization and trigger a compensatory decrease in AP-evoked release, which can be reversed by blockade of APs but is unaltered by changes in postsynaptic glutamate receptor activity (Moulder et al., 2003, 2004, 2006). Deficits in AP-evoked release in this homeostatic model are also attributed to deficits in priming, as SV release can also be triggered by α-latrotoxin (Moulder et al., 2006).

Since our RNA-sequencing results of motor neurons subject to RSSP knockdown have gene expression changes that bias cells toward excitation, we propose that homeostatic mechanisms like presynaptic silencing are bidirectional. In such a model, increased excitability results in adaptive suppression of AP-evoked release, while loss of RSSP function results in a compensatory increase in excitability. This might also explain the befuddling decrease in AZ component expression in RSSP knockdown motor neurons, as K+ induced presynaptic silencing results in decreased expression of both Munc-13 and RIM in mammalian neurons (Jiang et al., 2010).

Differentiating between general responses and specific responses to various modes of synaptic insult

One of the challenges of identifying homeostatic mechanisms with exploratory methods, such as RNA-sequencing, is that it can be difficult to differentiate between instructive and consequential changes in gene expression. We observe increased expression of neuropeptides, tetraspanins, and

voltage-gated K+ channels in RSSP knockdown motor neurons, features which are shared by another presynaptic homeostatic model which results in increased P_r and quantal content (see Chapter 3). However, ultrastructural analysis of *unc-13* mutants shows an increase in SV in the presynaptic volume of both vertebrate and invertebrate neurons (Aravamudan et al., 1999; Augustin et al., 1999). We find it fitting that in RSSP knockdown motor neurons there is increased expression of proteins involved in membrane organization, exosome trafficking, multivesicular body formation (MVB) and large dense-core vesicles.

The literature on the involvement of MVB formation specifically in neurons suggest that increased MVB formation is a general response to synaptic insult (Birks et al., 1972; Cavalli et al., 2005). Increased size or number of MVBs has even been observed in response to increased electrical activity either by electrical stimulation or genetic mutation, as in the *Drosophila eag Sh* double-mutant (Jia et al., 1993; Kadota et al., 1994). Most homeostatic mechanisms that stabilize firing and presynaptic SV release are thought to be specialties of neurons, however MVB and exosome trafficking is an output of homeostatic processes outside the nervous system (Desdín-Micó and Mittelbrunn, 2017). While there is no obvious link between this phenomenon and the functional outcomes of RSSP loss as measured by synaptic activity, we can't necessarily exclude its involvement in homeostatic compensation.

Methods

Fly Stocks

The *UAS-Rbp*^{RNAi} line (TRiP.JF02471, BDSC #29331), *UAS-unc-13*^{RNAi} line (TRiP.JF02440, BDSC #29548), and the empty *attP2* acceptor line (BDSC #36303) were obtained from the Bloomington Drosophila Stock Center as donated by the Transgenic RNAi Project. *UAS-dsRNA* constructs were driven in type I MNs with *OK6-Gal4* (Aberle et al., 2002; Sanyal, 2009). *UAS-Dcr2* (BDSC #24646) was used to improve the efficacy of RNA interference (Dietzl et al., 2007). Fruit fly stocks bearing a synaptically-localized GCaMP6f (*SynapGCaMP*) under the control of the myosin heavy-chain (*MHC*) promoter were used for reporting postsynaptic activity in the muscle (Newman et al., 2017) in electrophysiology experiments. For RNA-sequencing experiments, fruit fly stocks bearing transgenes encoding nuclear mCherry (*UAS-mCherry-NLS*; (Caussinus et al., 2008), BDSC #38424), along with Dcr2 and dsRNA constructs, in type I MNs were used for the purpose of FACS sorting.

Larvae were raised to the 3rd instar stage on cornmeal and molasses media in an incubator at 25°C for RNA-seq experiments and at 29°C for behavioral experiments. Female parents bearing the *OK6-Gal4* driver and *UAS-Dcr2* transgenes were crossed with male parents bearing either the *attP2* empty vector or RNAi construct to obtain control and knockdown progeny, respectively.

Fruit fly 3rd instar larva with the following genotypes were used for experiments described in this chapter:

UAS-Dcr2;OK6-Gal4/+;UAS-mCherry-NLS/(attP2) (*abbr. OK6>empty(attP2)*)

UAS-Dcr2;OK6-Gal4/+;UAS-mCherry-NLS/UAS-Rbp^{RNAi}(attP2) (abbr. *OK6>Rbp^{RNAi}(attP2)*)
UAS-Dcr2;OK6-Gal4/+;UAS-mCherry-NLS/UAS-unc-13^{RNAi}(attP2) (abbr. *OK6>unc-13^{RNAi}(attP2)*)
UAS-Dcr2;OK6-Gal4/+;MHC-SynapGCaMP/(attP2)
UAS-Dcr2;OK6-Gal4/+;MHC-SynapGCaMP/UAS-Rbp^{RNAi}(attP2)
UAS-Dcr2;OK6-Gal4/+;MHC-SynapGCaMP/UAS-unc-13^{RNAi}(attP2)

SynapGCaMP Imaging in Fillet Preparation

Standard fillet preparations were performed on 3rd instar larvae in HL3 solution (Stewart et al., 1994) with 0.45 mM Ca^{2+} and 20 mM Mg^{2+}. Just prior to recording, the brain and VNC were removed from the fillet preparation. Samples were washed and put into a recording HL3 solution with 1.5 mM Ca^{2+} and 25 mM Mg^{2+}. Optical recording of SynapGCaMP activity was performed on muscle 4 NMJs from segments A2-A5. Fluorescence images were acquired on a Vivo Spinning Disk Confocal microscope (3i Intelligent Imaging Innovation) system outfitted with a 63x 1.0 NA water immersion objective (Zeiss), LaserStack 488 nm (50 mW) laser, a Yokogawa CSU-X1 A1 spinning disk, a GFP excitation/emission filter set, and a Photometrics Evolve EMCCD camera. The imaged areas were selected so that both type Ib and Is terminals could be viewed together within a single focal plane.

Evoked activity was achieved with nerve stimulation by suction electrode attached to a Stimulus Isolation Unit (Iso-Flex, A.M.P.I) with a 75-100 μs stimulus duration. The stimulation protocol was synchronized with imaging episodes (SlideBook, v6.0.9, 3i Intelligent Imaging Innovations) using a custom Matlab script (Matlab Version R2015b and Image Processing Toolbox Release R2015b, MathWorks, Inc.). Low-frequency episodic stimulation (0.1 Hz) involved acquiring 10 frames (20 Hz) after application of a stimulus pulse. Each stimulus episode was preceded by 3-4 frames of baseline fluorescence images for intensity normalization. Each low-frequency stimulation epoch consisted of 200 stimulus trials.

Optical Quantal Analysis of SynapGCaMP Activity

Optical quantal analysis was performed as described previously (Newman et al., 2017) using custom Matlab scripts. High frequency noise was reduced with a first-pass Gaussian filter. Type Ib and Is terminals were split into separate regions of interest based on their baseline SynapGCaMP signal. Images were registered by calculating the 2D cross-correlation between the first frame of each episode to a reference frame. Trials during which the NMJ drifted out of focus or otherwise failed to register were excluded from analysis. Pixel intensities were corrected for bleaching by fitting baseline and post-activity fluorescence data to a double exponential curve.

Stimulation-evoked responses were identified by calculating the average ΔF responses for > 20 manually-selected spots of SynapGCaMP activity for each frame of the stimulus trial to serve as a template response. Response images were obtained by calculating pixel-wise ΔF values and dividing by the baseline fluorescence image (ΔF/F). Responsive pixels were identified by cross-covariance to the template response or having ΔF/F values greater than 1.5 standard

deviations above the average intensity for that pixel across the time series. Active pixels were grouped into ΔF/F spots were thresholded for amplitude and area to remove spurious events.

The P_r values of individual release sites were calculated by first smoothing with a Gaussian filter, and then calculating the local maximum of each ΔF/F spot. The probability of response was calculated by dividing the number of times activity appeared within a 4x4 or 5x5 pixel neighborhood of each ΔF/F spot by the number of stimulus trials in the experiment. Quantal density, defined as area-normalized quantal content, was determined by the average number of identified ΔF/F spots across stimulus trials divided by the imaged area.

In vivo SynapGCaMP Imaging

3rd instar larvae were staged and placed in a PDMS chamber for imaging *in vivo* activity of SynapGCaMP as described previously (Newman et al., 2017). A coverslip was affixed over the top of the PDMS chamber to subject the larvae to restrained crawling. We imaged changes in fluorescence of type Ib boutons on dorsal muscles 1, 2, 9, and 10 from either the T3 or A1 segment over a period of 1-2 minutes with a 50 ms exposure time on a Zeiss ZEISS Axio Zoom v16 FL microscope outfitted with a 2.3X 0.57 NA objective, a FS 38 HE filter set (Zeiss, excitation: 470/40HE, emission: 525/50HE), and an AxioCam Hr 38 camera. Movies where the synapses drift out of frame or out of focus were excluded from analysis.

Analysis of *In vivo* SynapGCaMP Imaging

Images of synaptic activity were analyzed with custom Matlab scripts. Images were registered in a multi-step process where correction for rigid translations was obtained by calculating the maximum 2D cross-correlation across successive frames and determining the offsets in x and y. Motion by warping and shearing of boutons during muscle contraction was corrected with affine and diffeomorphic registration algorithms (Lombaert et al., 2014). ΔF/F traces were calculated by first subtracting background fluorescence from nearby regions of muscle not containing synapses before calculating changes in fluorescence within each ROI (typically a single NMJ) over the time series.

Periods of activity were defined by binning ΔF/F traces into 100 linearly spaced bins. Low activity was defined as ΔF/F values falling within the bottom 25 bins. Periods of high activity are more variable, but are defined here as ΔF/F values surpassing the 50th bin ($0.5x\Delta F/F_{max}$). We represented neural activity by calculating the amount of time ΔF/F values exceeded this high-state threshold over the course of the time series. Synaptic activity is defined as the integrated ΔF/F values across the pixels assigned to each NMJ over all frames of the movie ($\Sigma\Sigma(\Delta F/F)\Delta p\Delta t$). A detailed description of these methods can be found Newman *et al.*, 2017.

Larval Locomotion Assay

Multiplexed tracking of crawling larvae was accomplished by outfitting a 6-well plate filled with 2% agarose gel leaving. A gap of approximately 3 mm was left between the surface of the agarose and the cusp of the well to minimize the movement of larvae in the z-direction. A single

larva was placed in each well of the plate for tracking individual animals. Larvae were filmed crawling for a single 10 minute trial at a rate of 10 fps backlit with an IR LED array. The imaging chamber was kept at 21 °C and illuminated with a 60W incandescent bulb.

Movies were processed with custom Matlab routines to assess two main features of larval locomotion, bouts of crawling along a continuous trajectory and reorientation events, as described previously (Günther et al., 2016). Trajectories of each larvae were calculated with a 2D centroid tracking algorithm. Centroids within 1 mm of each other across a 2 second window were merged by calculating the center of mass value, reducing noise in the crawling trajectory. Reorientation events were scored by fitting a 3rd degree polynomial along the length of the larva and calculating the curvature. Curvature values were low-pass filtered, and a reorientation event was scored when curvature exceeded the middle quartile value calculated across the entire movie for a duration of at least 2 s. Total distance traveled was determined from the length of the trajectory over the course of the experiment. Time spent during reorientation events was calculated from the number of centroids used to calculate a smoothed point scored as a reorientation event. Time spent crawling on a continuous trajectory was calculated from the time in between reorientation events, excluding periods where the larva stopped crawling.

CNS Dissection

Prior to dissection 3rd instar larva were screened for the presence of nuclear mCherry in the VNC with ZEISS Axio Zoom v16 FL epifluorescence microscope. For bulk RNA-sequencing experiments, larvae were rinsed twice in 1X PBS (Gibco), once in 70% ethanol, and again in 1X PBS to sterilize the surface of the animals. Larvae were dissected on a Sylgard pad in a droplet of Schneider's complete media (Gibco) supplemented with 10% FBS (Corning) and 1% PenStrep (Gibco). After removing extraneous tissues, the brain and VNC were transferred to a low-binding 1.5 mL tube containing Schneider's complete media on ice until dissociation. Dissected tissues were kept on ice prior to dissociation no longer than 60 minutes to ensure the viability of the cells during FACS sorting.

CNS Dissociation

Tissue samples were washed three times with 500 µL Schneider's media containing 1.5 mM EDTA and 1.5 mM L-Cysteine to remove media containing FBS. Fresh dissociation solution was prepared for each experiment from Schneider's media with the following additives: 1.5 mM EDTA, 1.5 mM L-Cysteine, papain (Worthington), and 1.25 mg/mL collagenase type-I (MilliporeSigma). Tissue samples were transferred into the dissociation solution and incubated at 25°C on a nutator for 5 minutes. Samples were triturated 30 times with a P200 pipette tip. This process of incubation and trituration was repeated before a final step in which tissue was sheared 7 times with a 27G1/2 needle.

The digestion reaction was quenched with the addition of 500 µL Schneider's complete media with 10% FBS and 1% PenStrep. Dissociated cells were passed through a 40 µm cell strainer (Falcon) and transferred to a low-binding 1.5 mL tube. The processed sample was centrifuged at

0.7 x *g* for 7 minutes, after which the supernatant was replaced with 1 mL of Schneider's complete media containing 5% FBS and 1% PenStrep.

Fluorescence Activated Cell Sorting

Processed cell samples were stained with 0.3 μM Sytox Green (Molecular Probes) to assay cell viability prior to sorting. Cells were sorted on a BD Influx Cell Sorter with 140 μm tubing at pressures < 12 PSI. The sorted population was chosen for high expression of nuclear mCherry (PE-Texas Red) and low Sytox Green fluorescence (GFP). Plots of FACS data were created using the flowCore (ver 1.52.1, Hahne et al., 2009) and ggcyto packages (ver 1.14.0, Van et al., 2018).

Low-input RNA-Seq Library Preparation and Sequencing

Cells were sorted into RLT lysis buffer (RNeasy Micro, QIAGEN) supplemented with 3.5 mM BME. Cells were lysed by vortexing for 30 seconds at room temperature. RNA extraction was performed according to RNEasy Micro kit protocol, omitting the DNase digestion step. Extracted RNA was checked for quality by an Agilent 2100 Expert Bioanalyzer with a Eukaryote Total RNA Pico chip.

RNA was annealed to an oligo-dT primer (5'-AAGCAGTGGTATCAACGCAGAGTACT$_{30}$VN-3', IDT) in a buffer containing 2.5 mM dNTPs and recombinant RNase Inhibitor (Takara). First-strand synthesis was performed with the SuperScriptII kit using a custom template-switching oligo (5'-/5Me-isodC//iisodG//iMe-isodC/AAGCAGTGGTATCAACGCAGAGTACATrGrGrG-3', IDT) with 5' modifications to avoid the creation of concatemers in low input samples (Kapetyn et al., 2010). cDNA preamplification, lambda exonuclease (New England Biolabs) digestion, size-selection with AMPure XP beads (Agencourt) were performed as described previously (Li et al., 2016). Libraries were constructed from preamplified cDNA using the Nextera XT kit (Illumina) and size-selected with AMPure XP beads. Fragments above 700 bps were excluded with Pippin Prep (SAGE Biosciences). Indexed libraries were sequenced on Illumina Hi-Seq 4000 sequencers to produce 100 nt paired-end reads.

RNA-Seq Alignment and Pre-processing

Demultiplexed .fastq files were first analyzed with FastQC (ver 0.11.7, Andrews, 2010) to check for quality and trimmed with Trimmomatic (ver 0.38, Bolger et al., 2014). Trimmed reads were aligned to a custom reference genome built from Berkeley Drosophila Genome Project (dm6, release 98) genome assembly and the pUAST-mCherry-NLS vector sequence for the detection of the mCherry mRNA reads. Samples bearing dsRNA constructs were mapped to custom genomes containing the aforementioned transgenes and the sequence of the dsRNA construct. Mapping was performed with HISAT2 (ver 2.1.0, Kim et al., 2019) and the counts matrix was generated with the featureCounts function from the Subread package (ver 1.6.4, Liao et al., 2014).

Gene Filtering and Normalization

Biological analysis was performed in R after using a custom script to import the featureCounts output into a SummarizedExperiment object (ver 1.16.1, Huber et al., 2015). Genes with fewer than 5 counts across 2 libraries were considered undetectable and removed from downstream analysis. Libraries were normalized by estimating factors of unwanted variation as implemented in the RUVg function in RUVSeq (Risso et al., 2014). A set of 600 housekeeping genes identified from RNA-sequencing data from a variety of *Drosophila* L3 tissues were used as negative control genes (Brown et al., 2014; Celniker et al., 2009). Details the identification of housekeeping genes and the efficacy of this normalization procedure are explained in detail in Appendix 1.

Differential Expression Testing and Visualization

Identification of differentially expressed (DE) genes between each knockdown condition was performed with the DESeq2 (ver 1.26.0, Love et al., 2014). Visualization of DE analysis was performed with custom scripts built upon ggplot2 (ver 3.2.1, Wickham, 2010).

Code availability

Code used for all RNA-seq data analysis steps will be available in a Github repository at https://github.com/isacofflab/presynap_MN upon publication.

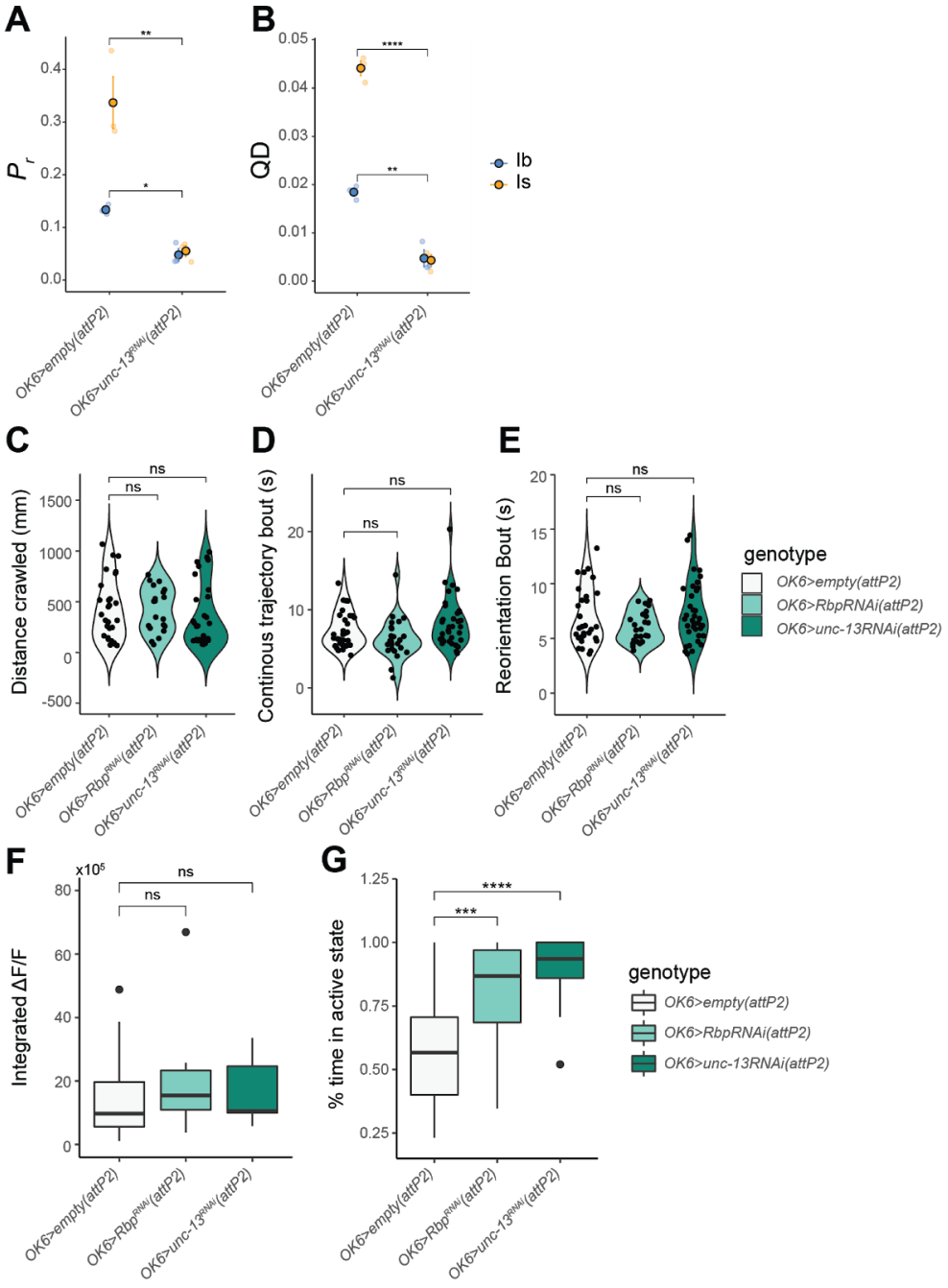

Figure 2.1) Loss of RSSPs results in severe deficits in SV release and an increase in neural activity, but no change in locomotion. **A**) Mean single-synapse P_r by NMJ of muscle 4 type Ib MNs (blue) and type Is MNs (orange) in *OK6>empty(attP2)* controls and *OK6>unc-13^{RNAi}(attP2)* larvae. **B**) Quantal density (QD) by NMJ of muscle 4 type Ib MNs (blue) and type Is MNs (orange) in *OK6>empty(attP2)* controls and *OK6>unc-13^{RNAi}(attP2)* larvae. (Points with black outline in (**A-B**) are mean ± SEM (*OK6>empty(attP2)* Ib MNs n = 3 NMJs, n = sites; *OK6>empty(attP2)* Is MNs n = 3 NMJs, n = sites; *OK6>unc-13^{RNAi}(attP2)* Ib MNs n = 3 NMJs, n = 154 sites; *OK6>unc-13^{RNAi}(attP2)* Is MNs n = 3 NMJs, n = 93 sites). **C-E**) Measures

of locomotion in *OK6>empty(attP2)* controls (gray) compared *OK6>Rbp^{RNAi}(attP2)* (light green) and *OK6>unc-13^{RNAi}(attP2)* (dark green) animals. **C**) Distance crawled (mm) over the course of the behavioral trial. **D**) Time spent crawling on a continuous trajectory (s). **E**) Duration of reorientation bouts (s). Solid black points are mean values of individual animals. (*OK6>empty(attP2)* n = 30 larvae, *OK6>Rbp^{RNAi}(attP2)* n = 24 larvae, *OK6>unc-13^{RNAi}(attP2)* n = 36 larvae). **F-G)** *In vivo* measurement of SynapGaMP ΔF/F responses to restrained crawling in RSSP knockdowns. **F)** Integrated postsynaptic SynapGCaMP response (ΣΣ(ΔF/F)ΔpΔt). **G)** Percent time in ΔF/F trace spent at >50% $\Delta F/F_{max}$ (*OK6>empty(attP2)* n = 28 NMJs, *OK6>Rbp^{RNAi}(attP2)* n = 18 NMJs, *OK6>unc-13^{RNAi}(attP2)* n = 11 NMJs). (Tests for significance: **A-B**, Welch's *t*-test; **C-G**, ANOVA with Dunnett's *post-hoc* test. Indicators of significance for all panels: ns $p > 0.05$, * $p < 0.01$, ** $p < 0.001$, *** $p < 0.0001$, **** $p <$ 1e-05).

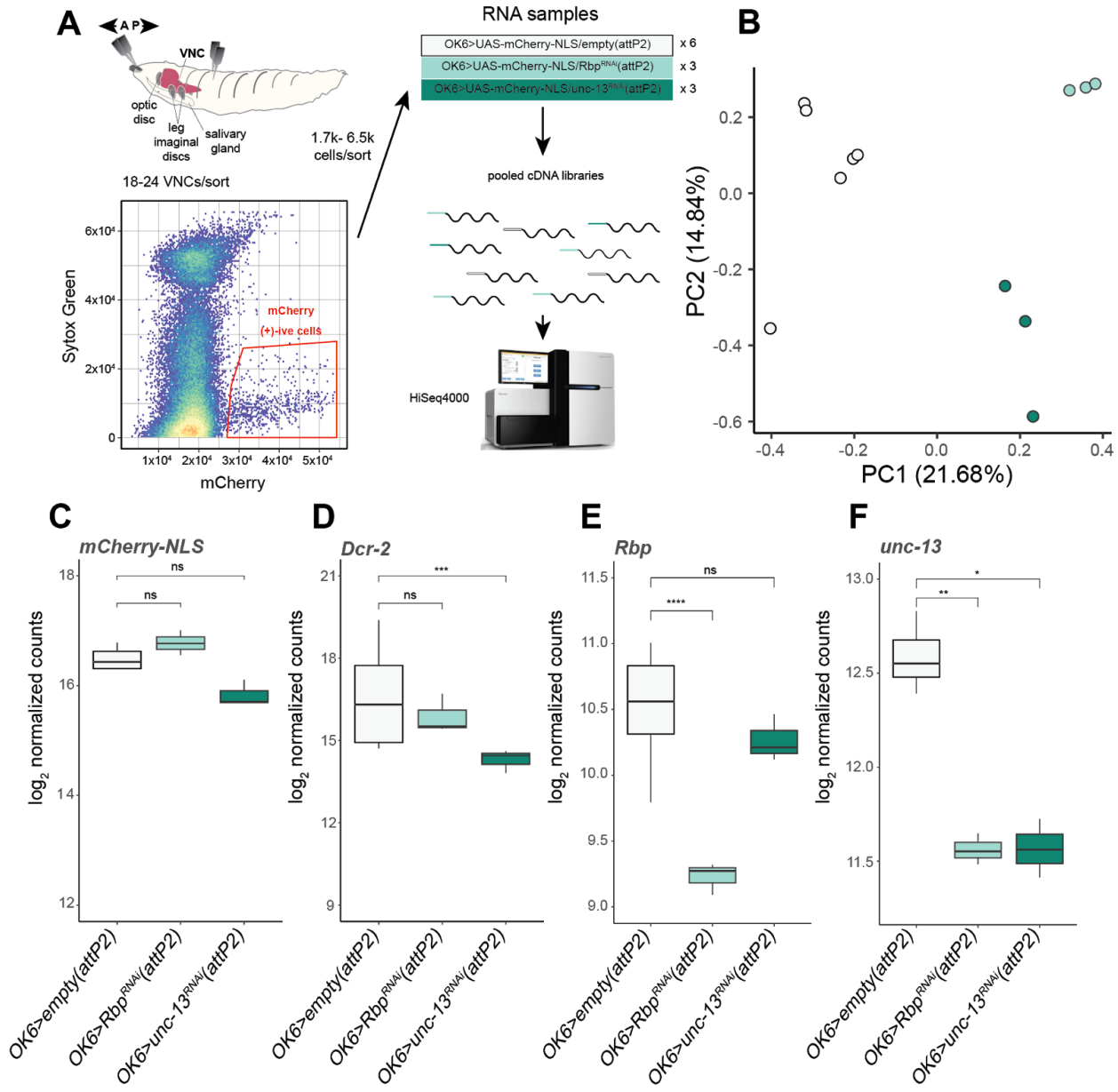

Figure 2.2) Knockdown RSSPs produce transcriptionally similar phenotypes. **A**) Schematic for generating RNA-seq libraries from sorted motor neuron populations from control (*OK6>empty(attP2)*) and RNAi (*OK6>Rbp^{RNAi}(attP2)*, *OK6>unc-13^{RNAi}(attP2)*) animals. **B**) Principal component analysis (PCA) plot of RNA-seq samples points colored as depicted in **A**. Axes are annotated by percent variance explained for each principal component. **C-F**) Boxplots of log2 normalized pseudocount expression of **C**) *mCherry-NLS*, **D**) *Dcr-2*, **E**) *Rbp*, and **F**) *unc-13* (BH-adjusted Wald test *p*-values, ns $p > 0.05$, * $p < 0.01$, ** $p < 0.001$, *** $p < 0.0001$, **** $p <$ 1e-05).

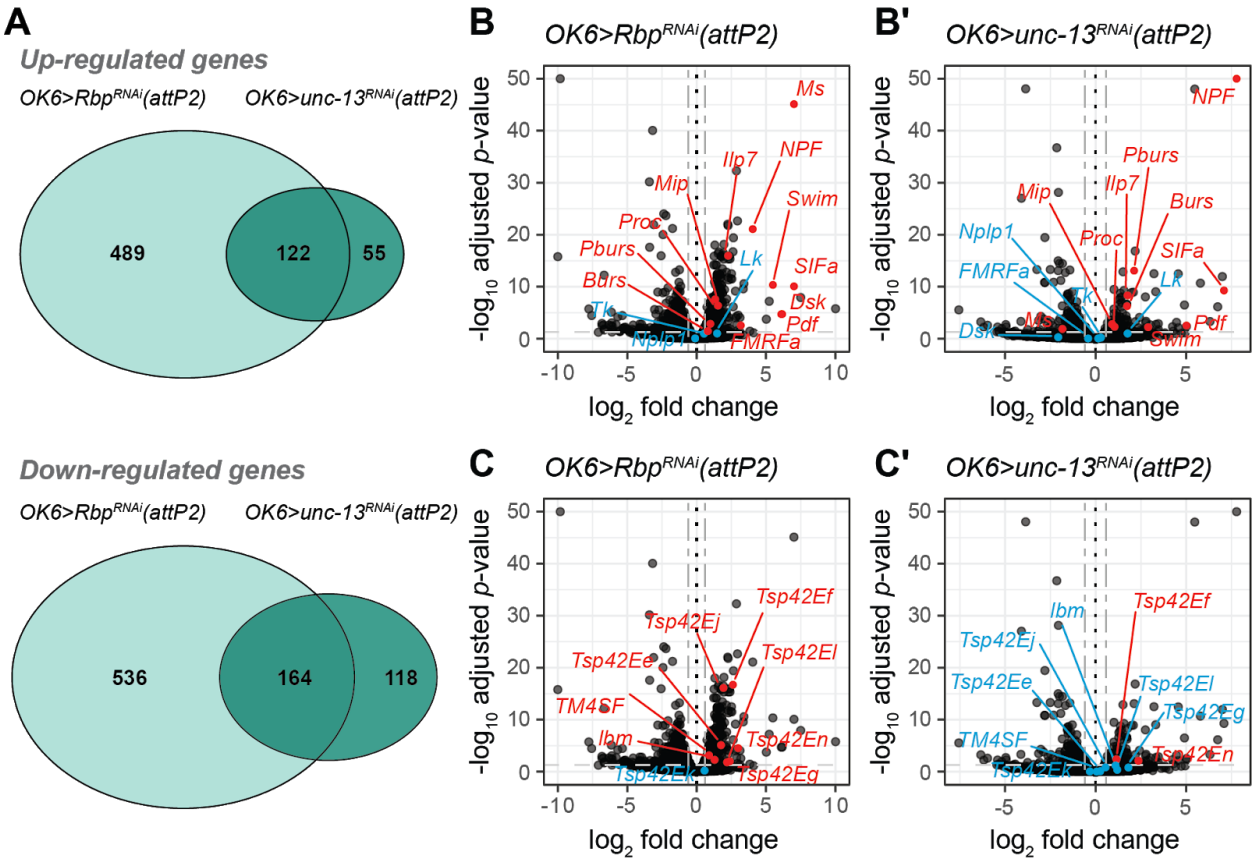

Figure 2.3) Rbp knockdown results in altered gene expression that both encompasses and is more severe than knockdown of unc-13. **A**) Venn diagram of differentially expressed genes (FDR = 0.05) by knockdown condition. **B-B'**) Volcano plots of *OK6>Rbp*^{RNAi} (**B**) and *OK6>unc-13*^{RNAi} (**B'**) highlighting genes encoding neuropeptides and secreted proteins. **C-C'**) Volcano plots of *OK6>Rbp*^{RNAi} (**C**) and *OK6>unc-13*^{RNAi} (**C'**) highlighting genes encoding exosome markers. Dotted lines in figures **B-B'**) and **C-C'**) demarcate a $\log_2$-fold-change of zero. The light gray single-dashed line demarcates an adjusted *p*-value of 0.05, while the dark gray double-dashed lines demarcate a fold-change of 0.5. Data points highlighted in red have an adjusted *p*-value < 0.05, while points highlighted in blue have a *p*-value ≥ 0.05.

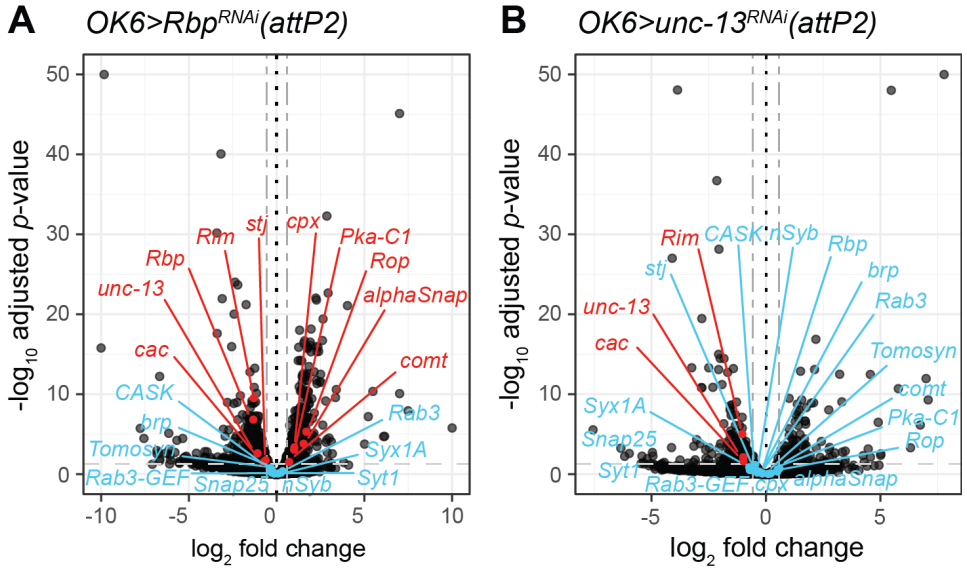

Figure 2.4) Knockdown of RSSPs decreases the expression of other structural AZ components. **A-B**) Volcano plot of *OK6>Rbp^{RNAi}(attP2)* (**A**) and *OK6>unc-13^{RNAi}(attP2)* (**A'**) highlighting genes comprising core synaptic machinery. Dotted lines demarcate a $\log_2$-fold-change of zero. The light gray single-dashed line demarcates an adjusted *p*-value of 0.05, while the dark gray double-dashed lines demarcate a fold-change of 0.5. Data points highlighted in red have an adjusted *p*-value < 0.05, while points highlighted in blue have a *p*-value ≥ 0.05.

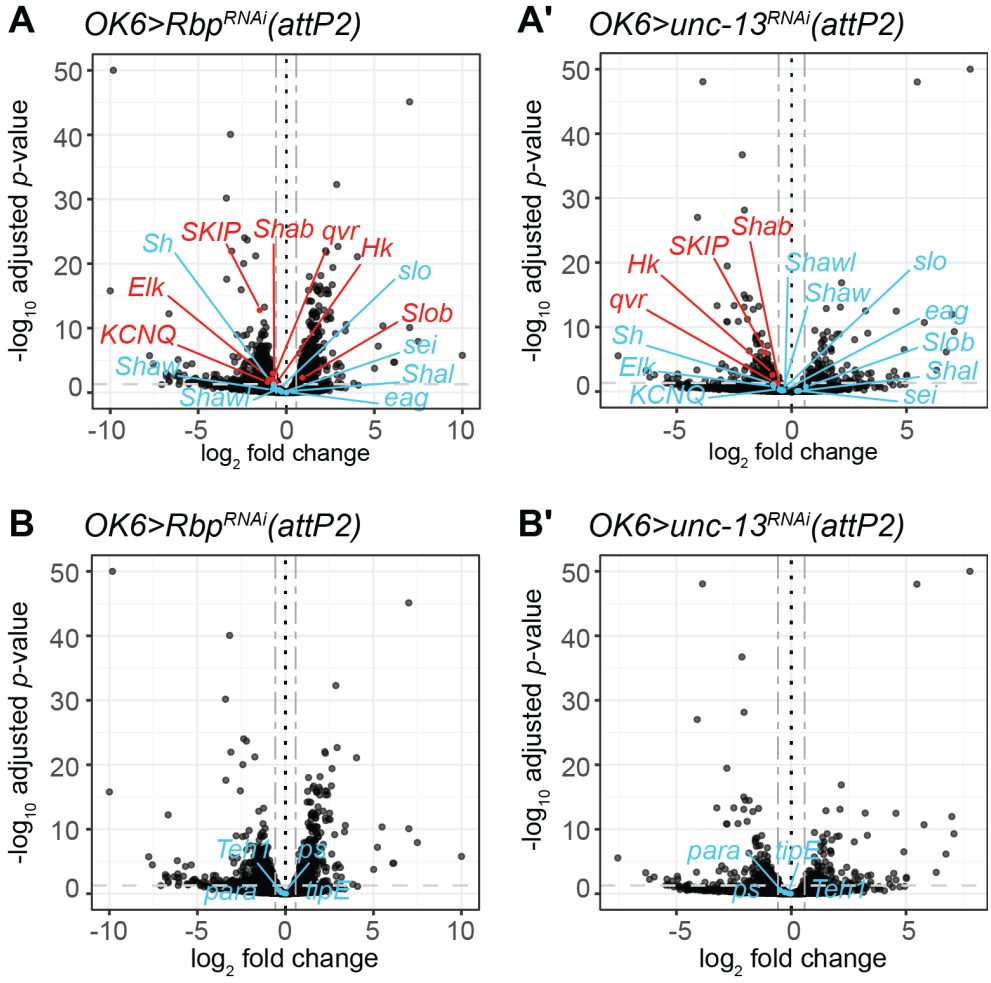

Figure 2.5) Loss of RSSPs results in down-regulation of voltage-gated K+ channel expression with no alteration in voltage-gated Na+ channel expression. **A-A'**) Volcano plots of *OK6>Rbp*^{RNAi} (**A**) and *OK6>unc-13*^{RNAi} (**A'**) highlighting (in red) genes encoding voltage-gated K+ channels and associated proteins. **B-B'**) Volcano plots of *OK6>Rbp*^{RNAi} (**A**) and *OK6>unc-13*^{RNAi} (**A'**) highlighting (in red) genes encoding voltage-gated Na+ channels and associated proteins.

Supplementary Table 2.1 Sample information for low-input RNA-seq of control and RNAi type I MNs

Run	Genotype	Biological replicates	Number of cells	Technical replicate
1	*OK6>empty(attP2)*	*n* = 12	6,414	OK6_ATTP2_001
1				OK6_ATTP2_002
1				OK6_ATTP2_003
1	*OK6>unc-13^{RNAi}(attP2)*	*n* = 19	1,753	OK6_UNC13_001
1				OK6_UNC13_002
1				OK6_UNC13_003
2	*OK6>empty(attP2)*	*n* = 10	3,530	OK6_ATTP2_101
2				OK6_ATTP2_102
2				OK6_ATTP2_103
2	*OK6>Rbp^{RNAi}(attP2)*	*n* =11	3,512	OK6_RBP_101
2				OK6_RBP_102
2				OK6_RBP_103

Supplementary Table 2.2 Top 15 differentially expressed genes in *OK6>Rbp*^{RNAi} Type I MNs

Up-regulated genes				
FlyBase ID	Gene symbol	log-fold-change	*p*-value	Adjusted *p*-value
FBgn0011581	Ms	7.01	1.95E-49	7.76E-46
FBgn0001258	Ldh	2.86	2.58E-36	5.13E-33
FBgn0032895	twit	2.94	2.20E-26	2.19E-23
FBgn0024995	CG2680	2.24	1.08E-25	9.53E-23
FBgn0266417	ringer	2.27	2.27E-25	1.64E-22
FBgn0027109	NPF	4.04	1.35E-24	8.24E-22
FBgn0019982	Gs1l	2.65	7.37E-23	3.91E-20
FBgn0003076	Pgm1	1.97	1.42E-21	9.83E-19
FBgn0000579	Eno	1.31	2.10E-21	9.83E-19
FBgn0033127	Tsp42Ef	2.61	4.52E-20	1.89E-17
FBgn0031037	CG14207	1.60	5.20E-20	2.07E-17
FBgn0028916	CG33090	1.92	8.06E-20	3.05E-17
FBgn0020235	ATPsyngamma	1.55	1.16E-19	4.19E-17
FBgn0033132	Tsp42Ej	1.93	2.20E-19	7.61E-17
FBgn0044046	Ilp7	2.27	3.29E-19	1.10E-16
Down-regulated genes				
FlyBase ID	Gene symbol	log-fold-change	*p*-value	Adjusted *p*-value
FBgn0019661	lncRNA:roX1	-9.83	1.03E-102	8.23E-99
FBgn0010113	hdc	-3.17	3.30E-44	8.75E-41
FBgn0004595	pros	-3.40	4.23E-34	6.74E-31
FBgn0016076	vri	-2.37	7.21E-28	9.56E-25
FBgn0010300	brat	-2.21	1.86E-27	2.11E-24
FBgn0038826	Syp	-3.10	1.41E-25	1.12E-22

FBgn0035692	Sf3b6	-1.74	9.34E-25	6.19E-22
FBgn0000546	EcR	-2.42	1.67E-23	9.51E-21
FBgn0267033	CG5151	-3.38	5.78E-21	2.55E-18
FBgn0036576	mamo	-2.56	3.51E-19	1.12E-16
FBgn0019660	lncRNA:roX2	-10.78	6.19E-19	1.64E-16
FBgn0032297	CG17124	-1.24	2.73E-16	5.57E-14
FBgn0051163	SKIP	-1.52	8.43E-16	1.64E-13
FBgn0063127	lncRNA:CR33938	-6.66	3.53E-15	5.97E-13
FBgn0043884	mask	-1.27	1.04E-13	1.40E-11

Supplementary Table 2.3 Top 15 differentially expressed genes in *OK6>unc-13*^{RNAi} Type I MNs

Up-regulated genes				
FlyBase ID	Gene symbol	log-fold-change	*p*-value	Adjusted *p*-value
FBgn0027109	NPF	7.78	1.26E-81	1.00E-77
FBgn0033268	Obp44a	5.47	3.66E-53	9.72E-49
FBgn00264810	Ldh	2.18	1.37E-20	1.36E-17
FBgn0039679	Pburs	2.12	1.57E-16	8.18E-14
FBgn0003071	AstC	1.51	2.85E-16	1.34E-13
FBgn0032895	Obp99a	3.22	7.57E-16	3.17E-13
FBgn0001145	Gs2	4.56	8.56E-16	3.40E-13
FBgn0000045	Act79B	6.99	2.91E-15	1.10E-12
FBgn0039332	alrm	5.78	6.61E-14	2.02E-11
FBgn0000579	Eno	1.01	1.11E-12	3.27E-10
FBgn0053527	SIFa	7.09	1.89E-12	5.18E-10
FBgn0024995	CG2680	1.56	1.86E-12	5.18E-10
FBgn0085417	natalisin	3.32	3.43E-12	9.10E-10
FBgn0023537	CG17896	2.08	4.65E-12	1.16E-09
FBgn0062978	CG31808	1.97	5.48E-12	1.32E-09
Down-regulated genes				
FlyBase ID	Gene symbol	log-fold-change	*p*-value	Adjusted *p*-value
FBgn0016076	vri	-3.87	2.19E-52	8.71E-49
FBgn0032297	CG17124	-2.15	9.62E-41	1.91E-37
FBgn0035692	Sf3b6	-2.06	4.59E-32	7.30E-29
FBgn0005612	Sox14	-4.10	7.31E-31	9.69E-28
FBgn0001234	lncRNA:Hsromega	-2.80	3.04E-23	3.45E-20
FBgn0010113	hdc	-2.07	1.16E-18	1.03E-15

FBgn0036935	CG14186	-2.00	4.17E-18	3.32E-15
FBgn0010300	brat	-1.84	4.86E-18	3.52E-15
FBgn0036576	CG5151	-2.50	7.63E-17	4.91E-14
FBgn0267033	mamo	-3.25	8.02E-17	4.91E-14
FBgn0051221	CG31221	-1.43	1.08E-16	6.16E-14
FBgn0003499	sr	-2.07	1.65E-16	8.18E-14
FBgn0003638	su(w[a])	-1.67	4.16E-16	1.85E-13
FBgn0000546	EcR	-1.92	1.72E-14	6.21E-12
FBgn0028407	Drep3	-2.32	3.99E-14	1.38E-11

References

Aberle, H., Haghighi, A.P., Fetter, R.D., McCabe, B.D., Magalhães, T.R., and Goodman, C.S. (2002). wishful thinking encodes a BMP type II receptor that regulates synaptic growth in Drosophila. Neuron *33*, 545–558.

Andrews, S. (2010). FastQC: a quality control tool for high throughput sequence data.

Aravamudan, B., Fergestad, T., Davis, W.S., Rodesch, C.K., and Broadie, K. (1999). Drosophila UNC-13 is essential for synaptic transmission. Nat. Neurosci. *2*, 965–971.

Augustin, I., Rosenmund, C., Südhof, T.C., and Brose, N. (1999). Munc13-1 is essential for fusion competence of glutamatergic synaptic vesicles. Nature *400*, 457–461.

Betz, A., Thakur, P., Junge, H.J., Ashery, U., Rhee, J.S., Scheuss, V., Rosenmund, C., Rettig, J., and Brose, N. (2001). Functional interaction of the active zone proteins Munc13-1 and RIM1 in synaptic vesicle priming. Neuron *30*, 183–196.

Birks, R.I., Mackey, M.C., and Weldon, P.R. (1972). Organelle formation from pinocytotic elements in neuntes of cultured sympathetic ganglia. J. Neurocytol. *1*, 311–340.

Böhme, M.A., Beis, C., Reddy-Alla, S., Reynolds, E., Mampell, M.M., Grasskamp, A.T., Lützkendorf, J., Bergeron, D.D., Driller, J.H., Babikir, H., et al. (2016). Active zone scaffolds differentially accumulate Unc13 isoforms to tune Ca(2+) channel-vesicle coupling. Nat. Neurosci. *19*, 1311–1320.

Bolger, A.M., Lohse, M., and Usadel, B. (2014). Trimmomatic: a flexible trimmer for Illumina sequence data. Bioinformatics *30*, 2114–2120.

Brown, J.B., Boley, N., Eisman, R., May, G.E., Stoiber, M.H., Duff, M.O., Booth, B.W., Wen, J., Park, S., Suzuki, A.M., et al. (2014). Diversity and dynamics of the Drosophila transcriptome. Nature *512*, 393–399.

Budnik, V., Ruiz-Cañada, C., and Wendler, F. (2016). Extracellular vesicles round off communication in the nervous system. Nat. Rev. Neurosci. *17*, 160–172.

Caussinus, E., Colombelli, J., and Affolter, M. (2008). Tip-cell migration controls stalk-cell intercalation during Drosophila tracheal tube elongation. Curr. Biol. *18*, 1727–1734.

Cavalli, V., Kujala, P., Klumperman, J., and Goldstein, L.S.B. (2005). Sunday Driver links axonal transport to damage signaling. J. Cell Biol. *168*, 775–787.

Celniker, S.E., Dillon, L.A.L., Gerstein, M.B., Gunsalus, K.C., Henikoff, S., Karpen, G.H., Kellis, M., Lai, E.C., Lieb, J.D., MacAlpine, D.M., et al. (2009). Unlocking the secrets of the genome. Nature *459*, 927–930.

Clary, D.O., Griff, I.C., and Rothman, J.E. (1990). SNAPs, a family of NSF attachment proteins

involved in intracellular membrane fusion in animals and yeast. Cell *61*, 709–721.

Covarrubias, M., Wei, A.A., and Salkoff, L. (1991). Shaker, Shal, Shab, and Shaw express independent K+ current systems. Neuron *7*, 763–773.

Desdín-Micó, G., and Mittelbrunn, M. (2017). Role of exosomes in the protection of cellular homeostasis. Cell Adh. Migr. *11*, 127–134.

Dickman, D.K., Kurshan, P.T., and Schwarz, T.L. (2008). Mutations in a Drosophila alpha2delta voltage-gated calcium channel subunit reveal a crucial synaptic function. J. Neurosci. *28*, 31–38.

Dietzl, G., Chen, D., Schnorrer, F., Su, K.-C., Barinova, Y., Fellner, M., Gasser, B., Kinsey, K., Oppel, S., Scheiblauer, S., et al. (2007). A genome-wide transgenic RNAi library for conditional gene inactivation in Drosophila. Nature *448*, 151–156.

Günther, M.N., Nettesheim, G., and Shubeita, G.T. (2016). Quantifying and predicting Drosophila larvae crawling phenotypes. Sci. Rep. *6*, 27972.

Hahne, F., LeMeur, N., Brinkman, R.R., Ellis, B., Haaland, P., Sarkar, D., Spidlen, J., Strain, E., and Gentleman, R. (2009). flowCore: a Bioconductor package for high throughput flow cytometry. BMC Bioinformatics *10*, 106.

Harrison, S.D., Broadie, K., van de Goor, J., and Rubin, G.M. (1994). Mutations in the Drosophila Rop gene suggest a function in general secretion and synaptic transmission. Neuron *13*, 555–566.

Huber, W., Carey, V.J., Gentleman, R., Anders, S., Carlson, M., Carvalho, B.S., Bravo, H.C., Davis, S., Gatto, L., Girke, T., et al. (2015). Orchestrating high-throughput genomic analysis with Bioconductor. Nat. Methods *12*, 115–121.

Jia, X.-X., Gorczyca, M., and Budnik, V. (1993). Ultrastructure of neuromuscular junctions in Drosophilal: Comparison of wild type and mutants with increased excitability. J. Neurobiol. *24*, 1025–1044.

Jiang, X., Litkowski, P.E., Taylor, A.A., Lin, Y., Snider, B.J., and Moulder, K.L. (2010). A role for the ubiquitin-proteasome system in activity-dependent presynaptic silencing. J. Neurosci. *30*, 1798–1809.

Kadota, T., Mizote, M., and Kadota, K. (1994). Dynamics of presynaptic endosomes produced during transmitter release. J. Electron Microsc. *43*, 62–71.

Kim, D., Paggi, J.M., Park, C., Bennett, C., and Salzberg, S.L. (2019). Graph-based genome alignment and genotyping with HISAT2 and HISAT-genotype. Nat. Biotechnol. *37*, 907–915.

Krasnoperov, V.G., Bittner, M.A., Beavis, R., Kuang, Y., Salnikow, K.V., Chepurny, O.G., Little, A.R., Plotnikov, A.N., Wu, D., Holz, R.W., et al. (1997). alpha-Latrotoxin stimulates

exocytosis by the interaction with a neuronal G-protein-coupled receptor. Neuron *18*, 925–937.

Liao, Y., Smyth, G.K., and Shi, W. (2014). featureCounts: an efficient general purpose program for assigning sequence reads to genomic features. Bioinformatics *30*, 923–930.

Liu, K.S.Y., Siebert, M., Mertel, S., Knoche, E., Wegener, S., Wichmann, C., Matkovic, T., Muhammad, K., Depner, H., Mettke, C., et al. (2011). RIM-binding protein, a central part of the active zone, is essential for neurotransmitter release. Science *334*, 1565–1569.

Lombaert, H., Grady, L., Pennec, X., Ayache, N., and Cheriet, F. (2014). Spectral Log-Demons: Diffeomorphic Image Registration with Very Large Deformations. Int. J. Comput. Vis. *107*, 254–271.

Love, M.I., Huber, W., and Anders, S. (2014). Moderated estimation of fold change and dispersion for RNA-seq data with DESeq2. Genome Biol. *15*, 550.

Ly, C.V., Yao, C.-K., Verstreken, P., Ohyama, T., and Bellen, H.J. (2008). straightjacket is required for the synaptic stabilization of cacophony, a voltage-gated calcium channel alpha1 subunit. J. Cell Biol. *181*, 157–170.

Ma, C., Su, L., Seven, A.B., Xu, Y., and Rizo, J. (2013). Reconstitution of the vital functions of Munc18 and Munc13 in neurotransmitter release. Science *339*, 421–425.

Moulder, K.L., Cormier, R.J., Shute, A.A., Zorumski, C.F., and Mennerick, S. (2003). Homeostatic effects of depolarization on Ca2+ influx, synaptic signaling, and survival. J. Neurosci. *23*, 1825–1831.

Moulder, K.L., Meeks, J.P., Shute, A.A., Hamilton, C.K., de Erausquin, G., and Mennerick, S. (2004). Plastic elimination of functional glutamate release sites by depolarization. Neuron *42*, 423–435.

Moulder, K.L., Jiang, X., Taylor, A.A., Olney, J.W., and Mennerick, S. (2006). Physiological activity depresses synaptic function through an effect on vesicle priming. J. Neurosci. *26*, 6618–6626.

Newman, Z.L., Hoagland, A., Aghi, K., Worden, K., Levy, S.L., Son, J.H., Lee, L.P., and Isacoff, E.Y. (2017). Input-Specific Plasticity and Homeostasis at the Drosophila Larval Neuromuscular Junction. Neuron *93*, 1388–1404.e10.

Pan, B., and Zucker, R.S. (2009). A general model of synaptic transmission and short-term plasticity. Neuron *62*, 539–554.

Peng, I.-F., and Wu, C.-F. (2007). Differential contributions of Shaker and Shab K+ currents to neuronal firing patterns in Drosophila. J. Neurophysiol. *97*, 780–794.

Reddy-Alla, S., Böhme, M.A., Reynolds, E., Beis, C., Grasskamp, A.T., Mampell, M.M., Maglione, M., Jusyte, M., Rey, U., Babikir, H., et al. (2017). Stable Positioning of Unc13

Restricts Synaptic Vesicle Fusion to Defined Release Sites to Promote Synchronous Neurotransmission. Neuron *95*, 1350–1364.e12.

Richmond, J.E., and Broadie, K.S. (2002). The synaptic vesicle cycle: exocytosis and endocytosis in Drosophila and C. elegans. Curr. Opin. Neurobiol. *12*, 499–507.

Risso, D., Ngai, J., Speed, T.P., and Dudoit, S. (2014). Normalization of RNA-seq data using factor analysis of control genes or samples. Nat. Biotechnol. *32*, 896–902.

Sanyal, S. (2009). Genomic mapping and expression patterns of C380, OK6 and D42 enhancer trap lines in the larval nervous system of Drosophila. Gene Expr. Patterns *9*, 371–380.

Söllner, T., Bennett, M.K., Whiteheart, S.W., Scheller, R.H., and Rothman, J.E. (1993). A protein assembly-disassembly pathway in vitro that may correspond to sequential steps of synaptic vesicle docking, activation, and fusion. Cell *75*, 409–418.

Stewart, B.A., Atwood, H.L., Renger, J.J., Wang, J., and Wu, C.F. (1994). Improved stability of Drosophila larval neuromuscular preparations in haemolymph-like physiological solutions. J. Comp. Physiol. A *175*, 179–191.

Südhof, T.C. (2012). The presynaptic active zone. Neuron *75*, 11–25.

Tang, A.-H., Chen, H., Li, T.P., Metzbower, S.R., MacGillavry, H.D., and Blanpied, T.A. (2016). A trans-synaptic nanocolumn aligns neurotransmitter release to receptors. Nature *536*, 210–214.

Tang, J., Maximov, A., Shin, O.-H., Dai, H., Rizo, J., and Südhof, T.C. (2006). A complexin/synaptotagmin 1 switch controls fast synaptic vesicle exocytosis. Cell *126*, 1175–1187.

Tolar, L.A., and Pallanck, L. (1998). NSF function in neurotransmitter release involves rearrangement of the SNARE complex downstream of synaptic vesicle docking. J. Neurosci. *18*, 10250–10256.

Turrigiano, G. (2012). Homeostatic synaptic plasticity: local and global mechanisms for stabilizing neuronal function. Cold Spring Harb. Perspect. Biol. *4*, a005736.

Van, P., Jiang, W., Gottardo, R., and Finak, G. (2018). ggCyto: next generation open-source visualization software for cytometry. Bioinformatics *34*, 3951–3953.

Wickham, H. (2010). ggplot2: Elegant Graphics for Data Analysis (Use R!) (Springer).

Chapter 3:
Altering the transcriptomic landscape by disruption of *Msp300*, a new model for presynaptic homeostatic potentiation

This chapter contains co-authored material, representing a collaborative effort between myself, Zachary L. Newman, and Shivali Baveja. I contributed to the experimental design and execution of RNA-sequencing experiments, including VNC dissections, FACS, RNA-seq library preparation and quality control, and data analysis, in addition to immunofluorescence staining and confocal microscopy. Z.L.N. performed the SynapGCaMP recordings in the semi-intact larval preparation and optical quantal analysis. S.B. performed the fillet dissections for immunofluorescence experiments

Abstract

Compensatory increases in action potential-evoked neurotransmission as a consequence of impaired postsynaptic response is a hallmark of presynaptic homeostatic plasticity (PHP). PHP at the *Drosophila* larval NMJ is mediated by a retrograde signal sent from the muscle to the presynaptic motor neuron terminal. How this retrograde signal differentially affects the synaptic machinery of AP-evoked neurotransmission versus spontaneous neurotransmission remains unknown. Here we identify a new genetic model of input-specific PHP in a commonly used *Drosophila* stock bearing a disruption of the *Msp300* gene. Transcriptomic characterization of this new model of PHP by RNA-sequencing suggests a role for cell adhesion molecules in mediating this retrograde signal and altering the physiology of individual release sites.

Background

Execution of homeostatic programs is a key survival mechanism for many biological systems in response to environmental challenges. Specialized homeostatic programs in neurons serve to stabilize the input and output of neural activity (Pozo and Goda, 2010). One potent form of such plasticity augments the release of neurotransmitter from the presynapse to compensate for reduced sensitivity at the postsynapse, a process known as presynaptic homeostatic potentiation (PHP).

PHP is a mechanism that is conserved across many organisms, but has been best characterized at the larval *Drosophila* neuromuscular junction (NMJ) (Davis and Müller, 2015). Excitatory drive at the *Drosophila* NMJ is provided by glutamatergic synapses formed by two morphologically and functionally distinct classes of motor neuron (MN) named type Ib and Is MNs. Compromised neurotransmission at the postsynaptic end of the NMJ, either by acute pharmacological blockade or genetic loss of postsynaptic glutamate receptors (GluRs), elicits a retrograde signal from the muscle to enhance synaptic vesicle (SV) exocytosis from the MN (Davis and Goodman, 1998; Davis et al., 1998; Frank et al., 2006; Petersen et al., 1997).

PHP is phenomenologically defined by an increase in the probability of release (P_r) of a SV per action potential (AP) fired by the MN, leading to an increase in the number SVs released overall (quantal content) (Davis and Müller, 2015). However, PHP also features a decrease in the glutamate content of each SV as measured by amplitude of spontaneous neurotransmission events (Frank et al., 2006; Petersen et al., 1997). The net result of these processes is overall stabilization of excitatory postsynaptic potentials in the muscle.

The molecular components of the retrograde signal and how they alter AP-evoked SV release is a topic of great interest. SV exocytosis occurs at specialized domains in the terminal boutons of MNs known as active zones (AZs) (Kittel and Heckmann, 2016; Südhof, 2012). Active zones are responsible for the correct positioning of SVs so that they can be rapidly released upon AP-evoked Ca^{2+} entry via voltage-gated Ca^{2+} channels (VGCCs). Hypomorphic mutations to the VGCC gene, *cacophony*, in *Drosophila* has shown that Ca^{2+} flux through VGCCs is necessary for the expression of PHP (Frank et al., 2006, 2009). While all the components of AZs are shared between type Ib and Is MNs, spatially-resolved measures of synaptic activity in the chronic

GluRIIA$^{-/-}$ model of PHP have shown that PHP is enacted specifically at type Ib synapses (Newman et al., 2017).

This is further complicated by the fact that PHP has divergent effects on different modes of neurotransmission. While both acute and chronic PHP robustly boost AP-evoked release, they also decrease the rate of spontaneous neurotransmission (Newman et al., 2017; Peled et al., 2014; Petersen et al., 1997). AP-evoked and spontaneous SV release occur at distinct sites within the presynaptic bouton (Peled et al., 2014). This raises the question of how and why PHP is exerted not only at specific terminals, but at specific SV release sites within those terminals.

In this study, we found that a commonly-used line for the integration of transgenic tools in *Drosophila* undergoes input-specific PHP. Seeking to understand genetic mechanisms for the expression of chronic PHP in these mutants, we performed RNA-sequencing on purified type I MNs and identified differential expression in groups of genes involved in anterograde signaling to the muscle, neuronal excitability, and cell adhesion. Using these results we generate a hypothesis involving alterations in cell adhesion that lead to increased AP-evoked SV exocytosis in PHP.

Results

attP40 mutants exhibit input-specific presynaptic homeostatic potentiation

While investigating the molecular mechanisms of PHP, we discovered that a commonly used *Drosophila melanogaster* stock bearing *attP40*, a site for phiC31-mediated integration of transgenes (Dietzl et al., 2007; Pfeiffer et al., 2008, 2010), has aberrant synaptic activity at the 3rd instar larval NMJ. The *attP40* site is located at 25C7 on the 2nd chromosome (Markstein et al., 2008), in an intronic region of the *Msp300* (Muscle-specific protein 300 kDa) gene (Figure 3.1A). *Msp300* encodes a Nesprin-like protein that is essential for embryonic muscle development, and controls the organization of nuclei in striated muscles by mediating the interaction between the cytoskeleton and the nuclear membrane (Elhanany-Tamir et al., 2012; Rosenberg-Hasson et al., 1996). *Msp300* has been shown to have more specific roles at the NMJ, including localization ribonuclear protein granules to the postsynapse as well as clustering of GluRIIA receptors (Apel et al., 2000; Morel et al., 2014; Packard et al., 2015). Mutations to *Msp300* result in decreased locomotion, diminished excitatory postsynaptic potential amplitude, and altered expression of GluRIIA (Elhanany-Tamir et al., 2012; Morel et al., 2014)

To characterize synaptic transmission in *attP40* mutants, we turned to optical quantal analysis for its superior spatial resolution over traditional electrophysiological methods (Peled and Isacoff, 2011). In the *Drosophila* 3rd instar fillet preparation, we use a postsynaptically-localized genetically-encoded Ca^{2+} sensor, SynapGCaMP (*MHC-CD8-GCaMP6f-Sh*), to report on synaptic transmission (Newman et al., 2017). The high signal-to-noise ratio of SynapGCaMP combined with fast, spinning-disk confocal microscopy allows us to discriminate neurotransmission events between different release sites within the same axon terminal or between different inputs.

We employed this technique in the semi-dissected larval fillet preparation, in which we removed the brain and electrically stimulated the nerve bundles projecting to the body wall muscles. We tested the effect of the insertion of the pCaryP vector at *attP40* by comparing the synaptic function of these animals to the *attP2* line, which harbors the vector in an intergenic region on the 3rd chromosome. We measured AP-evoked release subjecting type Ib and Is MNs to low-frequency stimulation (0.1 Hz) and optically-recording the SynapGCaMP response at muscle 4. We found that Is release sites have higher P_r compared Ib in animals bearing either *attP2* or *attP40* insertion (Figure 3.1B), as described previously in wild-type larvae (Newman et al., 2017). Similarly, the mean quantal density (QD, area-normalized quantal content) per stimulus of Is synapses is greater than that of Ib synapses (Figure 3.1C). However, we discovered that *attP40* mutant Ib synapses have a 1.47-fold increase in P_r and a 1.60-fold increase in quantal density relative to *attP2* Ib synapses (Figure 3.1B-C). We did not observe this trend in Is synapses across any of the genotypes we tested (Figure 3.1B-C). These data suggest that the mutation introduced by the *attP40* insertion phenocopies the input-specific plasticity that we have previously observed in the *GluRIIA*$^{-/-}$ model of PHP.

Since *attP40* synapses functionally resemble *GluRIIA*$^{-/-}$ synapses and mutations to *Msp300* alter GluRIIA density, we next asked if *attP40* mutants also have perturbed GluRIIA expression. We stained for GluRIIA in wild-type (*OK6-Gal4;SynapGCaMP*), *attP2* (*OK6-Gal4>,empty(attP2)*; *SynapGCaMP*), *attP40* (*OK6-Gal4>empty(attP40)*; *SynapGCaMP*), and *GluRIIA*$^{-/-}$ (*GluRIIA*^{SP16}*/Df(cl)h4;SynapGCaMP*) NMJs. We found that GluRIIA was expressed in the postsynaptic densities of wild-type, *attP2*, and *attP40* Ib NMJs, but was completely absent in the *GluRIIA*$^{-/-}$ postsynapse (Figure 3.1D-G). Defects in nuclear positioning found in *Msp300* KASH domain mutants (Elhanany-Tamir et al., 2012) were not observed in the body wall muscles of wild-type controls, *attP2*, *attP40*, or *GluRIIA*$^{-/-}$ larvae (Supplementary Figure 3.1). Collectively, this evidence suggests that chronic PHP in *attP40* mutants is induced downstream of GluRIIA disruption. However, it remains to be seen if the balance of GluRIIA expression is altered *attP40* mutants with respect to other GluRs in the muscle.

<u>*attP40* type I MNs have altered expression of genes involved neuropeptide signaling, exosome expression, and excitability</u>

Intrigued by the functional similarities between *attP40* and *GluRIIA*$^{-/-}$ models of PHP, we wanted to understand the mechanisms underlying this form of plasticity. To generate specific hypotheses for how this process works, we leveraged the exploratory power of RNA-sequencing to identify differentially expressed genes between *attP40* mutants and *attP2* controls.

Purified populations of neuroblasts by fluorescence activated cell sorting (FACS) from *Drosophila* larvae have been used for transcriptional profiling (Berger et al., 2012), so we adapted this approach for purifying type I MNs (Figure 3.2A). We accomplished this by utilizing the *OK6-Gal4* line to drive expression of nuclear mCherry in type I MNs (Aberle et al., 2002; Caussinus et al., 2008; Sanyal, 2009). Previous anatomical and developmental studies have shown that Ib MNs constitute the majority of type I MNs (Hoang and Chiba, 2001), and therefore differences in gene expression should largely reflect alterations in the transcriptional profiles of type Ib MNs. We prepared sequencing libraries from a purified population type I MNs

by first screening 3rd instar larvae for mCherry expression, dissecting the brain and ventral nerve cords (VNCs) of screened larvae, dissociating the cells for FACS, and preparing Illumina sequencing libraries from RNA isolated from sorted cells (Figure 3.2A; see Methods and Table 3.1 for details).

We performed exploratory principal component analysis (PCA) on normalized transcriptomes of type I MNs from *OK6>empty(attP40)* (*w^{1118};OK6-Gal4/(attP40);UAS-mCherry-NLS/+*) and *OK6>empty(attP2)* (*UAS-Dcr2;OK6-Gal4/+;UAS-mCherry-NLS/(attP2)*) animals. We found that libraries from *OK6>empty(attP40)* MNs are separated from *OK6>empty(attP2)* libraries in PCA space, indicating that MNs from each genotype are transcriptionally distinct (Figure 3.2B). Next, we evaluated the success of our normalization and differential expression (DE) inference pipelines (see Methods and Appendix 1 for details) by examining the expression of *UAS* transgenes as a ground truth for DE inference, with *UAS-mCherry-NLS* serving as a negative control and *UAS-Dcr-2* serving as a positive control. We determined that *mCherry* expression is indistinguishable between *OK6>empty(attP40)* and *OK6>empty(attP2)* controls (Figure 3.2C). In accordance with our ground truths, *Dcr-2* has ~400-fold (8.73 $\log_2$ fold-change) greater expression in *OK6>empty(attP2)* samples (Figure 3.2D). Optical recording of *SynapGCaMP* larvae with both the *attP2* insertion and *UAS-Dcr-2* transgene show that overexpression of Dcr-2 has no impact on either P_r or quantal density (Supplementary Figure 3.2).

We next asked if *OK6>empty(attP40)* MNs have altered expression of *Msp300* relative to *OK6>empty(attP2)* controls. Indeed, we found that a single copy of the *attP40* insertion results in a 2.7-fold (-1.43 $\log_2$ fold-change) reduction in *Msp300* mRNA expression (Figure 3.2E). Having confirmed that *attP40* decreases *Msp300* expression, we next asked which genes are differentially expressed as a consequence. We found that, much like knockdown of release site stabilizing proteins (see Chapter 2), *OK6>empty(attP40)* samples had increased expression of neuropeptides and tetraspanins (Figure 3.3A-B, Supplementary Table 3.2) and decreased expression of voltage-gated K+ channels (Figure 3.3C). These results suggest that alterations in anterograde signaling, trafficking and excitability are general responses to synaptic dysfunction.

<u>*attP40* type I MNs have decreased expression Dystrophin Glycoprotein Complex genes</u>

Since we seek potential mechanisms to explain PHP in the *attP40* model, we examined DE genes that are unique to this condition. Among the up-regulated genes was *shriveled* (*shv*) (Supplementary Table 3.2), a protein secreted from motor neuron terminals during high-levels of activity (Lee et al., 2017). This is likely an anterograde response to *attP40* loss of function, as secretion of *shv* boosts GluR expression via it's interactions with muscle β-integrin (Lee et al., 2017). We also noticed among the top 15 down-regulated genes that there are several genes encoding cell-adhesion molecules (CAMs) or extracellular-matrix (ECM) interacting proteins (*eys*, *Dscam1*, and *side-III;* Supplementary Table 3.2). CAMs have well established roles in axon guidance and synapse maturation in *Drosophila* (Ashley et al., 2019; Chiba et al., 1995; Schmucker et al., 2000; Siebert et al., 2009; Thomas et al., 1997), as well as established roles in long-term potentiation at synapses in the hippocampus (Aoto et al., 2013; Armstrong et al., 2006; Bozdagi et al., 2000; Contractor et al., 2002). The *Drosophila* genome encodes roughly 1000 cell

surface molecules and secreted proteins involved in synaptic target recognition (Kurusu et al., 2008), and the function of many of these genes remain poorly characterized at the NMJ.

We noticed that several components of the Dystrophin Glycoprotein Complex (DGC) had decreased expression in *OK6>empty(attP40)* libraries compared to controls (Figure 3.4A-B). Mutations in the human orthologs of DGC genes result in muscular dystrophies (Grady et al., 1999; Hoffman and Kunkel, 1989). The DGC interacts extracellularly with laminin A, a known activity-dependent retrograde signal that is regulated by crawling activity (Tsai et al., 2012). Moreover, both *Dystrophin* (*Dys*) and *Dystrobrevin* (*Dyb*) mutants have elevated quantal content (Jantrapirom et al., 2019; van der Plas et al., 2006). The intracellular components of the DGC, *Dys*, *Dyb*, *Syntrophin-like 1* (*Syn1*), and *Syntrophin-like 2* (*Syn2*) are all down-regulated in *attP40* MNs (Figure 3.4A). The extracellularly facing components, *Dystroglycan* (*Dg*) and the Sarcogylcan family genes (*Scgα*, *Scgβ*, *Scgδ*) have either no change expression or mixed regulation (Figure 3.4B).

<u>*attP40* type I MNs have mixed regulation of genes encoding complexin PTM enzymes</u>

While immunohistological evidence suggests that the DGC complex is expressed primarily at the postsynapse, our findings suggest a presynaptic role. While some CAMs and ECM interacting proteins, such as *Plexin B* (*PlexB*) or *Multiplexin*, are required for PHP (Orr et al., 2017; Wang et al., 2014), it is unclear if these molecules act in an instructive or permissive role for PHP expression. We examined the expression of *PlexB* and its downstream effector *Mical* and found that they have decreased expression at the mRNA level in *attP40* mutants (Supplementary Figure 3.3). Wondering if loss of the DGC components instead could produce an increase in P_r or quantal content, we examined the expression of genes encoding proteins known to interact with the intracellular components of the DGC. We found that *OK6>empty(attP40)* had 2.5-fold less (-1.33 $\log_2$ fold-change) *Nos* (*<u>N</u>itric <u>o</u>xide <u>s</u>ynthase*) expression (Figure 3.4C).

Presynaptic nitric oxide (NO) has been shown to decrease evoked activity by enhancing the fusion-clamp function of complexin (cpx) by S-nitrosylation (Huntwork and Littleton, 2007; Robinson et al., 2018). S-nitrosylation is a reversible post-translational modification (PTM) of cpx, and competes for the same C-terminal CAAX motif as farnesylation, which shunts cpx to the endomembrane system (Iyer et al., 2013; Reim et al., 2005; Robinson et al., 2018). Suppression of farnesylation recapitulates the effects of NO, and reduces AP-evoked vesicular release (Robinson et al., 2018). We examined the expression of *cpx* and genes encoding enzymes that modify cpx function (Figure 3.4C). While *cpx* expression was unchanged, *farnesyltransferase B* (*CG17565*) had 2.8-fold greater (1.47 $\log_2$ fold-change) expression in the *attP40* mutants (Figure 3.4C). *Farnesyltransferase a* (*Fnta*) and PKA (*Pka-C1*), which phosphorylates cpx to enhance spontaneous release (Cho et al., 2015), had no difference in expression between the genotypes sequenced (Figure 3.4C).

With this evidence we put forth a potential mechanism for PHP as observed in *attP40* mutants. We propose that under normal signaling conditions, moderate expression of the DGC results in localization of Nos to the presynaptic volume, where the NO it produces can compete with farnesylases to modify cpx (Figure 3.5A). This results in appropriate clamping of AP-evoked

synaptic vesicle release. In *attP40* mutants, expression of the DGC is decreased, resulting in decreased expression of Nos (Figure 3.5B). Loss of *attP40* results in presynaptic homeostatic potentiation, which results in a concomitant decrease in the expression of the DGC and Nos. Simultaneous decrease in Nos expression and increase in farnesylase expression shunts cpx from the AZ to the endomembrane system, resulting in reduced clamping activity of cpx and apparent increase in evoked P_r and quantal content (Figure 3.5B).

Conclusions and Discussion

The role of Msp300 in postsynaptic physiology and retrograde signaling

With this evidence, we establish that mutations to *Msp300* by the *attP40* insertion alter synaptic function. We show that *attP40* mutants have increased P_r and QD specifically at Ib terminals (Figure 3.1B-C) at magnitudes similar to the classic *GluRIIA*$^{-/-}$ model of chronic PHP (Newman et al., 2017). This alteration in presynaptic behavior appears without gross anomalies in nuclear localization (Supplementary Figure 3.1) or GluRIIA expression (Figure 3.1D-G).

The need for Msp300 in normal postsynaptic physiology remains ambiguous. Msp300 mutants lacking the KASH domain have diminished locomotion, altered GluRIIA localization, and uneven distribution of nuclei in muscle segments (Morel et al., 2014). Msp300 organizes F-actin tracts between the nucleoskeleton and the postsynaptic density and is essential for synapse maturation (Packard et al., 2015). Recent work has shown that *Msp300* transcripts are bound in ribonuclear protein granules, and are trafficked to the postsynapse and locally translated in an activity dependent manner to stabilize nascent synapses (McDermott et al., 2014; Titlow et al., 2020). Since this process has been characterized in the context of synapse development, it remains to be seen how Msp300 functions in the homeostatic stabilization of mature boutons or if this process is input-specific.

Involvement of CAMs in presynaptic homeostatic plasticity

Functional understanding of the mechanisms of PHP has been plagued by the difficulty in discriminating between molecular components that instruct or simply mediate PHP. To generate specific hypotheses for the mechanism of PHP we sequenced the transcriptomes of purified type I MNs from *attP40* mutants. We found that the transcriptomes of purified MNs from *attP40* mutants are distinct from *attP2* controls and have sweeping alterations in the expression of neuropeptides, tetraspanins, and voltage-gated K+ channels. These gene expression changes are similar to those observed in a different model of presynaptic plasticity in which the expression of AZ components are reduced by RNA interference (see Chapter 2).

Seeking to identify potential causal mechanisms specific to PHP in *attP40* mutants, we noticed that the intracellular components of the DGC were down-regulated, along with other CAMs (Figure 3.4A, Supplementary Table 3.2). The function of CAMs at the *Drosophila* NMJ has largely been focused on synapse formation and maturation (Missler et al., 2012; Walsh and Doherty, 1997), but there is a growing body of literature on the participation of CAMs in neurotransmission by tuning AZ organization and composition (Banovic et al., 2010; Li et al.,

2007; Mosca et al., 2012). Long-term expression of PHP requires AZ remodeling (Böhme et al., 2019; Mrestani et al., 2019), a process that has become amenable to study as superresolution microscopy methods become increasingly accessible. With these methods AZ compaction and the formation of multi-ring AZ structures have been described as attendant phenomena in both acute and chronic PHP (Hong et al., 2020; Mrestani et al., 2019). These aberrant AZ structures also form in response to loss of function mutations in *neuroligin*, demonstrating that transsynaptic interactions between CAMs can influence both the structure and function of presynaptic neurotransmission machinery (Hong et al., 2020).

Alterations in CAMs pose interesting hypotheses about how the ECM may influence synaptic physiology. *In vivo* imaging of synaptic activity at NMJ of *Drosophila* larvae during restrained crawling has demonstrated that MNs are subjected to much mechanical warping during muscle contraction (Newman et al., 2017). Since many myopathies and muscular dystrophies observed in humans can be attributed to mutations in ECM genes (Ahmad et al., 2020), it's tempting to think that homeostatic plasticity can be enacted by direct mechanical sensing via CAMs and the basal lamina. Laminins, which make up the influence the organization of the vertebrate NMJ via direct interactions with VGCCs, dystroglycan, and integrins (Rogers and Nishimune, 2017).

Indeed the role of the ECM in the development of is better understood in *en passant* synapses with a basement membrane, like the vertebrate NMJ. Much less is known about the function of the ECM at the *Drosophila* larval NMJ as the boutons are largely engulfed by the muscle's subsynaptic reticulum (Atwood et al., 1993). Yet these synapses must still function despite the mechanical shearing from muscle contraction. Although the larval *Drosophila* NMJ lacks contact with a basement membrane, muscle-derived laminins and their interactions with the DGC and integrins have been shown to regulate synaptic function in this system (Beumer et al., 1999; Bogdanik et al., 2008; Tsai et al., 2008, 2012). In addition to laminins, heparan sulfate proteoglycans are also localized to the NMJ (Johnson et al., 2006; Kamimura et al., 2019; Ren et al., 2009). Mutant larvae with impaired heparan sulfate biosynthesis and expression have alterations in both evoked and spontaneous activity, as well as deficits in locomotion (Johnson et al., 2006; Ren et al., 2009). How CAMs and the ECM participate in synapse formation and homeostasis, or how these structures might be modified during these processes, remains an exciting avenue of investigation.

Untangling alterations in spontaneous and AP-evoked SV exocytosis in PHP

Using DE inference from our RNA-seq data, we propose a mechanism for the enhanced neurotransmission observed in *attP40* mutants. In our proposed mechanism, decreased expression of the DGC and Nos result in reduced S-nitrosylation of cpx. Reduced NO activity and enhanced farnesyltransferase expression lead cpx to be retained in the endomembrane system. This in turn produces a net decrease in clamping activity and the observed increase in P_r and quantal density observed in *attP40* mutants.

Electrophysiological characterization of *Nos* mutants has shown that decreased NO activity increases both AP-evoked activity and spontaneous activity (Robinson et al., 2018), while overexpression of Nos has the opposite effect. In contrast, PHP is characterized by severe

reductions in the frequency and amplitude of spontaneous activity (Petersen et al., 1997). Since spontaneous release and AP-evoked release are favored by distinct sets of synapses within the NMJ (Peled et al., 2014), the subcellular distribution of Nos and cpx may be key to explaining the suppression of spontaneous activity during PHP (Figure 5.4C). The early stages of AZ remodeling repurposes existing AZ scaffolding protein at the synapse to rapidly increase P_r and quantal content (Böhme et al., 2019). Redistributing cpx towards sites where SV release is unlikely to result in meaningful depolarization of the muscle would boost P_r at PHP-remodeled AZs, as Ca^{2+}-dependent SV exocytosis is extinguished by high local concentrations of cpx (Tang et al., 2006).

AZ remodeling might also explain differences in short-term plasticity in PHP models. *GluRIIA*$^{-/-}$ Ib synapses fail to facilitate after in response to an AP train due to a reduction in the number of silent sites recruited (Newman et al., 2017). The process of AZ remodeling during PHP may result in partially-assembled, non-functional sites that may be detected with *post hoc* immunohistochemistry or other imaging methods.

While the importance of AZ reorganization and regulation in presynaptic homeostatic programs is coming into view, we have leveraged RNA-sequencing to test thousands of hypotheses regarding the genetic regulation of chronic PHP and prioritize potential mechanisms for functional testing. Integration of structural information from microscopy experiments and physiological measurements of synaptic function will allow the molecular sequences of PHP to be uncovered.

Methods

Fly Stocks

Drosophila melanogaster stocks bearing transgenes to drive expression in type I MNs (OK6-Gal4; (Aberle et al., 2002; Sanyal, 2009) were bred and maintained in a *w*^{1118} background. Fruit fly stocks bearing a synaptically-localized GCaMP6f (*SynapGCaMP*) under the control of the myosin heavy-chain (*MHC*) promoter were used for reporting postsynaptic activity in the muscle (Newman et al., 2017) in electrophysiology and immunohistochemistry experiments. Fly stocks with the *GluRIIA*^{SP16} allele and Df(2L)clh4 deficiency (Petersen et al., 1997) were obtained from Corey Goodman (UC Berkeley). Fruit fly stocks bearing transgenes encoding nuclear mCherry (*UAS-mCherry-NLS*; Caussinus et al., 2008, BDSC #38424) in type I MNs were used for the purpose of FACS sorting.

Larvae were raised to the 3rd instar stage on cornmeal and molasses media in an incubator at 25°C. Female parents were crossed with male parents bearing either the *attP2* empty vector or *attP40* empty vector construct to obtain control and *attP40* mutant progeny, respectively.

Fruit fly 3rd instar larvae with the following genotypes were used for the experiments described in this chapter:

w^{1118}*;OK6-Gal4/+;MHC-GCaMP6f/+*

w^{1118};OK6-Gal4/+;MHC-GCaMP6f/(attP2)
w^{1118};OK6-Gal4/(attP40);MHC-GCaMP6f/+
w^{1118};$GluRIIA^{SP16}$/Df(2L)clh4;MHC-GCaMP6f/+
UAS-Dcr2;OK6-Gal4/+;MHC-GCaMP6f/(attP2)
w^{1118};OK6-Gal4/(attP40);MHC-GCaMP6f/+
w^{1118};OK6-Gal4/(attP40);UAS-mCherry-NLS/+
UAS-Dcr2;OK6-Gal4/+;UAS-mCherry-NLS/(attP2)

Immunohistochemistry and Confocal Microscopy

Fillet preparation of 3rd instar larvae in HL3 buffer was performed as described previously (Stewart et al., 1994), and fixed in Bouin's fixative for 15 minutes at room temperature and permeabilized in 1X PBS with 0.1% Triton X100 (PBT) for a minimum of 2 hours. Samples were blocked in 1X PBS with 0.1% Triton X100, 5% normal goat serum, and 0.02% sodium azide (PBN) for 30 minutes at room temperature on a nutator in a round-bottom 2 mL tube. Primary incubations were performed overnight at 4 °C. Samples were washed three times in PBT for 15 minutes at room temperature and then blocked for 30 minutes in PBN. Secondary incubations were performed for 2 hours at room temperature. Residual antibodies were removed with a final series of three 15 minute washes in PBT. Samples were mounted on glass slides in VectaShield antifade mounting medium (Vector Labs).

GluRIIA localization assays used the following primary antibodies: 1:1000 chicken anti-GFP (Invitrogen, Cat#A10262, RRID:AB_2534023), mouse anti-GluRIIA (Developmental Studies Hybridoma Bank, Cat#8B4D2, RRID:AB_528269), 1:250 Cy3-conjugated anti-HRP (Jackson Immunoresearch, Cat#123-165-021, RRID: AB_2338959). The following secondary antibodies were also used in the GluRIIA localization experiments: 1:1000 AF488-conjugated goat anti-chicken (Invitrogen, Cat#A11039, RRID: AB_2534096), AF647-conjugated goat anti-mouse (Invitrogen, Cat#A21235, RRID:AB_2535804). Nuclear position was assayed by staining samples with Hoechst. Confocal images to assess nuclear localization were acquired on a ZEISS LSM 710 microscope with a 40X oil-immersion objective. Confocal images of GluRIIA stains were acquired on a ZEISS LSM 810 microscope with a 63X oil-immersion objective. NMJs contacting muscle 4 in segments A2-A5 were used for imaging.

Image processing was performed with ImageJ. High-frequency noise was removed from the images with a Guassian blur with a 0.5 pixel radius. Background subtraction was performed after taking the maximum intensity projections of each stack. Representative pseudocolor images were set to the same contrast across all images for each channel.

SynapGCaMP Imaging and Optical Quantal Analysis

Fillet preparations and recording of evoked SynapGCaMP activity were performed as described in Chapter 2. Data analysis routines were performed as described in Chapter 2.

CNS Dissection, Dissociation, and FACS

Samples were dissected, dissociated, and sorted as described in Chapter 2.

Low Input RNA-Seq Cell Capture, Library Preparation, and Sequencing

Cell capture, library preparation, and sequencing were performed with the same procedure as described in Chapter 2.

RNA-Seq Alignment and Pre-processing

Read quality and trimming were performed as described in Chapter 2. Trimmed reads were aligned to a custom reference genome built from Berkeley Drosophila Genome Project (dm6, release 95) genome assembly and the pUAST-mCherry-NLS vector sequence for the detection of the encoded transgenes used in these experiments. Mapping, read quantification, filtering, normalization, and biological analysis were performed as described in Chapter 2.

Gene Filtering and Normalization

Biological analysis was performed in R after using a custom script to import the featureCounts output into a SummarizedExperiment object (ver 1.16.1, Huber et al., 2015). Genes were filtered and normalized as described in Chapter 2.

Differential Expression Testing and Visualization

Identification of differentially expressed (DE) genes between each knockdown condition was performed with the DESeq2 (ver 1.26.0, Love et al., 2014). Visualization of DE analysis was performed with custom scripts built upon ggplot2 (ver 3.2.1, Wickham, 2010).

Code availability

Code used for all RNA-sequencing data analysis steps will be available publicly in a Github repository at https://github.com/isacofflab/presynap_MN upon publication.

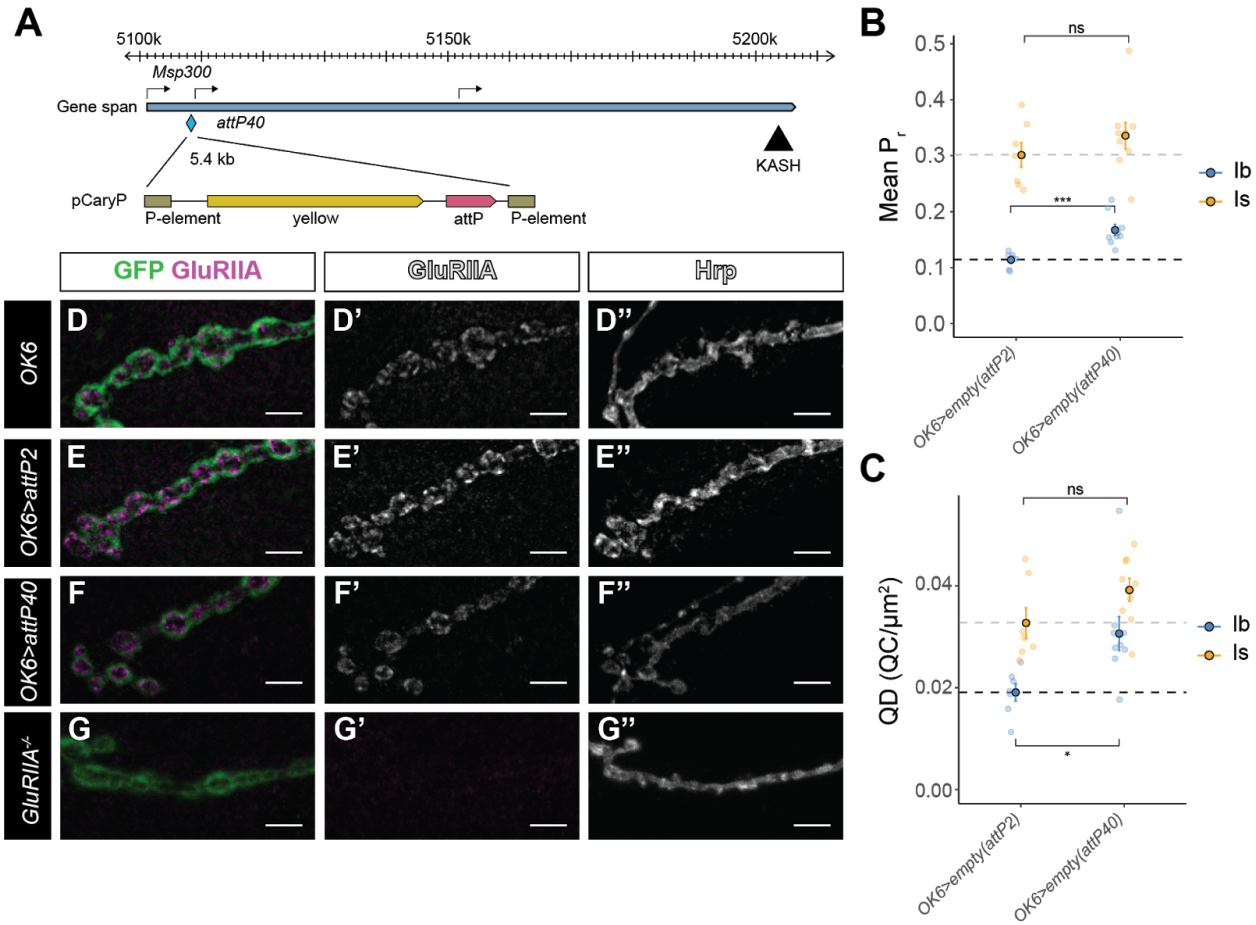

Figure 3.1) Mutation of *Msp300* by the *attP40* insertion results in input-specific PHP. **A)** Diagram of *attP40* insertion in the *Msp300* gene. Arrows indicate predicted transcription start sites for various isoforms of *Msp300*. Arrowhead indicates the location of the exon containing the KASH domain. **B**) Mean probability of vesicle release (P_r) per stimulus per NMJ by optical quantal analysis of Ib (blue) and Is (orange) terminals in *OK6>empty(attP2)* (*OK6>empty(attP2);SynapGCaMP*) and *OK6>empty(attP40)* (*OK6>empty(attP40);SynapGCaMP*). **C**) Quantal density (QD, area normalized quantal content) by optical quantal analysis. Genotypes and NMJ types are the same as in (**B**). (Solid circle, mean; Error bars, SEM; ANOVA and Dunnett's *post hoc* test *p*-values, ns $p > 0.05$, * $p < 0.01$, ** $p < 0.001$, *** $p < 0.0001$). **D-G)** Representative confocal images of muscle 4 type Ib MNs expression of SynapGCaMP (green), and GluRIIA (magenta), GluRIIA alone, and Hrp alone for *OK6* controls (*OK6;SynapGCaMP*, **D-D''**), *OK6>attP2* controls (*OK6>empty(attP2);SynapGCaMP*, **E-E''**), *OK6>attP40* mutants (*OK6>empty(attP40);SynapGCaMP*, **F-F''**), and *GluRIIA*$^{-/-}$ mutants (*GluRIIA*$^{-/-}$*;SynapGCaMP*, **G-G''**). Scale bar, 5 µm.

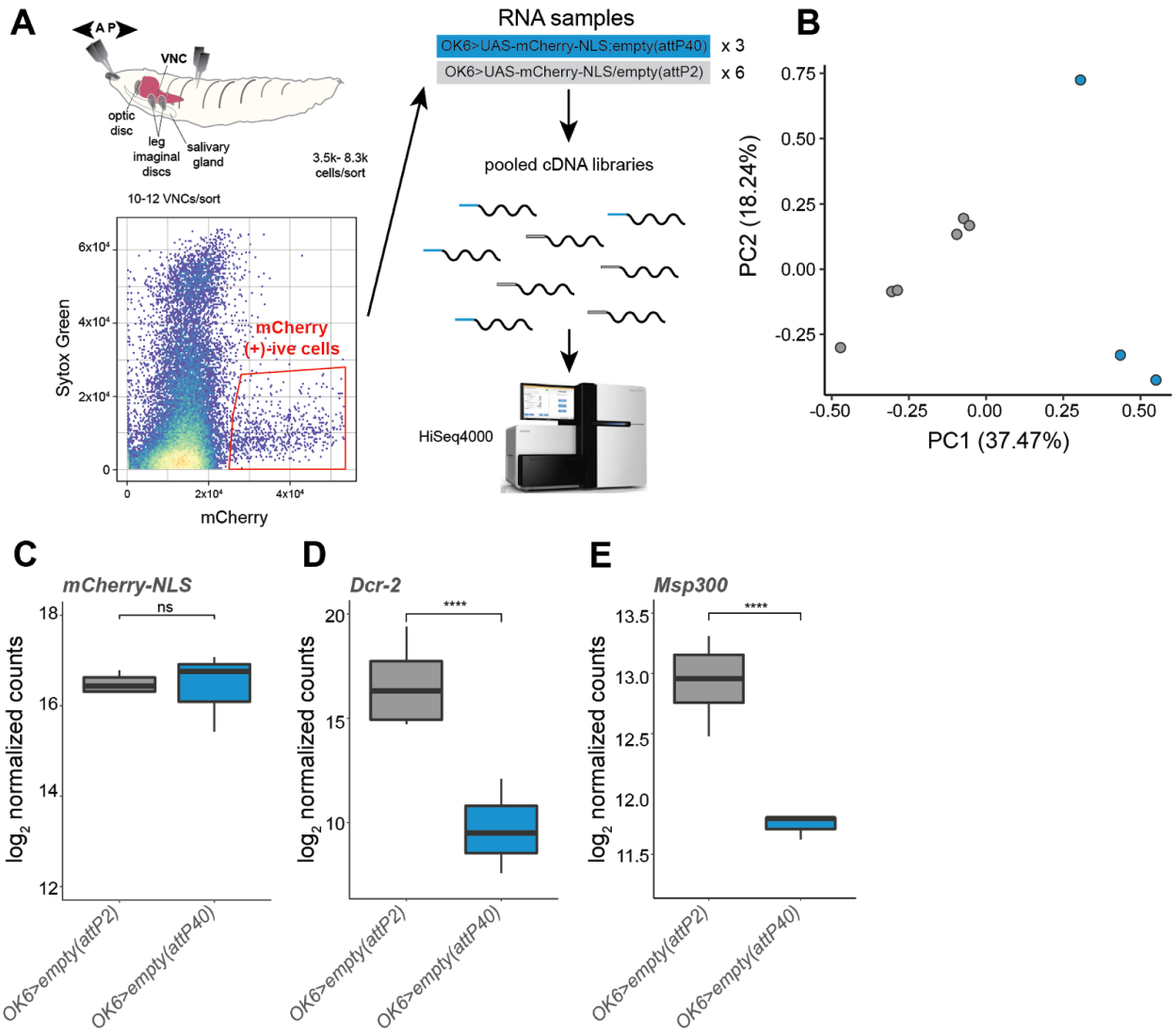

Figure 3.2) *attP40* mutant type I MNs are transcriptionally distinct from *attP2* controls. **A**) Schematic for generating RNA-seq libraries from sorted motor neuron populations from control (*OK6>empty(attP2)*) and *attP40* mutant (*OK6>empty(attP40)*) animals. **B**) Principal component analysis (PCA) plot of RNA-seq samples points colored as depicted in **A**. Axes are annotated by percent variance explained for each principal component. **C-E**) Boxplots of $\log_2$ normalized pseudocount expression of **C**) *mCherry-NLS*, **D**) *Dcr-2*, **E**) *Msp300* (BH-adjusted Wald test *p*-values, ns $p > 0.05$, * $p < 0.01$, ** $p < 0.001$, *** $p < 0.0001$, **** $p <$ 1e-05).

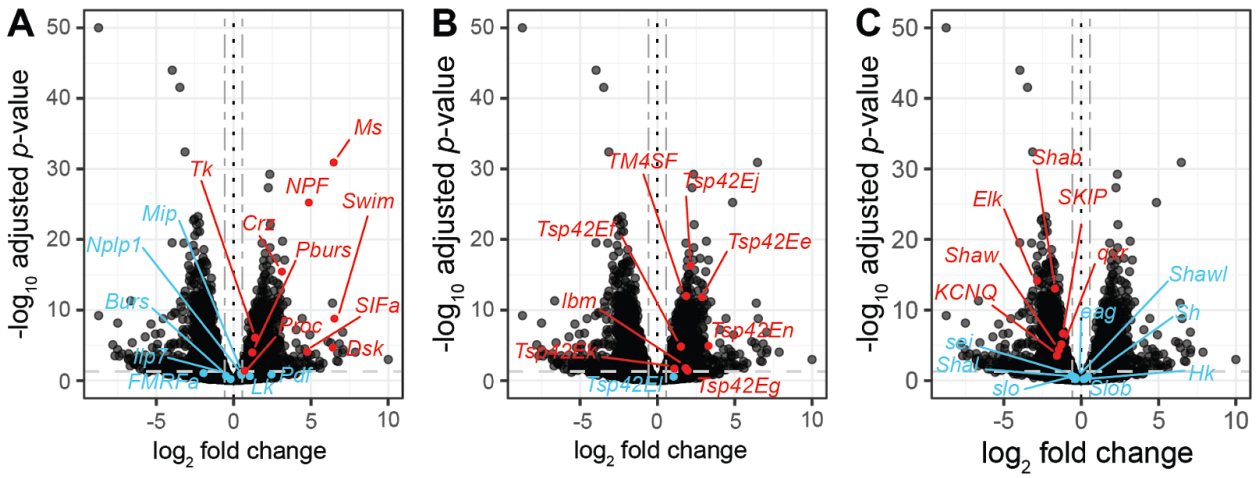

Figure 3.3) *attP40* mutants feature increased expression of exosome markers and neuropeptides, but a decrease in voltage-gated K+ channels. **A-C)** Volcano plots comparing *OK6>empty(attP40)* MNs to *OK6>empty(attP2)* controls highlighting genes encoding neuropeptides (**A**), tetraspanins (**B**), and voltage-gated K+ channels (**C**). Dotted lines demarcate a $\log_2$-fold-change of zero. The light gray single-dashed line demarcates an adjusted *p*-value of 0.05, while the dark gray double-dashed lines demarcate a fold-change of 0.5. Data points highlighted in red have an adjusted *p*-value < 0.05, while points highlighted in blue have a *p*-value ≥ 0.05.

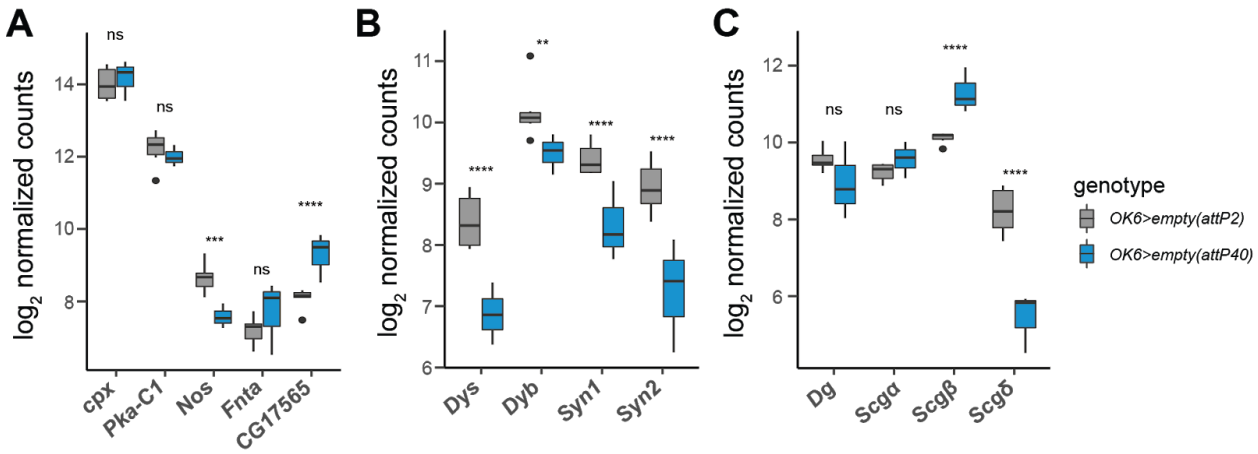

Figure 3.4) *attP40* mutants decreased expression of the intracellular components of the DGC and Nos. **A-C**) Boxplots showing $\log_2$ normalized expression of complexin and it's PTM enzymes (*cpx*, *Pka-C1*, *Nos*, *Fnta*, *CG17565*; **A**), intracellular components of DGC (*Dys*, *Dyb*, *Syn1*, and *Syn2*; **B**), and the extracellular and transmembrane components of DGC (*Dg*, *Scgα*, *Scgβ*, and *Scgδ*; **C**) in *OK6>empty(attP2)* controls (grey) and *OK6>empty(attP40)* animals (blue). (BH-adjusted Wald test *p*-values, ns $p > 0.05$, * $p < 0.01$, ** $p < 0.001$, *** $p < 0.0001$, **** $p <$ 1e-05).

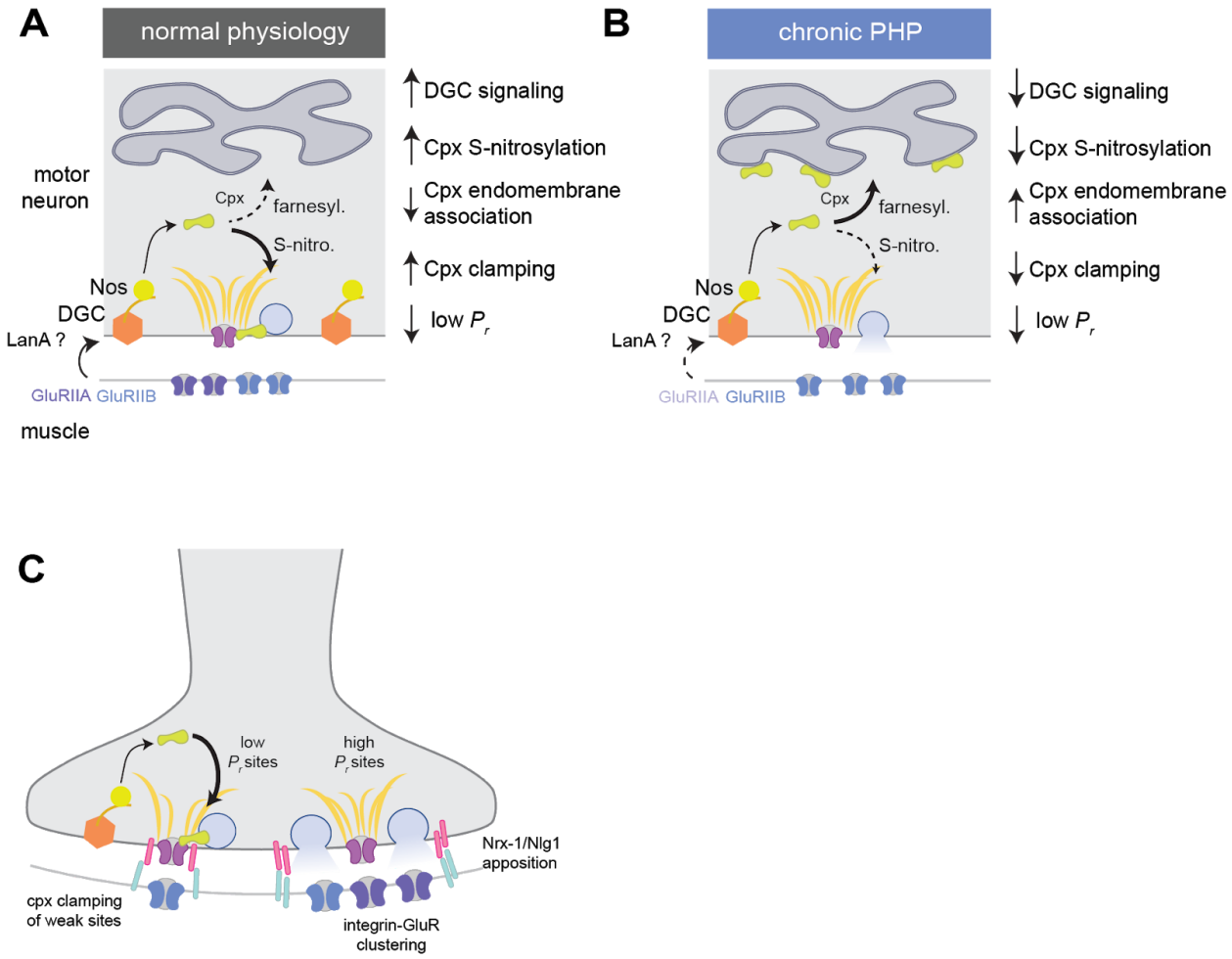

Figure 3.5) Proposed model of CAM involvement in chronic PHP. **A**) Model for cpx-mediated clamping of neurotransmission under normal physiological conditions. High expression of the DGC and Nos result in greater S-nitrosylation of cpx, which favors association with the AZ (Brp in yellow). Association of S-nitrosylated cpx reduces SV exocytosis in response to Ca^{2+} entry via voltage-gated Ca^{2+} channels (violet). **B**) Model for observed increase in P_r in chronic PHP. Decreased expression of the DGC and Nos and increased expression of farnesyltransferases, results in cpx retention in the endomembrane system. This relieves the clamping activity of cpx at the AZ, resulting in increased P_r and quantal content. **C**) Potential roles of CAMs in remodeling and regulating AZs. PHP-mediated AZ compaction and remodeling boosts AP-evoked transmission at a subset of sites. Integrin-mediated GluR clustering and neurexin/neuroligin-mediated (pink, cyan) AZ apposition bolster successful neurotransmission. Redistribution of cpx to partially assembled or weak sites reduces spontaneous release.

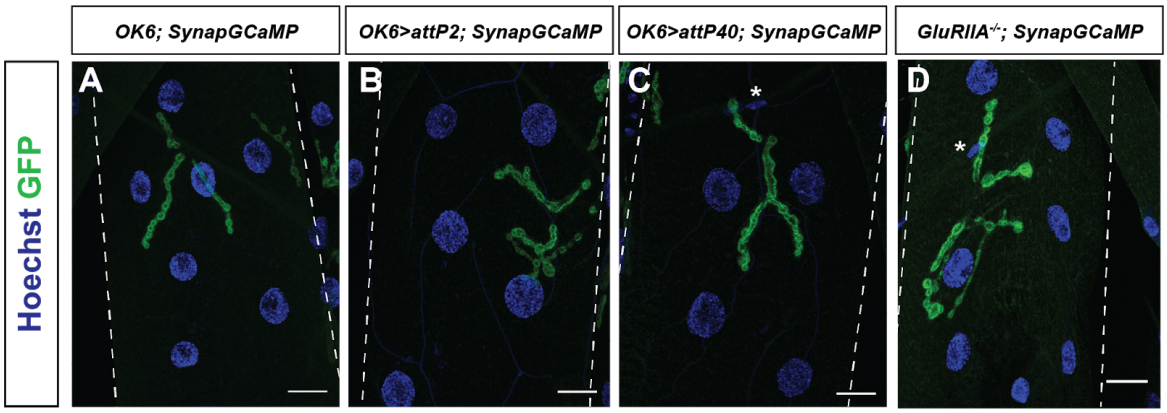

Supplementary Figure 3.1) *attP40* mutants do not have a nuclear localization defect. **A-D)** Confocal images of muscle 4 NMJs from *OK6;SynapGCaMP* (control, **A**), *OK6>attP2(empty);SynapGCaMP* (control for inserted pCaryP vector, **B**), *OK6>attP40(empty);SynapGCaMP* (*attP40* mutant, **C**), and *GluRIIA*$^{-/-}$*;MHC-GCaMP6f* (*GluRIIA*$^{-/-}$ mutant, **D**). SynapGCaMP shown in green for visualization of synapses and Hoechst is shown in blue for visualization of nuclei. (Scale bar, 20 μm; Dotted white line, border of muscle 4; Asterisk, nucleus of peripheral glia).

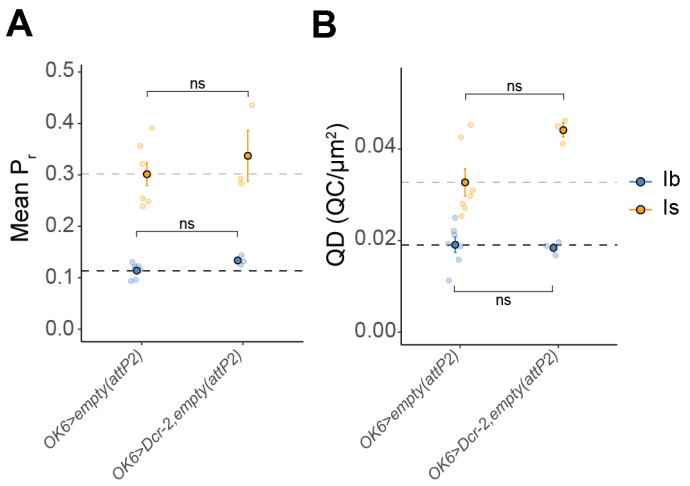

Supplementary Figure 3.2) *UAS-Dcr-2* does not alter synaptic function. **A**) Mean probability of vesicle release (P_r) per stimulus per NMJ by optical quantal analysis of Ib (blue) and Is (orange) terminals in *OK6>empty(attP2)* (*OK6>empty(attP2);SynapGCaMP*) and *OK6>Dcr-2,empty(attP2)* (*OK6>Dcr-2,empty(attP2);SynapGCaMP*). **B**) Quantal density (QD, area normalized quantal content) by optical quantal analysis. Genotypes and NMJ types are the same as in (**B**).

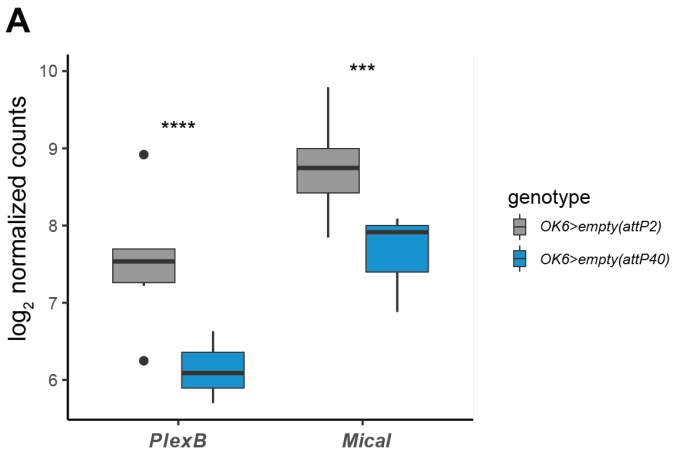

Supplementary Figure 3.3) *attP40* mutants have decreased expression of *PlexB* and *Mical*. **A)** Boxplot showing $\log_2$ normalized expression of *PlexB* and *Mical* in *OK6>empty(attP2)* controls (gray) and *OK6>empty(attP40)* animals (blue). (BH-adjusted Wald test *p*-values, ns $p > 0.05$, * $p > 0.01$, ** $p > 0.001$, *** $p > 0.0001$, **** $p >$ 1e-05).

Supplementary Table 3.1 Sample information for low-input RNA-seq of control and *attP40* mutant type I MNs

Run	Genotype	Biological replicates	Number of cells	Technical replicate
1	*OK6>empty(attP2)*	*n* = 12	6,414	OK6_ATTP2_001
1				OK6_ATTP2_002
1				OK6_ATTP2_003
2	*OK6>empty(attP2)*	*n* = 10	3,530	OK6_ATTP2_101
2				OK6_ATTP2_102
2				OK6_ATTP2_103
3	*OK6>empty(attP40)*	*n* = 12	8,228	OK6_ATTP40_001
3				OK6_ATTP40_002
3				OK6_ATTP40_003

Supplementary Table 2.2 Top 15 differentially expressed genes in *OK6>empty(attP40)* Type I MNs

Up-regulated genes				
FlyBase ID	Gene symbol	log-fold-change	*p*-value	Adjusted *p*-value
FBgn0011581	Ms	6.47	7.71E-35	1.23E-31
FBgn0031256	shv	2.34	4.34E-33	5.75E-30
FBgn0031037	CG14207	2.24	4.05E-31	4.60E-28
FBgn0027109	NPF	4.86	5.85E-29	5.81E-26
FBgn0051451	lncRNA:CR31451	2.37	1.38E-25	7.85E-23
FBgn0029868	ND-B16.6	3.16	4.01E-23	1.77E-20
FBgn0033934	CG17385	1.84	8.60E-23	3.28E-20
FBgn0266417	ringer	2.35	4.18E-22	1.45E-19
FBgn0016701	Rab4	2.04	3.13E-21	9.59E-19
FBgn0036133	CG7638	2.76	1.72E-20	4.73E-18
FBgn0001258	Ldh	2.33	3.20E-20	8.20E-18
FBgn0030521	CtsB1	3.30	3.14E-20	8.20E-18
FBgn0037891	CG5214	1.95	3.82E-20	9.49E-18
FBgn0033132	Tsp42Ej	2.15	2.45E-19	4.85E-17
FBgn0035871	BI-1	1.92	4.37E-19	8.28E-17
Down-regulated genes				
FlyBase ID	Gene symbol	log-fold-change	*p*-value	Adjusted *p*-value
FBgn0034246	Dcr-2	-8.74	3.69E-180	2.93E-176
FBgn0000546	EcR	-3.97	2.58E-48	1.03E-44
FBgn0016076	vri	-3.47	1.06E-45	2.81E-42
FBgn0270928	VAChT	-2.37	1.97E-36	3.92E-33
FBgn0023388	Dap160	-2.30	6.38E-27	5.63E-24
FBgn0031414	eys	-2.53	1.54E-26	1.22E-23

FBgn0264502	CG43901	-2.59	2.76E-26	2.00E-23
FBgn0261556	CG42674	-2.21	7.27E-26	4.82E-23
FBgn0033159	Dscam1	-2.40	1.34E-25	7.85E-23
FBgn0037336	CG2519	-2.33	1.44E-24	7.60E-22
FBgn0024277	trio	-2.2	1.53E-24	7.60E-22
FBgn0036935	CG14186	-2.51	6.01E-24	2.81E-21
FBgn0000567	Eip74EF	-3.97	7.05E-23	2.95E-20
FBgn0083949	side-III	-3.21	8.65E-23	3.27E-20
FBgn0003499	sr	-2.61	1.97E-22	7.13E-20

References

Aberle, H., Haghighi, A.P., Fetter, R.D., McCabe, B.D., Magalhães, T.R., and Goodman, C.S. (2002). wishful thinking encodes a BMP type II receptor that regulates synaptic growth in Drosophila. Neuron *33*, 545–558.

Ahmad, K., Shaikh, S., Ahmad, S.S., Lee, E.J., and Choi, I. (2020). Cross-Talk Between Extracellular Matrix and Skeletal Muscle: Implications for Myopathies. Front. Pharmacol. *11*, 142.

Aoto, J., Martinelli, D.C., Malenka, R.C., Tabuchi, K., and Südhof, T.C. (2013). Presynaptic neurexin-3 alternative splicing trans-synaptically controls postsynaptic AMPA receptor trafficking. Cell *154*, 75–88.

Apel, E.D., Lewis, R.M., Grady, R.M., and Sanes, J.R. (2000). Syne-1, a dystrophin- and Klarsicht-related protein associated with synaptic nuclei at the neuromuscular junction. J. Biol. Chem. *275*, 31986–31995.

Armstrong, J.N., Saganich, M.J., Xu, N.-J., Henkemeyer, M., Heinemann, S.F., and Contractor, A. (2006). B-ephrin reverse signaling is required for NMDA-independent long-term potentiation of mossy fibers in the hippocampus. J. Neurosci. *26*, 3474–3481.

Ashley, J., Sorrentino, V., Lobb-Rabe, M., Nagarkar-Jaiswal, S., Tan, L., Xu, S., Xiao, Q., Zinn, K., and Carrillo, R.A. (2019). Transsynaptic interactions between IgSF proteins DIP-α and Dpr10 are required for motor neuron targeting specificity. Elife *8*.

Atwood, H.L., Govind, C.K., and Wu, C.F. (1993). Differential ultrastructure of synaptic terminals on ventral longitudinal abdominal muscles in Drosophila larvae. J. Neurobiol. *24*, 1008–1024.

Banovic, D., Khorramshahi, O., Owald, D., Wichmann, C., Riedt, T., Fouquet, W., Tian, R., Sigrist, S.J., and Aberle, H. (2010). Drosophila neuroligin 1 promotes growth and postsynaptic differentiation at glutamatergic neuromuscular junctions. Neuron *66*, 724–738.

Berger, C., Harzer, H., Burkard, T.R., Steinmann, J., van der Horst, S., Laurenson, A.-S., Novatchkova, M., Reichert, H., and Knoblich, J.A. (2012). FACS purification and transcriptome analysis of drosophila neural stem cells reveals a role for Klumpfuss in self-renewal. Cell Rep. *2*, 407–418.

Beumer, K.J., Rohrbough, J., Prokop, A., and Broadie, K. (1999). A role for PS integrins in morphological growth and synaptic function at the postembryonic neuromuscular junction of Drosophila. Development *126*, 5833–5846.

Bogdanik, L., Framery, B., Frölich, A., Franco, B., Mornet, D., Bockaert, J., Sigrist, S.J., Grau, Y., and Parmentier, M.-L. (2008). Muscle dystroglycan organizes the postsynapse and regulates presynaptic neurotransmitter release at the Drosophila neuromuscular junction. PLoS One *3*,

e2084.

Böhme, M.A., McCarthy, A.W., Grasskamp, A.T., Beuschel, C.B., Goel, P., Jusyte, M., Laber, D., Huang, S., Rey, U., Petzoldt, A.G., et al. (2019). Rapid active zone remodeling consolidates presynaptic potentiation. Nat. Commun. *10*, 1085.

Bozdagi, O., Shan, W., Tanaka, H., Benson, D.L., and Huntley, G.W. (2000). Increasing numbers of synaptic puncta during late-phase LTP: N-cadherin is synthesized, recruited to synaptic sites, and required for potentiation. Neuron *28*, 245–259.

Caussinus, E., Colombelli, J., and Affolter, M. (2008). Tip-cell migration controls stalk-cell intercalation during Drosophila tracheal tube elongation. Curr. Biol. *18*, 1727–1734.

Chiba, A., Snow, P., Keshishian, H., and Hotta, Y. (1995). Fasciclin III as a synaptic target recognition molecule in Drosophila. Nature *374*, 166–168.

Cho, R.W., Buhl, L.K., Volfson, D., Tran, A., Li, F., Akbergenova, Y., and Littleton, J.T. (2015). Phosphorylation of Complexin by PKA Regulates Activity-Dependent Spontaneous Neurotransmitter Release and Structural Synaptic Plasticity. Neuron *88*, 749–761.

Contractor, A., Rogers, C., Maron, C., Henkemeyer, M., Swanson, G.T., and Heinemann, S.F. (2002). Trans-synaptic Eph receptor-ephrin signaling in hippocampal mossy fiber LTP. Science *296*, 1864–1869.

Davis, G.W., and Goodman, C.S. (1998). Synapse-specific control of synaptic efficacy at the terminals of a single neuron. Nature *392*, 82–86.

Davis, G.W., and Müller, M. (2015). Homeostatic control of presynaptic neurotransmitter release. Annu. Rev. Physiol. *77*, 251–270.

Davis, G.W., DiAntonio, A., Petersen, S.A., and Goodman, C.S. (1998). Postsynaptic PKA controls quantal size and reveals a retrograde signal that regulates presynaptic transmitter release in Drosophila. Neuron *20*, 305–315.

Dietzl, G., Chen, D., Schnorrer, F., Su, K.-C., Barinova, Y., Fellner, M., Gasser, B., Kinsey, K., Oppel, S., Scheiblauer, S., et al. (2007). A genome-wide transgenic RNAi library for conditional gene inactivation in Drosophila. Nature *448*, 151–156.

Elhanany-Tamir, H., Yu, Y.V., Shnayder, M., Jain, A., Welte, M., and Volk, T. (2012). Organelle positioning in muscles requires cooperation between two KASH proteins and microtubules. J. Cell Biol. *198*, 833–846.

Frank, C.A., Kennedy, M.J., Goold, C.P., Marek, K.W., and Davis, G.W. (2006). Mechanisms underlying the rapid induction and sustained expression of synaptic homeostasis. Neuron *52*, 663–677.

Frank, C.A., Pielage, J., and Davis, G.W. (2009). A presynaptic homeostatic signaling system

composed of the Eph receptor, ephexin, Cdc42, and CaV2.1 calcium channels. Neuron *61*, 556–569.

Grady, R.M., Grange, R.W., Lau, K.S., Maimone, M.M., Nichol, M.C., Stull, J.T., and Sanes, J.R. (1999). Role for α-dystrobrevin in the pathogenesis of dystrophin-dependent muscular dystrophies. Nat. Cell Biol. *1*, 215–220.

Hoang, B., and Chiba, A. (2001). Single-cell analysis of Drosophila larval neuromuscular synapses. Dev. Biol. *229*, 55–70.

Hoffman, E.P., and Kunkel, L.M. (1989). Dystrophin abnormalities in Duchenne/Becker muscular dystrophy. Neuron *2*, 1019–1029.

Hong, H., Zhao, K., Huang, S., Huang, S., Yao, A., Jiang, Y., Sigrist, S., Zhao, L., and Zhang, Y.Q. (2020). Structural remodeling of active zones is associated with synaptic homeostasis. J. Neurosci.

Huber, W., Carey, V.J., Gentleman, R., Anders, S., Carlson, M., Carvalho, B.S., Bravo, H.C., Davis, S., Gatto, L., Girke, T., et al. (2015). Orchestrating high-throughput genomic analysis with Bioconductor. Nat. Methods *12*, 115–121.

Huntwork, S., and Littleton, J.T. (2007). A complexin fusion clamp regulates spontaneous neurotransmitter release and synaptic growth. Nat. Neurosci. *10*, 1235–1237.

Iyer, J., Wahlmark, C.J., Kuser-Ahnert, G.A., and Kawasaki, F. (2013). Molecular mechanisms of COMPLEXIN fusion clamp function in synaptic exocytosis revealed in a new Drosophila mutant. Mol. Cell. Neurosci. *56*, 244–254.

Jantrapirom, S., Nimlamool, W., Temviriyanukul, P., Ahmadian, S., Locke, C.J., Davis, G.W., Yamaguchi, M., Noordermeer, J.N., Fradkin, L.G., and Potikanond, S. (2019). Dystrobrevin is required postsynaptically for homeostatic potentiation at the Drosophila NMJ. Biochim. Biophys. Acta Mol. Basis Dis. *1865*, 1579–1591.

Johnson, K.G., Tenney, A.P., Ghose, A., Duckworth, A.M., Higashi, M.E., Parfitt, K., Marcu, O., Heslip, T.R., Marsh, J.L., Schwarz, T.L., et al. (2006). The HSPGs Syndecan and Dallylike bind the receptor phosphatase LAR and exert distinct effects on synaptic development. Neuron *49*, 517–531.

Kamimura, K., Odajima, A., Ikegawa, Y., Maru, C., and Maeda, N. (2019). The HSPG Glypican Regulates Experience-Dependent Synaptic and Behavioral Plasticity by Modulating the Non-Canonical BMP Pathway. Cell Rep. *28*, 3144–3156.e4.

Kittel, R.J., and Heckmann, M. (2016). Synaptic Vesicle Proteins and Active Zone Plasticity. Front. Synaptic Neurosci. *8*, 8.

Kurusu, M., Cording, A., Taniguchi, M., Menon, K., Suzuki, E., and Zinn, K. (2008). A screen of cell-surface molecules identifies leucine-rich repeat proteins as key mediators of synaptic

target selection. Neuron *59*, 972–985.

Lee, J.Y., Geng, J., Lee, J., Wang, A.R., and Chang, K.T. (2017). Activity-Induced Synaptic Structural Modifications by an Activator of Integrin Signaling at the Drosophila Neuromuscular Junction. J. Neurosci. *37*, 3246–3263.

Li, J., Ashley, J., Budnik, V., and Bhat, M.A. (2007). Crucial role of Drosophila neurexin in proper active zone apposition to postsynaptic densities, synaptic growth, and synaptic transmission. Neuron *55*, 741–755.

Love, M.I., Huber, W., and Anders, S. (2014). Moderated estimation of fold change and dispersion for RNA-seq data with DESeq2. Genome Biol. *15*, 550.

Markstein, M., Pitsouli, C., Villalta, C., Celniker, S.E., and Perrimon, N. (2008). Exploiting position effects and the gypsy retrovirus insulator to engineer precisely expressed transgenes. Nat. Genet. *40*, 476–483.

McDermott, S.M., Yang, L., Halstead, J.M., Hamilton, R.S., Meignin, C., and Davis, I. (2014). Drosophila Syncrip modulates the expression of mRNAs encoding key synaptic proteins required for morphology at the neuromuscular junction. RNA *20*, 1593–1606.

Missler, M., Südhof, T.C., and Biederer, T. (2012). Synaptic cell adhesion. Cold Spring Harb. Perspect. Biol. *4*, a005694.

Morel, V., Lepicard, S., Rey, A.N., Parmentier, M.-L., and Schaeffer, L. (2014). Drosophila Nesprin-1 controls glutamate receptor density at neuromuscular junctions. Cell. Mol. Life Sci. *71*, 3363–3379.

Mosca, T.J., Hong, W., Dani, V.S., Favaloro, V., and Luo, L. (2012). Trans-synaptic Teneurin signalling in neuromuscular synapse organization and target choice. Nature *484*, 237–241.

Mrestani, A., Kollmannsberger, P., Pauli, M., Repp, F., Kittel, R.J., Eilers, J., Doose, S., Sauer, M., Sirén, A.-L., Heckmann, M., et al. (2019). Active zone compaction for presynaptic strength.

Newman, Z.L., Hoagland, A., Aghi, K., Worden, K., Levy, S.L., Son, J.H., Lee, L.P., and Isacoff, E.Y. (2017). Input-Specific Plasticity and Homeostasis at the Drosophila Larval Neuromuscular Junction. Neuron *93*, 1388–1404.e10.

Orr, B.O., Fetter, R.D., and Davis, G.W. (2017). Retrograde semaphorin-plexin signalling drives homeostatic synaptic plasticity. Nature *550*, 109–113.

Packard, M., Jokhi, V., Ding, B., Ruiz-Cañada, C., Ashley, J., and Budnik, V. (2015). Nucleus to Synapse Nesprin1 Railroad Tracks Direct Synapse Maturation through RNA Localization. Neuron *86*, 1015–1028.

Peled, E.S., and Isacoff, E.Y. (2011). Optical quantal analysis of synaptic transmission in

wild-type and rab3-mutant Drosophila motor axons. Nat. Neurosci. *14*, 519–526.

Peled, E.S., Newman, Z.L., and Isacoff, E.Y. (2014). Evoked and spontaneous transmission favored by distinct sets of synapses. Curr. Biol. *24*, 484–493.

Petersen, S.A., Fetter, R.D., Noordermeer, J.N., Goodman, C.S., and DiAntonio, A. (1997). Genetic analysis of glutamate receptors in Drosophila reveals a retrograde signal regulating presynaptic transmitter release. Neuron *19*, 1237–1248.

Pfeiffer, B.D., Jenett, A., Hammonds, A.S., Ngo, T.-T.B., Misra, S., Murphy, C., Scully, A., Carlson, J.W., Wan, K.H., Laverty, T.R., et al. (2008). Tools for neuroanatomy and neurogenetics in Drosophila. Proc. Natl. Acad. Sci. U. S. A. *105*, 9715–9720.

Pfeiffer, B.D., Ngo, T.-T.B., Hibbard, K.L., Murphy, C., Jenett, A., Truman, J.W., and Rubin, G.M. (2010). Refinement of tools for targeted gene expression in Drosophila. Genetics *186*, 735–755.

van der Plas, M.C., Pilgram, G.S.K., Plomp, J.J., de Jong, A., Fradkin, L.G., and Noordermeer, J.N. (2006). Dystrophin is required for appropriate retrograde control of neurotransmitter release at the Drosophila neuromuscular junction. J. Neurosci. *26*, 333–344.

Pozo, K., and Goda, Y. (2010). Unraveling mechanisms of homeostatic synaptic plasticity. Neuron *66*, 337–351.

Reim, K., Wegmeyer, H., Brandstätter, J.H., Xue, M., Rosenmund, C., Dresbach, T., Hofmann, K., and Brose, N. (2005). Structurally and functionally unique complexins at retinal ribbon synapses. J. Cell Biol. *169*, 669–680.

Ren, Y., Kirkpatrick, C.A., Rawson, J.M., Sun, M., and Selleck, S.B. (2009). Cell type-specific requirements for heparan sulfate biosynthesis at the Drosophila neuromuscular junction: effects on synapse function, membrane trafficking, and mitochondrial localization. J. Neurosci. *29*, 8539–8550.

Robinson, S.W., Bourgognon, J.-M., Spiers, J.G., Breda, C., Campesan, S., Butcher, A., Mallucci, G.R., Dinsdale, D., Morone, N., Mistry, R., et al. (2018). Nitric oxide-mediated posttranslational modifications control neurotransmitter release by modulating complexin farnesylation and enhancing its clamping ability. PLoS Biol. *16*, e2003611.

Rogers, R.S., and Nishimune, H. (2017). The role of laminins in the organization and function of neuromuscular junctions. Matrix Biol. *57-58*, 86–105.

Rosenberg-Hasson, Y., Renert-Pasca, M., and Volk, T. (1996). A Drosophila dystrophin-related protein, MSP-300, is required for embryonic muscle morphogenesis. Mech. Dev. *60*, 83–94.

Sanyal, S. (2009). Genomic mapping and expression patterns of C380, OK6 and D42 enhancer trap lines in the larval nervous system of Drosophila. Gene Expr. Patterns *9*, 371–380.

Schmucker, D., Clemens, J.C., Shu, H., Worby, C.A., Xiao, J., Muda, M., Dixon, J.E., and Zipursky, S.L. (2000). Drosophila Dscam is an axon guidance receptor exhibiting extraordinary molecular diversity. Cell *101*, 671–684.

Siebert, M., Banovic, D., Goellner, B., and Aberle, H. (2009). Drosophila motor axons recognize and follow a Sidestep-labeled substrate pathway to reach their target fields. Genes Dev. *23*, 1052–1062.

Stewart, B.A., Atwood, H.L., Renger, J.J., Wang, J., and Wu, C.F. (1994). Improved stability of Drosophila larval neuromuscular preparations in haemolymph-like physiological solutions. J. Comp. Physiol. A *175*, 179–191.

Südhof, T.C. (2012). The presynaptic active zone. Neuron *75*, 11–25.

Tang, J., Maximov, A., Shin, O.-H., Dai, H., Rizo, J., and Südhof, T.C. (2006). A complexin/synaptotagmin 1 switch controls fast synaptic vesicle exocytosis. Cell *126*, 1175–1187.

Thomas, U., Kim, E., Kuhlendahl, S., Koh, Y.H., Gundelfinger, E.D., Sheng, M., Garner, C.C., and Budnik, V. (1997). Synaptic clustering of the cell adhesion molecule fasciclin II by discs-large and its role in the regulation of presynaptic structure. Neuron *19*, 787–799.

Titlow, J., Robertson, F., Järvelin, A., Ish-Horowicz, D., Smith, C., Gratton, E., and Davis, I. (2020). Syncrip/hnRNP Q is required for activity-induced Msp300/Nesprin-1 expression and new synapse formation. J. Cell Biol. *219*.

Tsai, P.-I., Kao, H.-H., Grabbe, C., Lee, Y.-T., Ghose, A., Lai, T.-T., Peng, K.-P., Van Vactor, D., Palmer, R.H., Chen, R.-H., et al. (2008). Fak56 functions downstream of integrin alphaPS3betanu and suppresses MAPK activation in neuromuscular junction growth. Neural Dev. *3*, 26.

Tsai, P.-I., Wang, M., Kao, H.-H., Cheng, Y.-J., Lin, Y.-J., Chen, R.-H., and Chien, C.-T. (2012). Activity-dependent retrograde laminin A signaling regulates synapse growth at Drosophila neuromuscular junctions. Proc. Natl. Acad. Sci. U. S. A. *109*, 17699–17704.

Walsh, F.S., and Doherty, P. (1997). Neural cell adhesion molecules of the immunoglobulin superfamily: role in axon growth and guidance. Annu. Rev. Cell Dev. Biol. *13*, 425–456.

Wang, T., Hauswirth, A.G., Tong, A., Dickman, D.K., and Davis, G.W. (2014). Endostatin is a trans-synaptic signal for homeostatic synaptic plasticity. Neuron *83*, 616–629.

Wickham, H. (2010). ggplot2: Elegant Graphics for Data Analysis (Use R!) (Springer).

Chapter 4:
Transcriptomic characterization of type I MNs with single-cell RNA-sequencing

This chapter contains co-authored material, representing a collaborative effort between myself and Shivali Baveja. I contributed to the experimental design and execution of single-cell RNA-sequencing experiments, including VNC dissections, FACS, RNA-seq library preparation and quality control, and data analysis, as well as immunofluorescence staining and confocal microscopy. S.B. performed the fillet preparations for the immunofluorescence experiments.

Abstract

The *Drosophila* larval NMJ is a highly stereotyped structure. During development a diverse array of glutamatergic type I motor neurons must accurately and precisely innervate their target muscles. However, the relationship between temporal identity, anatomical identity, biophysical characteristics, and the capacity for plasticity in type I motor neurons is unknown. We employ single-cell RNA-sequencing on purified motor neurons to transcriptionally characterize this diverse cell type. We find that motor neurons are primarily segregated into temporal cohorts. We also determine that these cohorts feature differential expression of cell adhesion molecules, activity-regulated genes, and voltage-gated ion channels, suggesting that temporal identity influences functional properties in this class of neuron.

Background

The *Drosophila* ventral nerve cord (VNC) must produce a genetically diverse repertoire of motor neurons (MNs) to ensure precise innervation of target muscles across the body plan of the larva. The VNC is responsible for transforming sensory input into motor output via synaptic transmission from MNs to their target muscles. The VNC is organized into three thoracic neuromeres and eight abdominal neuromeres which send projections to matching muscle segments (Ruiz‐Cañada and Budnik, 2006). Each neuromere includes approximately 32 glutamatergic MNs that supply the main excitatory drive to each muscle segment (Jan and Jan, 1976; Johansen et al., 1989). These MNs arise from divisions of three distinct type I neuroblasts (NBs) per hemineuromere during the mid-embryonic stages of development (citation). These MNs vary by hemilineage and birth order but must all extend their axons and form synaptic connections during the late embryonic stage to produce appreciable locomotion during the larval stages (Halpern et al., 1991; Sánchez-Soriano and Prokop, 2005). Type I MNs can be further classified into type Ib (big) and Is (small) based on their postsynaptic morphology. While type Ib and Is MNs express the same neurotransmitter and form convergent inputs, they differ in their firing patterns, capacities for short-term and homeostatic plasticity, and number of postsynaptic partners (Choi et al., 2004; Lnenicka and Keshishian, 2000; Melom et al., 2013; Newman et al., 2017; Peled and Isacoff, 2011).

Early work characterizing the molecular diversity of MNs focused on anatomical characterization of axon guidance mutants. Characterization of various *Drosophila* mutants led to the discovery of a plethora of transmembrane receptors and secreted factors that mediate axonal guidance and cell-adhesion (Bieber et al., 1989; Lin and Goodman, 1994; Mitchell et al., 1996; Nose et al., 1992; Pipes et al., 2001; Seeger et al., 1993; Yu et al., 1998). Mutants of such classes of genes produce several phenotypic classes of defects in target specificity, including axonal stalling at the appropriate target muscle, failure to defasciculate from nerve and overshooting the target muscle, and inappropriate branching (Arzan Zarin and Labrador, 2019).

However, individual mutations to these genes typically results in a low-penetrance phenotype, misexpression of these genes often robustly produce innervation defects (Goodman, 1996). This has lent support to the idea that target specificity is acquired by combinatorial expression of cell adhesion molecules, chemoattractants and chemorepuslants (Winberg et al., 1998; Zarin et al.,

2014). Concurrent work on transcriptional regulation of neuronal identity has shown that misexpression of cell-specific transcription factors (TFs) influences target muscle selection (Certel and Thor, 2004; Thor et al., 1999). Moreover, loss-of-function mutations in TFs produce similar innervation defects in MNs projecting to similar muscle groups (Garces and Thor, 2006; Landgraf et al., 1999), suggesting that combinatorial expression of TFs determines innervation. The relationship between TF expression and cell adhesion molecule (CAM) or morphogen expression has been specified for some subsets of neurons, but comprehensive integration of developmental, anatomical, and functional properties across type I MNs has not been completed.

Here we attempt to characterize the transcriptional diversity of type I MNs from the *Drosophila* larva with single-cell RNA-sequencing. From our experiments we show that differences in birth order are the greatest determinant of cell type among type I MNs, but that temporal birth order influences the expression of gene groups corresponding to postsynaptic target selection, axon guidance, and neuronal activity.

Results

Temporal patterning is the main driver of diversity in type I MNs of the larval VNC

To understand the nature of functional and genetic diversity among motor neurons, we devised a scheme to perform single-cell RNA-sequencing on purified motor neurons. We accomplished this by using the *OK6-Gal4* line which drives expression in motor neurons (Aberle et al., 2002; Sanyal, 2009). Combining this *Gal4* with a nuclear mCherry construct under *UAS* control, we were able to purify dissociated cells via fluorescence activated cell sorting (FACS) from ~20 dissected central nervous system (CNS) tissue samples (Figure 4.1A, C). Light-sheet microscopy imaging of mCherry expression in unfixed CNS tissue revealed expression in approximately 700 cells per VNC (Figure 4.1B). Our capture efficiency of 0.84% of mCherry-expressing neurons from dissociated brain tissue is therefore within the bounds of expected cell capture based on the number of neurons expected in the late 3rd instar stage (Homem and Knoblich, 2012; Scott et al., 2001).

We employed the 10X genomics platform to sequence a purified population of motor neurons. With this experimental protocol we captured and sequenced 881 cells (Figure 4.1D). We then removed low-quality or damaged cells from the data set by applying a minimum threshold for unique genes expressed and a maximum threshold for percent UMIs mapping to mitochondrial genes. We excluded doublets by setting a maximum threshold on the number of UMIs per cell. We performed outlier detection using principal component analysis (PCA) on quality measures, and determined that all outlying cells were also removed by our manual thresholds. We identified contaminating cells as either Type II neuroblasts (NBs) or their immature neural progenitors by their combinatorial expression of transcription factors involved in maintaining stem cell identity (see Methods). We also identified monoaminergic cells were broadly identified by their expression of various monoamine transporters, (*Vmat*, *SerT*, *DAT*), dopa decarboxylase (*Ddc*), or tyrosine hydroxylase (*ple*).

With the remaining cells we performed normalization, clustering, and differential expression (DE) inference to classify the cells (Figure 4.1D). Resampling-Based Ensemble Clustering (RSEC) was applied to generate a consensus of clustering results from the expression set filtered for 300, 500 or 1,000 genes with the greatest variance across the cells or reduced to the first 10, 15, or 30 principal components (PCs). The consensus clustering result yielded a final assembly of 8 clusters. All clusters of cells had high expression of classic neuronal markers (*embryonic lethal abnormal vision* (*elav*), *found in neurons* (*fne*), long non-coding RNA *noe* (*noe*)) and synaptic proteins (*neuronal Synaptobrevin* (*nSyb*) and *unc-13*) (Supplementary Figure 4.4), indicating that they are composed of mature neurons (DiAntonio et al., 1993; Kim et al., 1998; Robinow et al., 1988; Samson and Chalvet, 2003).

We next performed one-versus-all comparisons of clusters to identify marker genes for each subpopulation within our sample (Supplementary Table 4.3). We were surprised to find that cluster membership was dominated by a gradient of master regulators of temporal identity (Figure 4.2A-G). Expression of these regulators features a striking sequential gradient of *IGF-II mRNA binding protein* (*Imp*), *maternal gene required for meiosis* (*mamo*), *chronologically inappropriate morphogenesis* (*chinmo*), *Syncrip* (*Syp*), *prospero* (*pros)*, and *Ecdysone-induced protein 93F* (*Eip93F*) across clusters. The ratio of *Syp* to *Imp* in post-mitotic cells has been proposed as a marker for birth order, with high expression of *Imp* indicating an early-born temporal identity and *Syp* indicating a later birth order (Dillard et al., 2018; Liu et al., 2015; Ren et al., 2017; Rossi and Desplan, 2020; Syed et al., 2017; Yang et al., 2017). While opposing *Imp* and *Syp* gradients and their relationship of temporal identity has been best characterized in Type II NBs, which give rise to neurons and glia in the brain lobes, descending *Imp* gradients have been observed across different stem cell types and organisms (Nishino et al., 2013; Toledano et al., 2012). We examined the *Syp*/*Imp* ratio in cell clusters from the *OK6>UAS-mCherry-NLS* line and found that the clusters can be ordered along this temporal axis (Figure 4.2H). Since we observe this robust gradient in neurons from the VNC, which are derived from type I NBs, we conclude that this gradient of expression is also conserved within these lineages.

We sought to assign other markers of neuronal identity to these cell clusters by first examining the expression of any other TFs between clusters. Several homeobox-domain TFs also demarcated differences between clusters of cells, particularly in the later-born clusters (Figure 4.3). Cluster G had high expression of *Lim3*, *abnormal chemosensory jump 6* (*acj6)*, and *twin of eyeless* (*toy*) (Figure 4.3B, F, G). These TFs are expressed in the NB3-3 lineage, which gives rise to Eve(+) lateral interneurons responsible for proprioception and normal locomotion patterns (Birkholz et al., 2015; Lacin and Truman, 2016; Wreden et al., 2017). Clusters F and H express *cut* (*ct*) and *acj6*, while cluster F additionally expresses *toy* (Figure 4.3 E, F, G). Early-born clusters A-C have sparse expression of these transcription factors, in addition to expression of *ventral veins lacking* (*vvl*, also known as *drifter*) whose expression is absent in later-born groups (Figure 4.3).

Several of these TFs are known to be involved in synaptic targeting both in motor neurons and in other classes of neurons in *Drosophila* (Komiyama et al., 2003; Thor et al., 1999). We next asked if cell-adhesion molecules (CAMs) involved in axon target recognition are DE between clusters of type I MNs. We answered this question by performing pairwise DE inference

between clusters, ignoring cluster G since it appears to be composed of interneurons. We found that several classes of CAMs are differentially-expressed between clusters of type I MNs (Supplementary Table 4.4), including those from the *beaten-path*, *sidestep*, and defective proboscis extension response (*dpr*) subfamilies of Immunoglobulin-like CAMs (Figure 4.4). These classes of genes are known to form intricate networks of interactions to coordinate synapse specificity and circuit assembly in the VNC, optic lobe, and antennal lobe (Carrillo et al., 2015; Özkan et al., 2013; Pipes et al., 2001; Tan et al., 2015). We find that these classes of CAMs are combinatorially expressed across clusters, with early-born clusters bearing greater resemblance to each other relative to late-born clusters (Figure 4.4). Although *beaten path*, *sidestep*, and *dpr* genes have mutually exclusive expression in the neurons of the adult *Drosophila* VNC, we find that there are overlapping expression profiles of these genes as has been observed from immunohistochemistry experiments on the embryonic VNC (Allen et al., 2019; Li et al., 2017). *Beat-Ic* and *beat-IIa* had fairly promiscuous expression across temporal cohorts of cells, while *beat-IV* was restricted to cluster H of late-born MNs and *beat-VII* was more greatly expressed in early-born clusters (Figure 4.4). Of the CAM genes examined we found that *Down syndrome cell adhesion molecule 2 (Dscam2*), *Fasciclin 2* (*Fas2*), and *Neuroglian* (*Nrg*) had the strongest correlation with birth order, while *dpr14* and *connectin* (*Con*) were anti-correlated (Figure 4.4). Taken collectively these data suggest that temporal order may have the ability to restrict circuit membership and target muscle selection.

Early-born identity is associated with higher expression of canonical ARGs, metabolic genes, and voltage-gated K+ channels

Seeking to better identify the membership of each cluster, we attempted to validate the expression of *pasilla* (*ps*), an mRNA-binding protein that we have found to be a marker gene for clusters A and B (Figure 4.5A, Supplementary Table 4.3). The *ps* expression pattern across type I MN clusters overlapped with the expression pattern of *para* (Figure 4.5B), the voltage-gated Na+ channel whose splice isoforms are regulated by *ps* (Lin et al., 2009, 2015). To identify which MNs make up these *ps*(+) clusters, we stained for pasilla in the *ShakB-Gal4* and *RN2-Gal4* lines, which drive expression of cytosolic tdTomato in restricted subsets of type I MNs (Fujioka et al., 2003; Takizawa et al., 2007). We found that pasilla was expressed in two dorsally-projecting MNs, the intersegmental nerve type Is MN (MNISN-Is, RP2) and the muscle 1-projecting type Ib MN (MN1-Ib, aCC) (Figure 4.5 C, D-D'). Pasilla expression was absent from the ventrally-projecting Is MN (MNISNb/d-Is) and laterally-projecting Is MN (SNa-Is) (Figure 4.5 C-C'). These data suggest that temporal identity is a greater determinant genetic diversity than functional differences between type Is and type Ib MNs.

Since expression of *ps* increases persistent sodium current and the voltage-sensitivity of *para*, we wondered if cells constituting early-born clusters had other DE genes that might influence the biophysical properties. We found that *stripe* (*sr*; mammalian homolog, EGR1), *Hr38* (mammalian homolog, Nurr1), *CG14186,* and *cabut* (*cbt*; mammalian homolog, *Krüppel-like factor 11*) had greater expression in early-born clusters (Figure 4.6A, Supplementary Table 4.3). These genes make up the canonical Ca^{2+}-responsive activity regulated genes (ARGs) downstream of *c-Fos* (*Drosophila* name, *kayak*) and have increased expression in response to neuronal activity (Chen et al., 2016; Guan et al., 2005). We also noticed that the genes in the

glycolysis and gluconeogenesis pathway were similarly upregulated in early-born clusters (Figure 4.6B), indicating that the cells composing these clusters have greater metabolic activity.

Since early-born clusters have greater markers of neural activity, we next asked if there is a relationship between temporal identity and the expression of voltage-gated K+ channels and their auxiliary subunits. Loss of function mutations to *ps* rescue epileptic activity in fly lines with "bang-sensitive" or "shaking" phenotypes, many of which are caused by loss of function mutations to voltage-gated K+ channels (Pavlidis and Tanouye, 1995). We found that *slowpoke* (*slo*), *hyperkinetic* (*Hk*), *Ih*, and *Shab* had increased expression in early-born clusters, while *Shaker* (*Sh*) and *SKIP* are up-regulated in late-born identities (Figure 4.6C). Each of these proteins are important for shaping the components of an action potential, with Shab contributing to repolarization after action potential firing and Sh and Hk shaping fast-inactivating currents that influence spike initiation (Chouinard et al., 1995; Covarrubias et al., 1991; Peng and Wu, 2007; Schwarz et al., 1988; Tsunoda and Salkoff, 1995). Slo mediates a Ca^{2+} dependent K+ current, and contributes to action potential repolarization and interspike interval (Elkins and Ganetzky, 1988; Elkins et al., 1986). Thus, the expression pattern of *slo*, *Shab*, *Sh*, and *Hk* across temporal cohorts, combined with increased expression of ARGs and metabolic genes, suggests that birth order is related to the biophysical properties and firing dynamics of mature neurons.

Conclusions and Discussion

Here we demonstrate with single-cell RNA-sequencing that transcriptional diversity among MNs from the 3rd instar *Drosophila* larvae is most greatly influenced by temporal identity. We establish that type I MNs can be ordered on an opposing temporal gradient of *Imp* and *Syncrip*, similar to the progeny of type II NBs in the larval brain. We also find that these temporally ordered clusters of cells differentially express Homeobox-like TFs and CAMs, similar to neuronal populations identified in the adult VNC (Allen et al., 2019). Finally, we show that temporal identity is associated with markers of function, including the expression of ARGs, metabolic genes, and voltage-gated ion channels.

<u>The challenge of mapping transcriptionally-determined cell types onto anatomical and functional categories</u>

To ensure proper innervation and circuit membership, both motor neurons and muscle must express a complex ensemble of cell adhesion molecules and secreted factors. From our single-cell sequencing data we show that temporal cohorts of type I MNs have combinatorial expression of several classes of CAMs, particularly from the Immunoglobulin-like superfamily.

Mutation of individual genes belonging to the *beaten path*, *sidestep*, or *dpr* families result in inappropriate targeting of motor axons during embryonic development (citation). However, it is unknown if these gene expression patterns are transient or if they are maintained in the 3rd instar larval stage. Evidence suggests that gene expression patterns of these CAMs are dynamic. For example, the genes of the *beaten path* family are combinatorially expressed in the RP1-4 and aCC MNs of the late stage embryo, but these genes have mutually exclusive expression patterns in the neurons of the adult VNC (Allen et al., 2019; Li et al., 2017). Since we observe

combinatorial expression among temporal cohorts of MNs, it is likely that clusters also represent groups of MNs that project to similar, but not strictly unique, muscle groups.

Assigning temporal cohorts of MNs to functional, physiologically defined categories remains similarly challenging. Type I MNs are divided into type Ib and Is MNs based on the macroscopic appearance of their associated postsynaptic structures (Packard et al., 2015), but they differ in the number of muscle segments with which they form synapses, their biophysical properties, and their capacity for short and long-term modes of plasticity (Atwood and Klose, 2009; Lnenicka and Keshishian, 2000; Newman et al., 2017). Current clamp experiments on individual type I MNs have shown that they vary in the threshold of current required to evoke spiking activity, delay to first spike, and kinetics of activation (Choi et al., 2004). Despite the wealth of functional information about the differences between type Ib and Is MNs, the nature of genetic diversity between the two classes remains difficult to address. Indeed, the cluster of early-born MNs, specifically expressing *pasilla*, a gene known to influence action potential firing, was found to be composition of both type Ib and Is MNs.

The difficulty in identifying transcriptional differences type Ib and Is MNs are derived from several overlapping NB lineages, which don't follow a myotonic map. For example, the two dorsally-projecting MNs labeled by the *RN2-Gal4*, MNISN-Is and MN1-Ib, are produced from a separate neuroblast lineage from the remaining dorsally-projecting Ib MNs (NB 7-1 lineage) (Broadus et al., 1995; Meng et al., 2019; Schmid et al., 1999). A screens of the Janelia FlyLight Gal4 collection has identified new lines which express in two type Is MNs per hemisegment (MNISN-Is and MNISNb/d-Is) and another which has exclusive expression in MN1-Ib (Pérez-Moreno and O'Kane, 2019). Incidentally, the MN1-Ib *Gal4* insertion in this study maps to the region proximal to *dpr4* and *dpr5*, while the Is driver maps to a region near the *DIP-α* gene. However, MultiColor FlpOut combined with lineage-specific *Gal4* lines to visualize more classes of MNs at the 3rd instar stage is a promising tool for validating clusterwise gene expression differences with anatomical and functional classifications of type I MNs.

How does temporal identity influence biophysical firing properties?

From our single-cell sequencing data, we show that type I MNs have differential expression of activity-regulated genes downstream of *c-Fos*, which are regulated by neuronal activity in *Drosophila* (Chen et al., 2016; Guan et al., 2005). We also show that early temporal identity is correlated with increased expression of metabolic genes, a phenomenon that has also been observed in the adult fly CNS (Davie et al., 2018). Finally, we show that voltage-gated ion channels are differentially expressed between temporal cohorts.

These findings agree well with studies that misexpress spatially and temporally-restricted TFs in NB lineages that give rise to MNs. Overexpression of *Krüppel* in 3rd instar larval motor neurons results in increased expression *Sh*, *Shab*, and *slo*, a process also observed to maintain K+ homeostasis in *Shal* loss of function mutants (Kulik et al., 2019; Parrish et al., 2014). Similarly, ectopic expression of *tup*, which is normally expressed in embryonic ventrally-projecting MNs, can reduce levels of *Sh* expression (Wolfram et al., 2012, 2014). Precocious expression of *hunchback (Hb)*, an early temporal identity TF, in the NB3-1 lineage results in a larger number

of MNs with RP1/4 markers (larval MN14-Ib and MN30-Ib) at the expense of RP3 (MN6/7-Ib) and RP5 (MNISNb/d-Is) identities (Meng et al., 2020). Not only is circuit membership of these MNs altered, but so are their plasticity properties. Aberrant MN30-Ib neurons in NB3-1>*Hb* larvae have decreased amplitude and frequency of spontaneous neurotransmission, but increased quantal content, a hallmark of homeostatic plasticity. While many questions remain on how MNs acquire their homeostatic set points for firing and synaptic transmission over developmental time, improvements in integrating *post hoc* functional genomics measurements with electrophysiological experiments make addressing the relationship between developmental identity and the capacity for plasticity and homeostasis more amenable.

Methods

Fly Stocks

Drosophila melanogaster stocks bearing transgenes to drive nuclear mCherry or cytosolic tdTomato in type I MNs (*OK6-Gal4*, (Aberle et al., 2002; Sanyal, 2009), BDSC #64199; *UAS-mCherry-NLS*, Caussinus et al., 2008, BDSC #38424; *UAS-tdTomato*; Newman et al., 2017), cytosolic tdTomato in dorsally projecting MNs (*RN2-Gal4*, Fujioka et al., 2003, BDSC #7473), and cytosolic tdTomato in type Is MNs (*ShakB-Gal4*, Jacobs et al., 2000, BDSC #51633) were bred and maintained in a w^{1118} background. All fruit fly cultures were raised on cornmeal and molasses media at 25°C.

Fruit fly 3rd instar larva with the following genotype were used for experiments described in this chapter:

w^{1118}*;OK6-Gal4/+;UAS-mCherry-NLS/+* (*OK6>UAS-mCherry-NLS*)
w^{1118}*;RN2-Gal4,UAS-tdTomato/+;+* (*RN2>UAS-tdTomato*)
w^{1118}*;UAS-tdTomato/+;ShakB-Gal4/+* (*ShakB>UAS-tdTomato*)

CNS Dissection

Prior to dissection OK6>UAS-mCherry-NLS 3rd instar larva were screened for the presence of nuclear mCherry in the VNC with ZEISS Axio Zoom v16 FL epifluorescence microscope. Brain and VNC tissue were dissected as described in Chapter 2.

CNS Dissociation

Tissue dissociation steps were performed as previously described in Chapter 2.

Fluorescence Activated Cell Sorting

Cells were assayed for viability as described in Chapter 2. Cells were sorted on a BD Influx Cell Sorter with 140 μm tubing at pressures < 12 PSI. The sorted population was chosen for high expression of nuclear mCherry (PE-Texas Red) and low Sytox Green fluorescence (GFP). Plots of FACS data were performed as described in Chapter 2.

10X Chromium scRNA-Seq Cell Capture, Library Preparation, and Sequencing

Cells were sorted into PBS with 5% FBS (Corning) prior to centrifugation, resuspension, and cell-counting. Cells were loaded onto a 10X Chromium chip and barcoded first-strand synthesis products were generated as per protocol for the 10X 3' single-cell RNA-seq protocol (v2 chemistry). cDNA amplification, SPRI-bead size selection, and library construction were also performed to kit specifications. Indexed, single-cell libraries were sequenced on Illumina Hi-Seq 4000 sequencers to produce 100 nt paired-end reads.

scRNA-Seq Alignment, Pre-processing, and Filtering

10X single-cell RNA-seq reads were first processed by converting .bcl files to .fastq files with CellRanger 'mkfastq' function. Reads were aligned to a custom reference genome built from Berkeley Drosophila Genome Project (dm6, release 75) genome assembly and the pUAST-mCherry-NLS vector sequence for the detection of the encoded transgenes used in these experiments. Alignment, barcode counting, UMI counting, and filtering were handled by CellRanger (version 2.0.0).

Filtering of the resulting gene-barcode matrix produced by CellRanger was performed with scater (ver 1.14.0, McCarthy et al., 2017) to identify low-quality cells and reduce technical effects in downstream analysis. Cells with fewer than 1000 unique genes, greater than 5 % counts from mitochondrial genes, or outliers detected from PCA on quality control measures were excluded from analysis. Genes with at least 1 count in more than five cells were considered detectable, and genes failing to meet this criteria were excluded from analysis. Cells in the 90th percentile of gene expression in at least two of the following genes, *Vmat*, *Ddc*, *SerT*, *DAT*, or *ple*. Type II neuroblasts (NBs) and their immature progeny were identified by 90th percentile expression of at least two of the following genes: *N* (Notch), *ase* (asense), *pnt* (pointed), *erm* (earmuff), *klu* (klumpfuss), *svp* (seven up), *esg* (escargot), *wor* (worniu), *sna* (snail), *E(spl)m8-HLH*, or *E(spl)mbeta-HLH*. *N* and *pnt* are expressed in Type II NBs, while *erm* and *ase* are expressed in immature neural progenitors (INPs) and ganglion mother cells, respectively, while the Snail family transcription factors, *klu*, *wor*, *sna*, and *esg*, were chosen for their roles in asymmetric cell division and maintenance of stem cell identity (Ashraf and Ip, 2001; Berger et al., 2012; Cai et al., 2001; Lai et al., 2012; Li et al., 2016; Xiao et al., 2012). Enhancer of split (*E(spl)*) complex proteins were chosen for their involvement in NB self-renewal (Zacharioudaki et al., 2012). Optic lobe contaminants were identified by 90th percentile expression of at least two of the following genes: *esg*, *Hey* (Hairy), *E(spl)m6-BFM*, *E(spl)m7-HLH, E(spl)m8-HLH*, or *E(spl)mbeta-HLH* (Apitz and Salecker, 2016; Brunet Avalos et al., 2019; Monastirioti et al., 2010; Pérez-Gómez et al., 2013; Zacharioudaki et al., 2012). Cells identified as belonging to any of the aforementioned contaminated cell types were filtered from the data set and excluded from downstream analysis.

scRNA-seq Normalization and Clustering

Several normalization methods were performed and assessed with SCONE (ver 1.10.0, Cole et al., 2019) to remove unwanted technical variation while avoiding the elimination of biological variation. Of the 64 normalization schemes, the top 10 were considered for downstream analysis (Supplementary Table 4.1). Of these schemes, combined use of scran (Lun et al., 2016), which pools cells to calculate size-factors, and RUVSeq (ver 1.20.0, Risso et al., 2014) using quality-related metadata, stably clustered cells.

Single-cell sequencing produces high dimensional datasets and dimensionality reduction is a crucial step towards identifying biological differences between cells. To classify cells based on broad differences in gene expression, we employed a method known as Resampling-based Sequential Ensemble Clustering (RSEC), which performs a battery of clustering methods and calculates a consensus clustering result (ver 2.0.2, Risso et al., 2018). Selected RSEC hyperparameters are documented in Supplementary Table 4.2. From this we determined that there are 8 populations of cells in the data set. Cells that failed to converge into these stable clusters were removed from downstream analyses.

Clustering results were visualized by creating a low-dimensional projection with UMAP (ver 0.2.4.1, Konopka, 2020). We determined the number of principal components (PCs) that represent meaningful latent variables for creating this projection. The counts matrix was filtered for the 500 genes with the greatest variance across the data set. A Jackstraw procedure over 10 permutations of the normalized data was performed to determine the number of significant PCs (Chung and Storey, 2015) (Supplementary Figure 4.1). A UMAP projection was calculated on the top 27 PCs over 300 epochs. We varied the number of neighbors in the UMAP calculation from 15-35 and found that the projections agreed with RSEC results (Supplementary Figure 4.2). We assessed the effectiveness of both normalization and clustering by mapping quality control data onto the UMAP projection to ensure that cluster identity was not dominated by technical parameters (Supplementary Figure 4.3).

scRNA-seq Differential Expression Testing

Identification of differentially expressed (DE) genes between each cluster was performed with the clusterExperiment (ver 2.6.1, Risso et al., 2018) implementation of limma (ver 3.42.2, Smyth, 2004). Visualization of clustering and DE analysis were performed with custom scripts built upon ggplot2 (ver 3.2.1, Wickham, 2010). Code used for all data analysis steps are in a Github repository at https://github.com/isacofflab/ok6_10x.

Immunohistochemistry and Confocal Microscopy

Larvae were screened for tdTomato expression prior to dissection and fixation. Immunohistochemistry was performed on fillet preparation of 3rd instar larvae with the brain and VNC left attached to the preparation. Samples were stained and mounted as described in Chapter 3.

Primary antibodies used in the experiments described in this chapter are rabbit anti-pasilla (Gill et al., 2017). Secondary antibodies used in the experiments described in this chapter are AlexaFluor 488-conjugated goat anti-rabbit (Invitrogen, Cat #A11008, RRID: AB_143165). Samples were imaged on a ZEISS LSM 710 microscope with a 40X oil-immersion objective. Maximum intensity projections were created and annotated using ImageJ (NIH).

Light-sheet Microscopy

Prior to dissection OK6>UAS-mCherry-NLS 3rd instar larva were screened for the presence of nuclear mCherry in the VNC with ZEISS Axio Zoom v16 FL epifluorescence microscope. Brain and VNCs were dissected in HL3 buffer on a Sylgard pad. Tissue was mounted unfixed in 0.5 % agarose (Denville Scientific) in a glass capillary tube with an inner diameter of ~ 1 mm (size 2, BRAND, Cat#701904) and imaged on Zeiss Lightsheet Z.1 microscope. Samples were imaged with dual side illumination with a 20X objective from two different views. Images were fused with the ZEN imaging software's registration algorithm.

Cells were counted by segmenting fused images in Imaris (Bitplane). Segmented portions of the image were thresholded to remove aberrant detection of fluorescent nuclei. Nuclei were counted and averaged between different views of the same specimen.

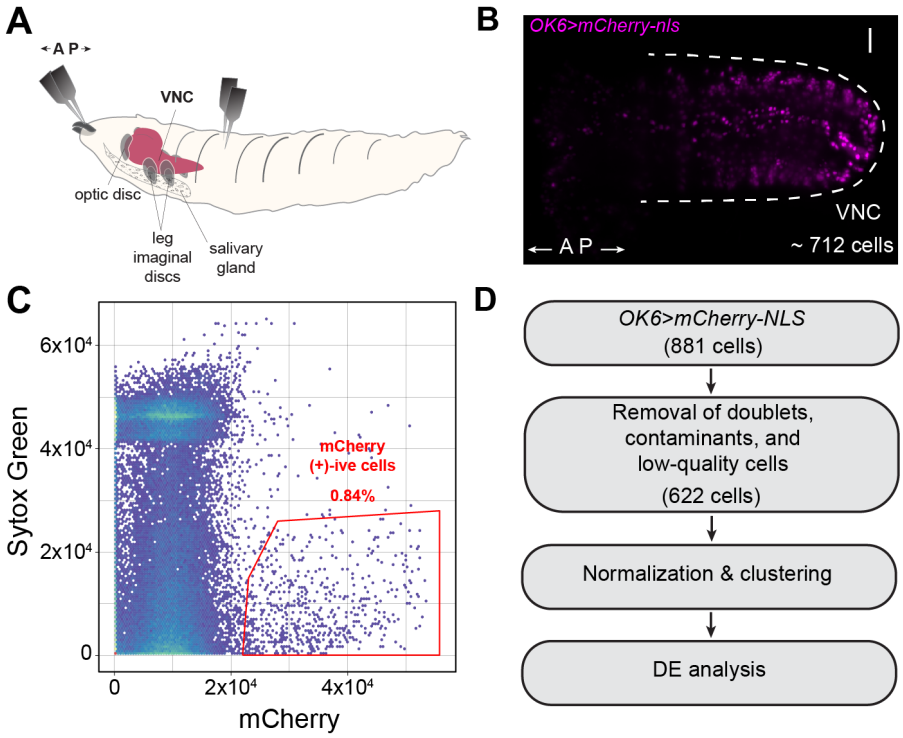

Figure 4.1) Scheme for single-cell RNA-sequencing of Type I MNs. **A)** Dissection of VNC from *OK6>UAS-mCherry-NLS* 3rd instar larva. **B)** Light sheet image of dissected *OK6>UAS-mCherry-NLS* VNC. mCherry fluorescence is visualized in magenta. Scale bar, 20 µm. Cell counts from light sheet imaging show that there are ~712 cells expressing this *Gal4* driver. **C**) FACS sorted population of *OK6>UAS-mCherry-NLS* against live/dead stain (Sytox Green). **D)** Workflow of 10x data analysis.

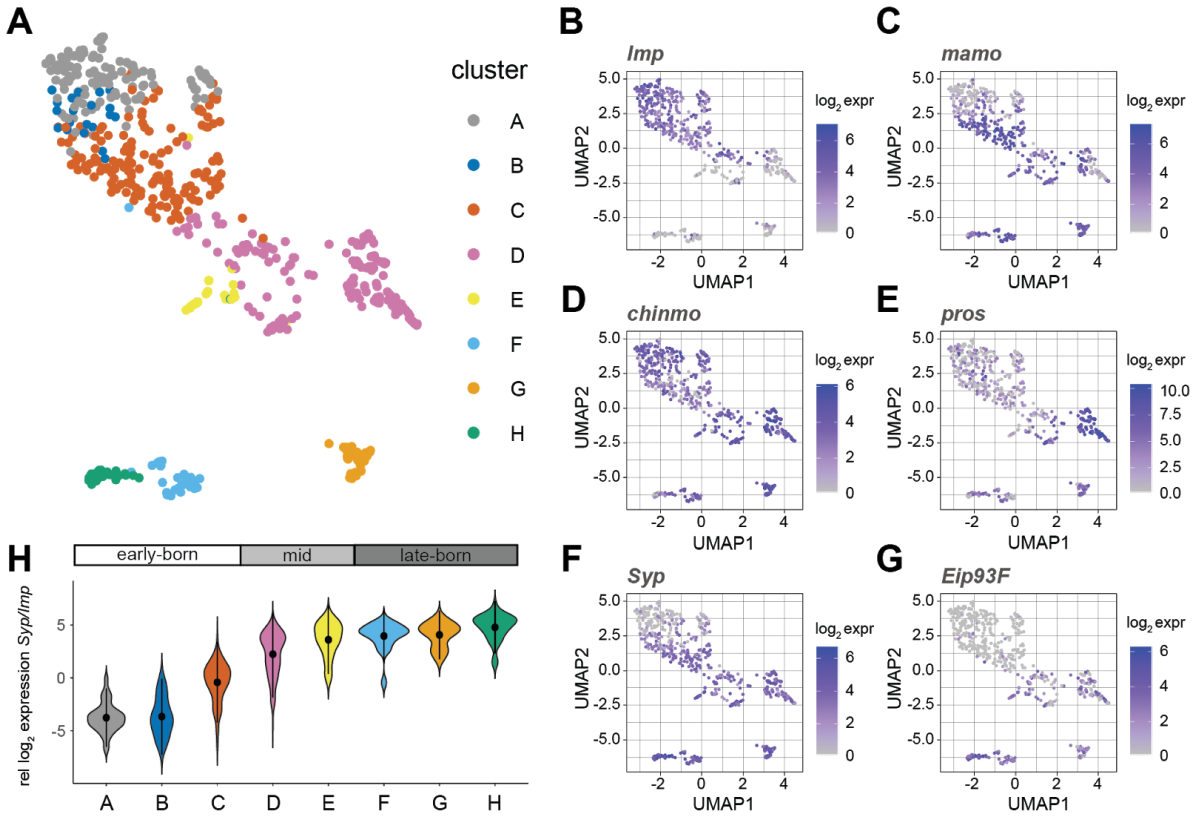

Figure 4.2) Unsupervised clustering of type I MNs segregates cells into temporal cohorts. **A)** UMAP projection of type I MNs on top 500 genes with greatest variance. **B-G)** Expression of temporal markers (*Imp*, *mamo*, *chinmo*, *pros*, *Syp*, and *Eip93F*). Expression is in units of $\log_2$ normalized pseudocounts. **H**) Relative $\log_2$ expression of *Syp* to *Imp* across clusters. Clusters are colored as in (**A**). Clusters A-C are early-born, D and E are mid-born, and F-H are late-born neurons.

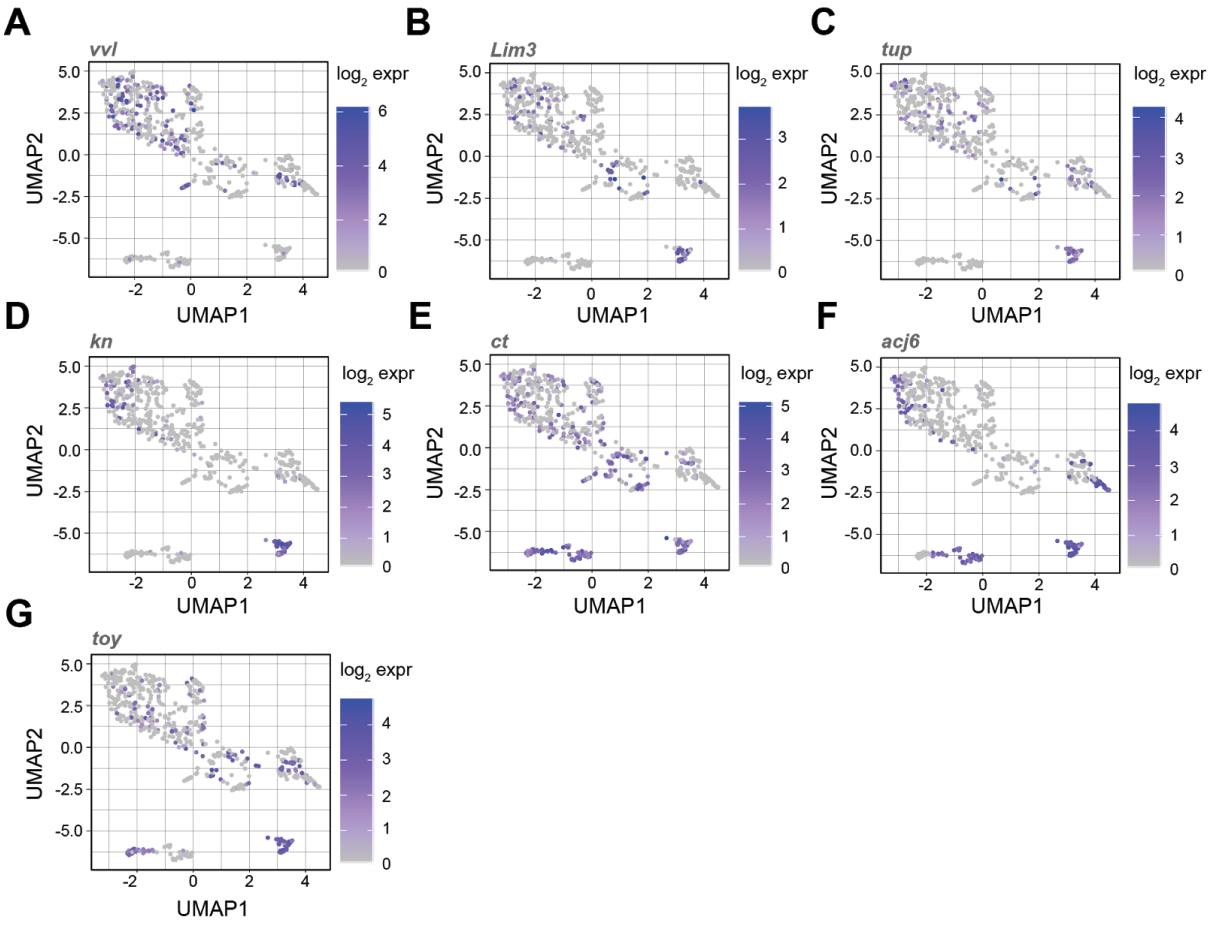

Figure 4.3) Late-born neurons have combinatorial expression of Homeobox-domain TFs. **A-G)** UMAP projections of single-cell expression of *vvl* (**A**), *Lim3* (**B**), *tup* (**C**), *kn* (**D**), *ct* (**E**), *acj6* (**F**), and *toy* (**G**). Units of expression are $\log_2$-transformed normalized pseudocounts.

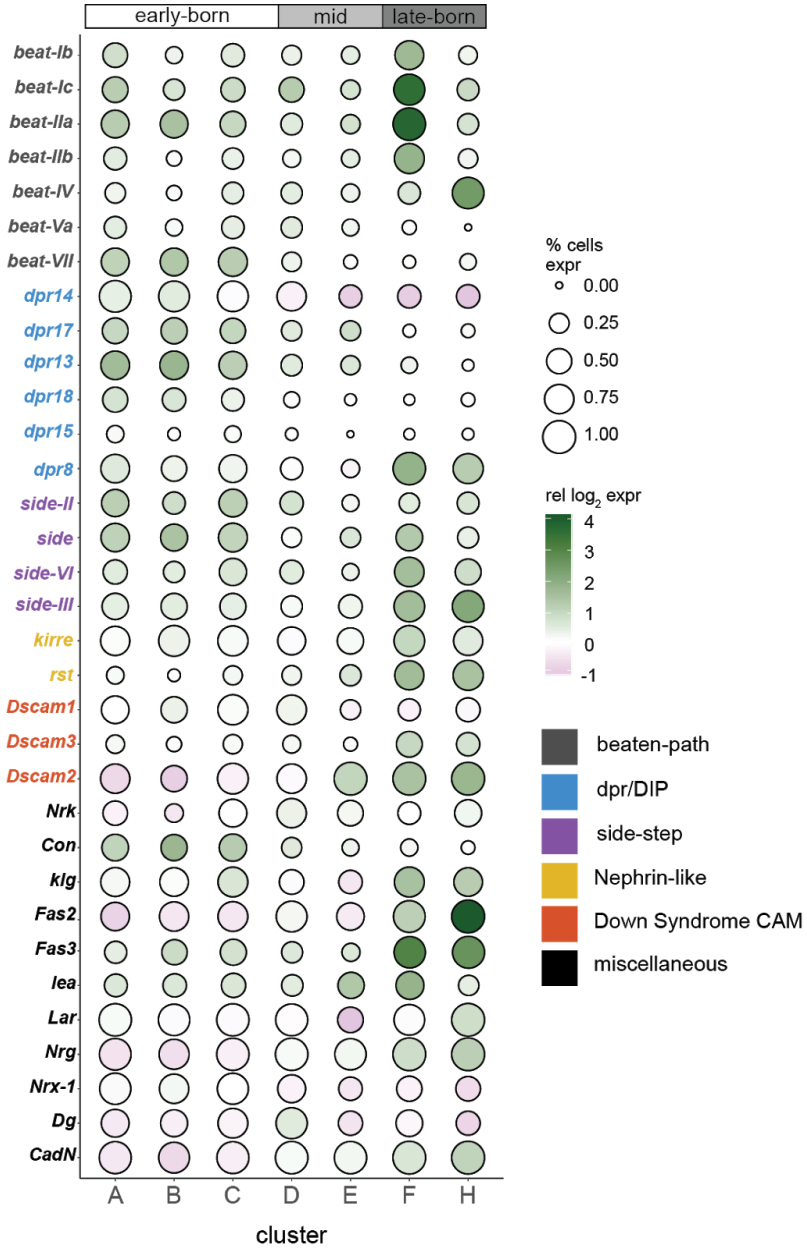

Figure 4.4) Pairwise comparisons of type I MN clusters are dominated by differences in CAM expression. Genes selected are DE between at least one pairwise combination between clusters with an adjusted *p*-value no greater than 1e-03. Gene expression within each cluster is represented by 1) the percentage of cells within each cluster with more than 0 counts and 2) the difference in $\log_2$-normalized expression from the median $\log_2$-transformed expression across all cells. Genes are grouped into the following CAM subfamilies: beaten-path (gray), dpr/DIP (blue), sidestep (purple), Nephrin-like (yellow), Down Syndrome CAM (red), and miscellaneous (Leucine-rich Repeat, Fibronectin, Receptor Tyrosine Kinase, and Cadherin families).

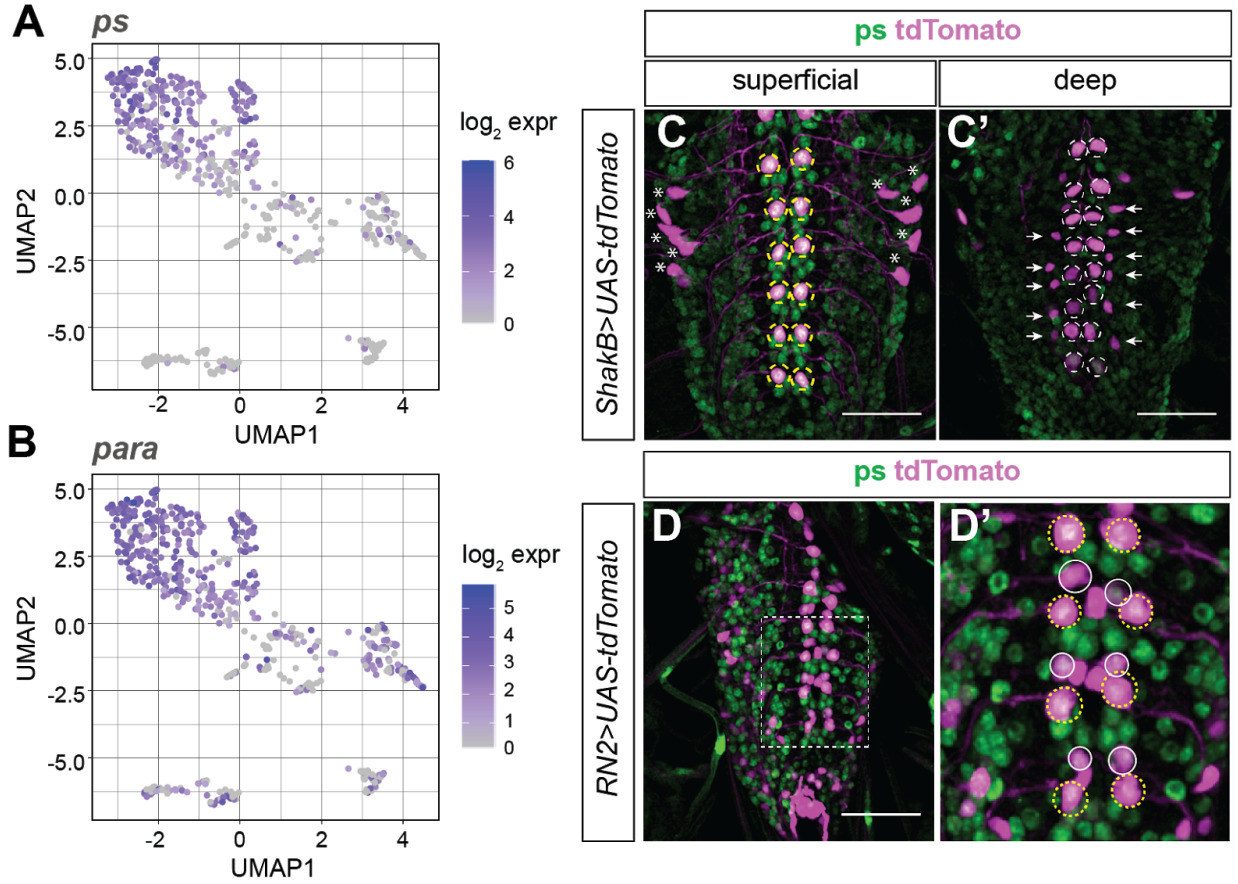

Figure 4.5) Early-born clusters of type I MNs are a mixture of type Ib and type Is MNs. **A-B)** Expression of pasilla (*ps*; **A**) and para (*para*; **B**) mapped UMAP space. **C-D)** Images of *ShakB>UAS-tdTomato* (**C-C'**) and *RN2>UAS-tdTomato* (**D-D')** VNC stained for pasilla (green). Native tdTomato fluorescence is in magenta. (Scale bar, 50 µm. Dashed white box inset, **D'.** Dashed yellow circles, MNISN-Is (RP2). Asterisk, MNSNa-Is. Dashed white circles, MNSNb/d-Is. Solid white circles, MN1-Ib (aCC). White arrow, interneuron).

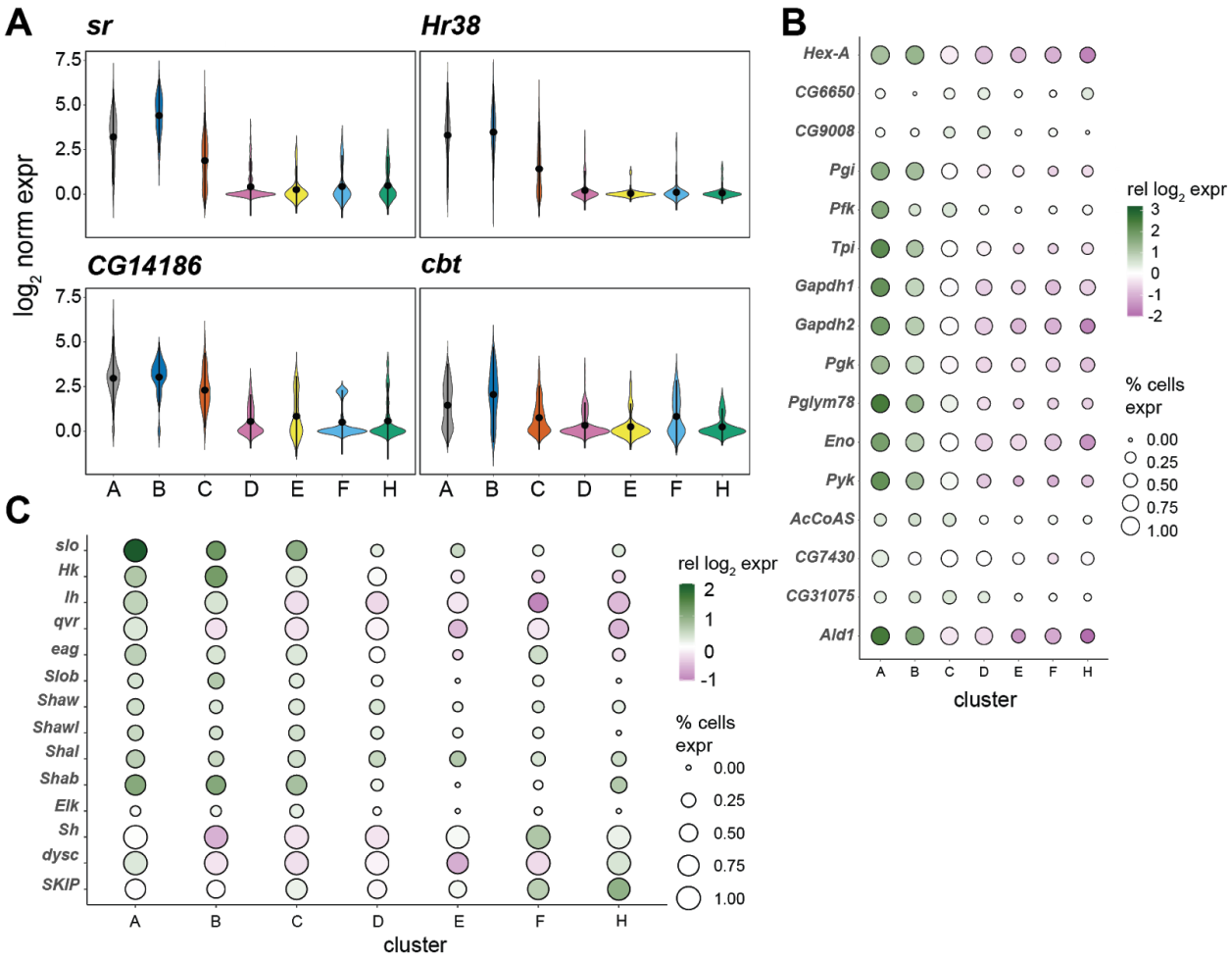

Figure 4.6) Temporal identity is correlated with expression of canonical ARGs, metabolic genes, and voltage-gated K+ channels. **A**) Expression of *Fos* effector genes, *sr* (top left), *Hr38* (top right), *CG14186* (bottom left), and *cbt* (bottom right), by cluster. Expression is measured in $\log_2$-transformed normalized pseudocounts. **B-C**) Expression of KEGG glycolysis and gluconeogenesis genes (**B**) and voltage-gated K+ channels (**C**) by cluster. Expression is represented as in Figure 4.4. Adjusted *p*-values of one versus all differences in average expression for selected genes is represented in Supplementary Table 4.3.

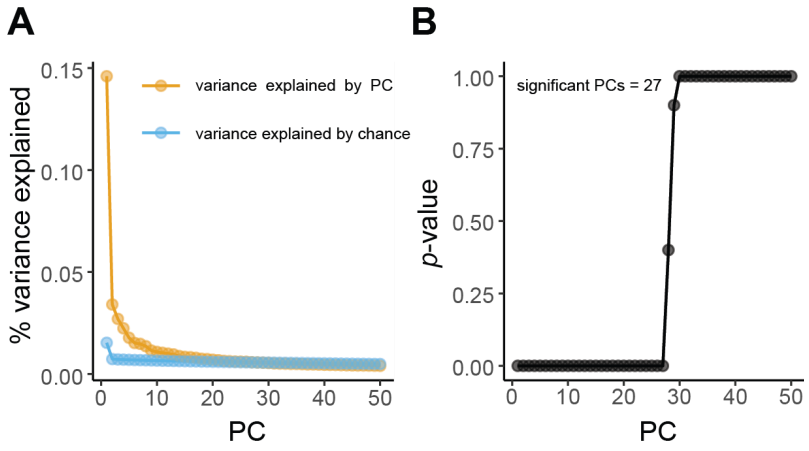

Supplementary Figure 4.1) Jackstraw procedure for identifying the optimal number of PCs for calculating the UMAP projection. **A**) Percent of the variance explained by PC of data set (yellow) versus percent variance explained by random permutations of the data (blue). **B**) *p*-value of each PC. PCs below a *p*-value of 0.05 represent latent variables of the data set.

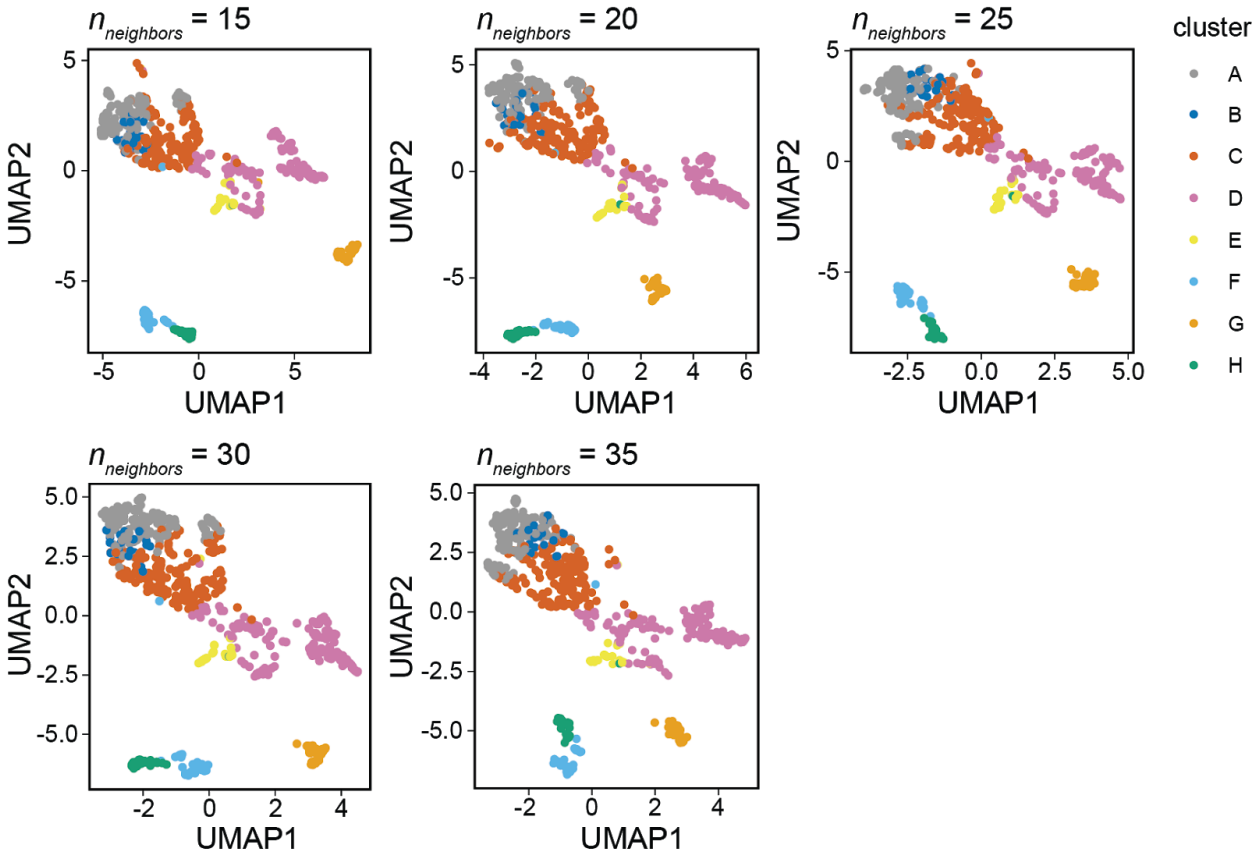

Supplementary Figure 4.2) Clustering results are stable over variations in UMAP hyperparameters. Cells in UMAP projection are colored by cluster membership as in Figure 4.2. UMAP projections vary by neighbors.

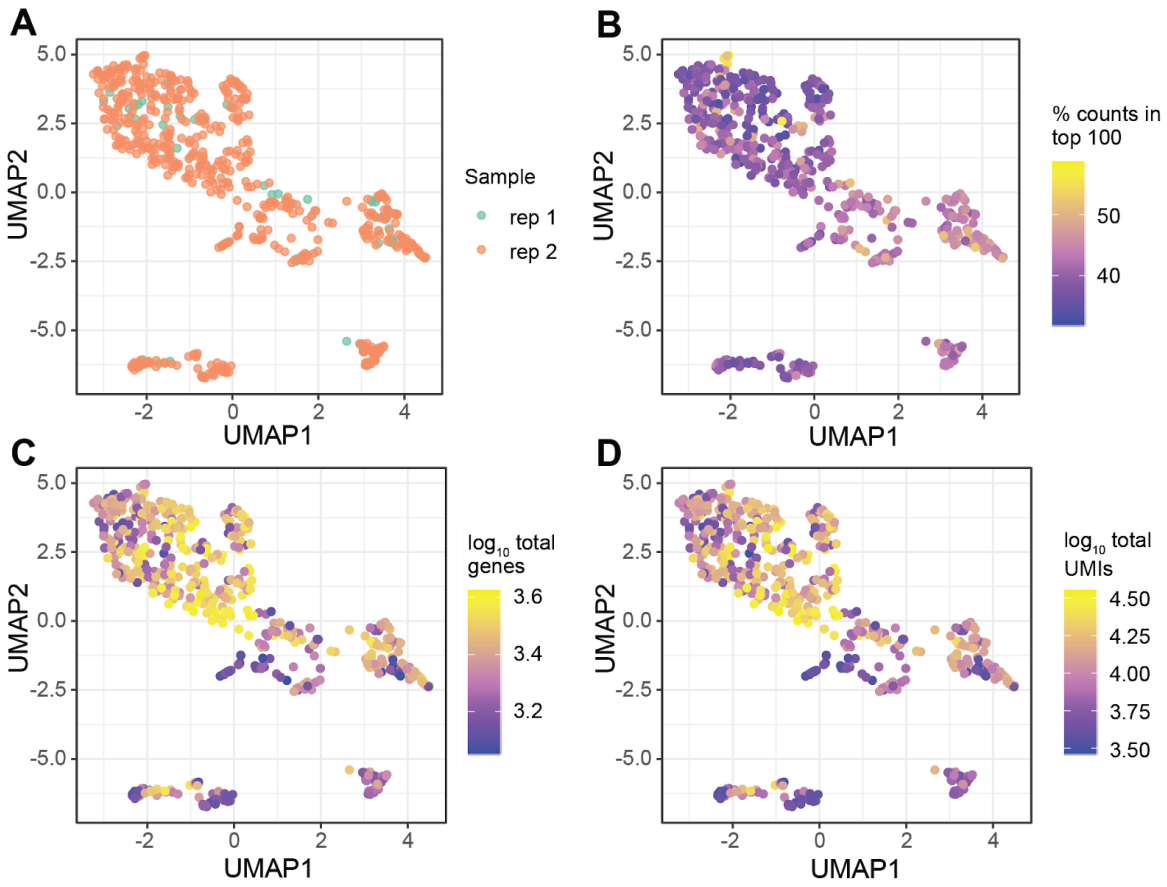

Supplementary Figure 4.3) Cluster membership is not determined by technical parameters. **A-D**) UMAP projections of single cells colored by replicate (**A**), percent of gene counts in the top 100 genes (**B**), $\log_{10}$ total unique genes (**C**), and $\log_{10}$ total UMIs (**D**).

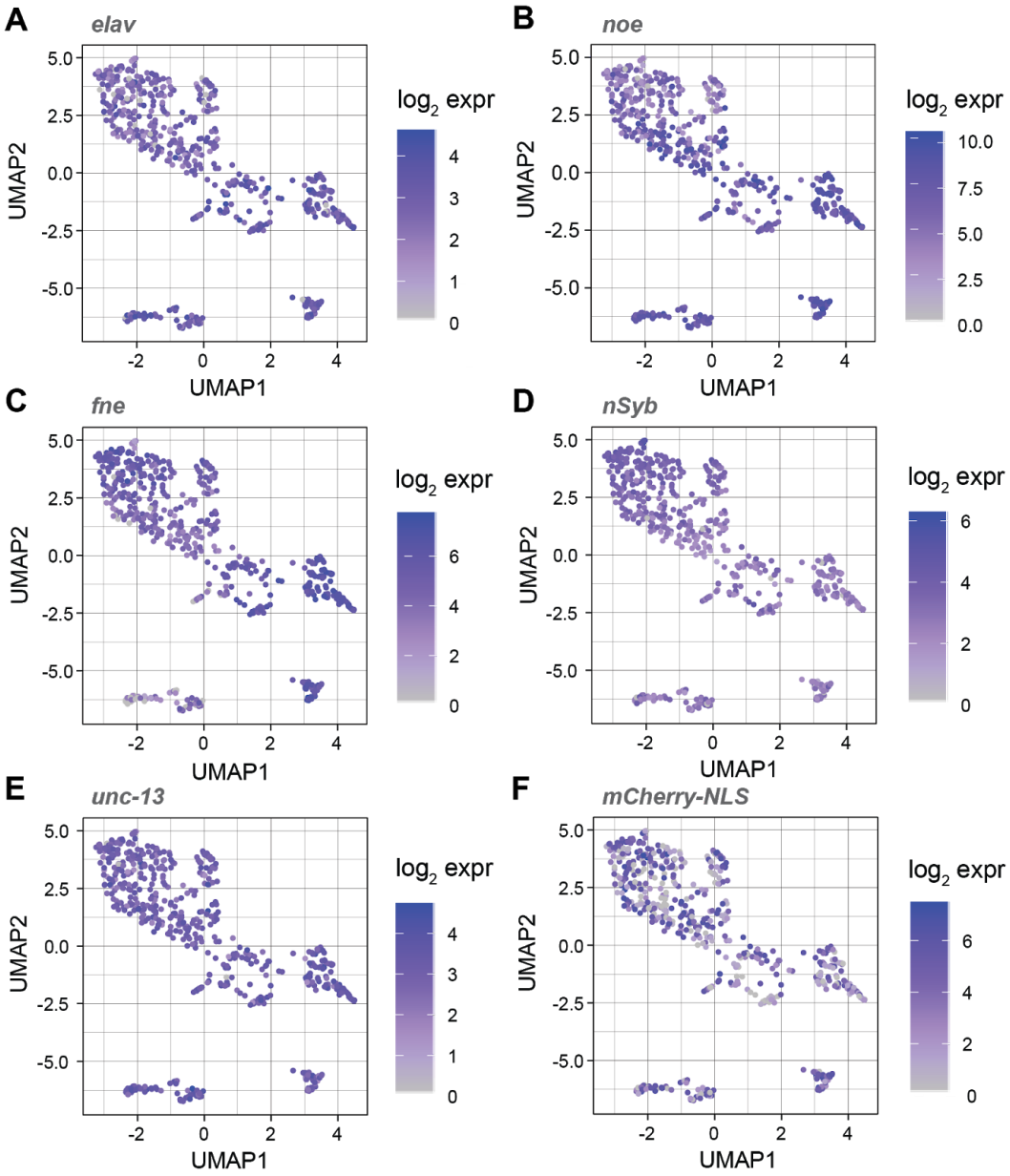

Supplementary Figure 4.4) Clusters express markers of mature neurons. **A-F**) UMAP projection of cells colored by $\log_2$ normalized pseudocounts of *elav* (**A**), *noe* (**B**), *fne* (**C**), *nSyb* (**D**), *unc-13* (**E**), and *mCherry-NLS* (**F**).

Supplementary Table 4.1 SCONE performance metrics

SCONE parameters	BATCH SIL	PAM SIL	EXP QC COR	RLE MED	RLE IQR	SCONE ranks
Metrics for Top 10 Ranked Normalizations						
none,fq,qc_k=3,no_bio,batch	0.0615	0.4051	-0.4214	0	-0.0321	57.3
none,fq,qc_k=2,no_bio,batch	0.0565	0.4139	-0.4856	0	-0.00328	56.5
none,fq,qc_k=3,no_bio,no_batch	0.0500	0.4145	-0.4782	0	-0.03514	55.3
none,tmm,qc_k=3,no_bio,batch	0.0543	0.4060	-0.4160	0	-0.0339	54.7
none,fq,qc_k=1,no_bio,batch	0.0607	0.4459	-0.4967	-2.41e-07	-0.0406	54.4
non,scran,qc_k=3,no_bio,batch	0.0607	0.4004	-0.4967	-2.16e-07	-0.0330	53.4
none,scran,qc_k=3,no_bio,batch	0.0564	0.4072	-0.4104	-2.43e-06	-0.0384	52.8
none,sum,qc_k=3,no_bio,batch	0.0588	0.3897	-0.3877	-4.23e-06	-0.0378	51.0
none,tmm,qc_k=3,no_bio,no_batch	0.0561	0.4464	-0.4980	-2.86e-07	-0.0417	50.8
none,fq,qc_k=1,no_bio,no_batch	0.0586	0.3987	-0.497	-1.55e-06	-0.0356	50.4

Supplementary Table 4.2 RSEC hyperparameters

Parameter	**Description**	**Value**
nPCADims	Number of PCs for clustering	10, 15, 30
nFiltDims	Number of genes to select for variance-based filtering	300, 500, 1000
α	Similarity value for finding a cluster in the co-occurence matrix	0.1, 0.2
β	Percentage of contingent cells as k is increased for sequential identification of a cluster	0.7, 0.8, 0.9
k_0	Number of clusters to find in each subsampling routine	2-8
minSize	Minimum threshold of cells in a cluster	3, 5, 10
clusterFunction	Algorithm to use for clustering	pam (partitioning-around medoids)

Supplementary Table 4.3 Top 10 differentially expressed genes in Type I MN Populations

Cluster	Gene	Log fold-change	Average expression	t	*p*-value	Adjusted *p*-value	B
A	Syp	-3.820	8.947	-34.13	1.76E-144	8.52E-140	319.263
A	Ald	3.731	8.979	29.02	1.42E-117	3.45E-113	257.669
A	Pglym78	3.405	7.271	26.72	3.31E-105	5.34E-101	229.260
A	PyK	3.204	7.444	26.49	5.26E-104	6.36E-100	226.499
A	Gapdh2	3.067	8.792	25.23	3.83E-97	3.09E-93	210.826
A	Gapdh1	3.078	7.949	24.69	3.01E-94	2.08E-90	204.149
A	Imp	3.179	8.358	22.76	8.29E-84	4.46E-80	180.312
A	Tpi	3.032	7.066	22.67	2.51E-83	1.21E-79	179.156
A	Eip93F	-2.187	6.770	-22.64	3.78E-83	1.66E-79	178.791
A	ps	2.860	7.072	22.48	2.71E-82	1.09E-78	176.815
B	sr	3.889	7.376	14.28	3.31E-40	2.14E-37	80.131
B	Eip93F	-2.265	6.770	-14.04	4.66E-39	2.78E-36	77.926
B	CG31221	4.666	8.404	12.81	1.69E-33	7.18E-31	65.197
B	IA-2	3.361	9.512	12.39	1.17E-31	4.53E-29	61.025
B	Imp	3.433	8.358	11.87	1.99E-29	6.37E-27	55.873
B	Mkp3	2.922	8.812	11.69	1.11E-28	3.33E-26	54.212
B	jeb	3.291	8.853	11.58	3.41E-28	9.64E-26	53.158
B	RpS3A	-1.669	11.364	-11.39	2.08E-27	5.64E-25	51.239
B	Syp	-3.311	8.947	-11.29	5.23E-27	1.37E-24	50.167
B	hid	-1.125	5.845	-11.02	6.22E-26	1.54E-23	48.014
C	Eip93F	-1.964	6.770	-19.47	2.96E-66	5.98E-63	139.759
C	hid	-1.033	5.845	-16.95	3.03E-53	3.41E-50	110.219
C	Imp	2.110	8.358	15.11	3.72E-44	2.72E-41	89.150
C	CG13298	1.355	10.597	13.40	3.68E-36	1.75E-33	71.248
C	Dll	-0.514	5.611	-12.72	4.34E-33	1.78E-30	64.279
C	Tctp	0.835	10.615	12.28	3.62E-31	1.37E-28	59.915
C	Inx2	-0.795	5.982	-12.05	3.50E-30	1.21E-27	57.729
C	CG4577	1.820	7.331	11.96	8.66E-30	2.83E-27	56.677
C	bru-3	2.159	9.067	11.88	1.85E-29	5.98E-27	55.983
C	CG14186	1.474	7.537	11.58	3.37E-28	9.58E-26	53.039
D	fne	2.186	11.081	17.07	7.75E-54	9.15E-51	111.293
D	pros	4.251	9.487	16.44	1.13E-50	1.07E-47	104.049
D	hid	-1.010	5.845	-15.95	3.16E-48	2.73E-45	98.743
D	Dll	-0.633	5.611	-15.73	3.70E-47	3.04E-44	96.412

D	jim	1.929	10.896	15.58	2.07E-46	1.67E-43	94.521
D	Lin29	2.106	6.211	13.83	4.36E-38	2.32E-35	75.352
D	Hr38	-1.283	7.042	-13.23	2.17E-35	9.79E-33	69.564
D	ftz-f1	-0.609	6.063	-13.14	6.06E-35	2.69E-32	68.547
D	sr	-1.438	7.376	-12.03	4.00E-30	1.36E-27	57.524
D	kn	-0.938	6.013	-12.00	5.80E-30	1.95E-27	57.209
E	Hs3st-A	-1.314	6.568	-12.22	6.65E-31	2.44E-28	59.350
E	Hr38	-1.575	7.042	-11.94	9.82E-30	3.19E-27	56.700
E	fkh	-1.525	6.501	-10.64	2.10E-24	4.61E-22	44.628
E	TM4SF	-1.290	7.011	-10.46	1.05E-23	2.16E-21	43.024
E	ftz-f1	-0.720	6.063	-10.21	1.01E-22	1.89E-20	40.806
E	CG42540	-0.994	6.454	-9.94	1.04E-21	1.75E-19	38.528
E	ps	-1.319	7.072	-9.90	1.46E-21	2.45E-19	38.204
E	Gycalpha99B	-0.949	6.511	-9.84	2.46E-21	4.09E-19	37.683
E	CG42817	-0.906	6.220	-9.31	2.22E-19	3.07E-17	33.258
E	acj6	-1.550	6.465	-9.21	5.16E-19	6.85E-17	32.464
F	beat-IIa	3.604	6.894	14.75	2.13E-42	1.43E-39	85.009
F	NetA	2.279	5.626	12.67	6.85E-33	2.78E-30	63.317
F	beat-Ic	3.393	6.908	12.59	1.63E-32	6.46E-30	62.732
F	CG4467	-1.264	6.708	-11.97	7.85E-30	2.58E-27	56.917
F	ps	-1.368	7.072	-11.75	6.61E-29	2.04E-26	54.804
F	TM4SF	-1.261	7.011	-11.46	1.05E-27	2.91E-25	52.088
F	ftz-f1	-0.714	6.063	-11.37	2.36E-27	6.32E-25	51.180
F	Dll	-0.659	5.611	-11.14	2.17E-26	5.49E-24	48.977
F	Hr38	-1.416	7.042	-10.93	1.50E-25	3.66E-23	47.157
F	Fas3	2.653	6.539	10.88	2.44E-25	5.83E-23	46.557
G	kn	4.438	6.013	21.83	8.19E-79	2.48E-75	166.879
G	fkh	3.773	6.501	15.06	6.89E-44	4.98E-41	88.314
G	jeb	-3.261	8.853	-14.27	3.63E-40	2.31E-37	80.096
G	CG10186	-1.236	6.619	-14.07	3.15E-39	1.90E-36	78.296
G	dpr8	-1.482	6.580	-14.01	5.96E-39	3.52E-36	77.684
G	acj6	3.390	6.465	13.87	2.62E-38	1.44E-35	75.719
G	fne	2.553	11.081	13.51	1.20E-36	5.84E-34	72.365
G	CG42541	-1.627	6.788	-13.50	1.32E-36	6.37E-34	72.342
G	bi	3.778	6.889	13.32	8.68E-36	4.00E-33	70.168
G	CG11000	-1.383	6.773	-13.08	1.03E-34	4.46E-32	68.030
H	Dll	3.842	5.611	25.98	3.00E-101	2.90E-97	217.267

H	hbn	5.624	5.910	23.84	1.28E-89	7.73E-86	192.409
H	Fas2	4.971	8.531	21.93	2.56E-79	8.24E-76	169.548
H	Mmp2	4.282	6.918	20.58	4.17E-72	1.06E-68	152.532
H	Ets65A	4.693	5.864	17.16	2.57E-54	3.27E-51	112.203
H	nAChRalpha5	-1.999	7.597	-17.05	9.37E-54	1.08E-50	111.488
H	aop	2.986	6.799	14.10	2.30E-39	1.41E-36	78.265
H	ps	-1.498	7.072	-13.85	3.48E-38	1.89E-35	75.877
H	CG14989	4.928	7.721	13.74	1.07E-37	5.48E-35	74.759
H	hid	2.361	5.845	12.43	8.14E-32	3.18E-29	61.103

Supplementary Table 4.4 Top 5 differentially expressed CAMs between pairwise comparisons of Type I MN populations

Contrast	Gene	Log fold-change	Average Expression	t	*p*-value	Adjusted *p*-value	B
A-D	dpr8	0.853	6.580	5.86	7.49E-09	1.99E-07	9.26
A-D	Nrg	-0.767	8.819	-5.80	1.06E-08	2.70E-07	8.96
A-D	dpr14	0.929	7.569	5.59	3.33E-08	7.62E-07	7.89
A-D	CadN	-0.682	8.387	-5.40	9.72E-08	1.99E-06	6.84
A-D	Fas2	-1.253	8.531	-5.30	1.60E-07	3.10E-06	6.35
A-E	dpr18	0.953	5.834	7.02	5.92E-12	2.83E-10	16.18
A-E	dpr14	1.800	7.569	6.29	5.94E-10	2.00E-08	12.14
A-E	Lar	1.646	8.470	5.78	1.16E-08	2.94E-07	9.30
A-E	dpr8	1.098	6.580	5.60	3.29E-08	7.53E-07	8.02
A-E	CG42313	1.207	6.692	5.36	1.18E-07	2.36E-06	6.78
A-F	CadN	-1.223	8.387	-6.61	8.49E-11	3.33E-09	13.87
A-F	CG34113	-1.509	6.439	-6.19	1.12E-09	3.57E-08	11.41
A-F	CG34114	-1.389	6.280	-5.96	4.17E-09	1.17E-07	10.13
A-F	lea	-1.540	6.287	-5.51	5.20E-08	1.14E-06	7.69
A-F	Con	1.189	6.631	5.32	1.43E-07	2.82E-06	6.45
A-G	beat-Ic	1.493	6.908	6.96	8.89E-12	4.12E-10	15.75
A-G	dpr14	1.705	7.569	6.85	1.73E-11	7.70E-10	15.43
A-G	CG34113	0.820	6.439	5.29	1.66E-07	3.21E-06	6.18
A-G	dpr15	0.390	5.492	5.13	3.88E-07	6.82E-06	4.85
A-H	dpr18	0.963	5.834	7.14	2.62E-12	1.34E-10	16.81
A-H	rst	-1.727	5.949	-6.78	2.76E-11	1.18E-09	14.96
A-H	beat-VII	1.291	6.403	6.37	3.62E-10	1.26E-08	12.20
A-H	dpr17	1.275	6.340	6.35	4.28E-10	1.48E-08	11.91
A-H	beat-Va	0.752	6.010	5.83	9.15E-09	2.37E-07	8.68
B-D	Nrk	-1.233	6.573	-6.00	3.40E-09	9.72E-08	10.43
C-D	dpr15	0.288	5.492	5.60	3.17E-08	7.28E-07	7.61
C-D	dpr13	0.920	6.630	5.52	5.11E-08	1.12E-06	7.83
C-D	klg	1.116	7.424	5.49	6.02E-08	1.30E-06	7.73
C-D	Dg	-0.858	7.420	-5.41	9.11E-08	1.88E-06	7.33
C-D	dpr18	0.425	5.834	5.11	4.36E-07	7.57E-06	5.44
E-B	Dscam2	2.507	7.941	6.27	6.73E-10	2.23E-08	12.13
E-C	beat-VII	-1.584	6.403	-9.34	1.69E-19	2.26E-17	33.55
E-C	Dscam2	1.547	7.941	5.70	1.90E-08	4.60E-07	8.99

E-C	CG42313	-1.224	6.692	-5.67	2.21E-08	5.27E-07	8.73
E-D	Dscam2	1.469	7.941	5.41	9.20E-08	1.90E-06	7.51
F-B	beat-IIa	2.800	6.894	6.13	1.59E-09	4.89E-08	11.29
F-B	Nrg	1.771	8.819	5.84	8.34E-09	2.19E-07	9.70
F-B	dpr8	2.062	6.580	5.84	8.42E-09	2.20E-07	9.70
F-B	beat-Ib	1.895	6.170	5.81	1.01E-08	2.59E-07	9.43
F-B	CadN	1.675	8.387	5.72	1.62E-08	3.98E-07	9.08
F-C	Fas2	1.702	8.531	5.39	9.93E-08	2.03E-06	7.27
F-C	beat-Ib	1.403	6.170	5.37	1.12E-07	2.25E-06	7.24
F-C	lea	1.429	6.287	5.20	2.74E-07	5.02E-06	6.38
F-C	dpr14	-1.263	7.569	-5.17	3.11E-07	5.62E-06	6.25
F-C	beat-Va	-0.659	6.010	-5.10	4.45E-07	7.72E-06	5.44
F-D	klg	2.011	7.424	6.49	1.80E-10	6.62E-09	13.41
F-D	lea	1.700	6.287	6.24	7.92E-10	2.60E-08	11.99
F-D	CG34114	1.402	6.280	6.11	1.74E-09	5.29E-08	11.24
F-D	kirre	1.372	7.225	5.35	1.23E-07	2.46E-06	7.19
F-D	side	1.482	6.671	5.26	1.98E-07	3.77E-06	6.73
F-E	beat-IIb	1.840	5.984	6.11	1.74E-09	5.30E-08	11.26
F-E	klg	2.397	7.424	5.66	2.28E-08	5.42E-07	8.83
F-E	CG34113	1.752	6.439	5.62	2.95E-08	6.83E-07	8.58
F-E	beat-Ib	1.695	6.170	5.24	2.25E-07	4.21E-06	6.66
F-E	Dscam3	1.215	5.755	5.06	5.57E-07	9.39E-06	5.72
F-H	beat-Ic	3.303	6.908	8.02	5.41E-15	4.13E-13	23.44
F-H	beat-IV	-2.428	6.088	-7.55	1.61E-13	9.86E-12	20.16
F-H	beat-IIb	2.107	5.984	7.53	1.76E-13	1.07E-11	20.08
F-H	beat-Ib	1.843	6.170	6.09	1.92E-09	5.80E-08	11.11
F-H	lea	1.785	6.287	5.34	1.30E-07	2.58E-06	7.11
G-B	Dscam2	2.684	7.941	7.21	1.60E-12	8.43E-11	17.94
G-B	side	-2.064	6.671	-5.42	8.60E-08	1.79E-06	7.42
G-B	Nrg	1.612	8.819	5.33	1.37E-07	2.71E-06	7.03
G-C	Nrg	1.066	8.819	5.88	6.52E-09	1.75E-07	9.88
G-C	beat-VII	-1.216	6.403	-5.80	1.08E-08	2.76E-07	9.35
G-C	beat-Ib	-0.778	6.170	-5.76	1.30E-08	3.25E-07	8.83
G-C	dpr15	-0.399	5.492	-5.65	2.44E-08	5.76E-07	7.88
G-C	dpr18	-0.549	5.834	-5.38	1.04E-07	2.11E-06	6.73
G-D	beat-Ic	-1.533	6.908	-7.56	1.41E-13	8.72E-12	20.22
G-D	Dscam2	1.647	7.941	7.18	1.95E-12	1.01E-10	17.76

G-D	Con	1.846	6.631	6.35	4.16E-10	1.44E-08	12.62
G-D	Dg	-1.375	7.420	-5.51	5.33E-08	1.16E-06	8.01
G-D	dpr8	-0.639	6.580	-5.50	5.42E-08	1.18E-06	7.59
G-E	Con	2.070	6.631	6.02	3.02E-09	8.75E-08	10.72
G-F	side	-1.951	6.671	-6.82	2.17E-11	9.45E-10	15.39
G-F	rst	-1.761	5.949	-6.64	6.85E-11	2.73E-09	14.32
G-F	CG34114	-1.517	6.280	-5.63	2.72E-08	6.35E-07	8.60
G-F	beat-Va	1.329	6.010	5.55	4.21E-08	9.41E-07	8.08
G-F	Dscam3	-1.241	5.755	-5.37	1.11E-07	2.24E-06	7.16
G-H	Con	2.504	6.631	8.49	1.55E-16	1.46E-14	26.84
G-H	beat-Va	1.456	6.010	6.21	9.84E-10	3.18E-08	11.55
G-H	Lar	-1.866	8.470	-6.18	1.14E-09	3.61E-08	11.58
G-H	rst	-1.597	5.949	-5.53	4.83E-08	1.07E-06	7.96
G-H	CadN	-1.226	8.387	-5.18	3.07E-07	5.57E-06	6.19

References

Aberle, H., Haghighi, A.P., Fetter, R.D., McCabe, B.D., Magalhães, T.R., and Goodman, C.S. (2002). wishful thinking encodes a BMP type II receptor that regulates synaptic growth in Drosophila. Neuron *33*, 545–558.

Allen, A.M., Neville, M.C., Birtles, S., Croset, V., Treiber, C.D., Waddell, S., and Goodwin, S.F. (2019). A single-cell transcriptomic atlas of the adult Drosophila ventral nerve cord.

Apitz, H., and Salecker, I. (2016). Retinal determination genes coordinate neuroepithelial specification and neurogenesis modes in the Drosophila optic lobe. Development *143*, 2431–2442.

Arzan Zarin, A., and Labrador, J.-P. (2019). Motor axon guidance in Drosophila. Semin. Cell Dev. Biol. *85*, 36–47.

Ashraf, S.I., and Ip, Y.T. (2001). The Snail protein family regulates neuroblast expression of inscuteable and string, genes involved in asymmetry and cell division in Drosophila. Development *128*, 4757–4767.

Atwood, H.L., and Klose, M.K. (2009). Comparative biology of invertebrate neuromuscular junctions.

Berger, C., Harzer, H., Burkard, T.R., Steinmann, J., van der Horst, S., Laurenson, A.-S., Novatchkova, M., Reichert, H., and Knoblich, J.A. (2012). FACS purification and transcriptome analysis of drosophila neural stem cells reveals a role for Klumpfuss in self-renewal. Cell Rep. *2*, 407–418.

Bieber, A.J., Snow, P.M., Hortsch, M., Patel, N.H., Jacobs, J.R., Traquina, Z.R., Schilling, J., and Goodman, C.S. (1989). Drosophila neuroglian: a member of the immunoglobulin superfamily with extensive homology to the vertebrate neural adhesion molecule L1. Cell *59*, 447–460.

Birkholz, O., Rickert, C., Nowak, J., Coban, I.C., and Technau, G.M. (2015). Bridging the gap between postembryonic cell lineages and identified embryonic neuroblasts in the ventral nerve cord of Drosophila melanogaster. Biol. Open *4*, 420–434.

Broadus, J., Skeath, J.B., Spana, E.P., Bossing, T., Technau, G., and Doe, C.Q. (1995). New neuroblast markers and the origin of the aCC/pCC neurons in the Drosophila central nervous system. Mech. Dev. *53*, 393–402.

Brunet Avalos, C., Maier, G.L., Bruggmann, R., and Sprecher, S.G. (2019). Single cell transcriptome atlas of the Drosophila larval brain. Elife *8*.

Cai, Y., Chia, W., and Yang, X. (2001). A family of snail-related zinc finger proteins regulates two distinct and parallel mechanisms that mediate Drosophila neuroblast asymmetric divisions.

EMBO J. *20*, 1704–1714.

Carrillo, R.A., Özkan, E., Menon, K.P., Nagarkar-Jaiswal, S., Lee, P.-T., Jeon, M., Birnbaum, M.E., Bellen, H.J., Garcia, K.C., and Zinn, K. (2015). Control of Synaptic Connectivity by a Network of Drosophila IgSF Cell Surface Proteins. Cell *163*, 1770–1782.

Caussinus, E., Colombelli, J., and Affolter, M. (2008). Tip-cell migration controls stalk-cell intercalation during Drosophila tracheal tube elongation. Curr. Biol. *18*, 1727–1734.

Certel, S.J., and Thor, S. (2004). Specification of Drosophila motoneuron identity by the combinatorial action of POU and LIM-HD factors. Development *131*, 5429–5439.

Chen, X., Rahman, R., Guo, F., and Rosbash, M. (2016). Genome-wide identification of neuronal activity-regulated genes in Drosophila. Elife *5*.

Choi, J.C., Park, D., and Griffith, L.C. (2004). Electrophysiological and morphological characterization of identified motor neurons in the Drosophila third instar larva central nervous system. J. Neurophysiol. *91*, 2353–2365.

Chouinard, S.W., Wilson, G.F., Schlimgen, A.K., and Ganetzky, B. (1995). A potassium channel beta subunit related to the aldo-keto reductase superfamily is encoded by the Drosophila hyperkinetic locus. Proc. Natl. Acad. Sci. U. S. A. *92*, 6763–6767.

Chung, N.C., and Storey, J.D. (2015). Statistical significance of variables driving systematic variation in high-dimensional data. Bioinformatics *31*, 545–554.

Cole, M.B., Risso, D., Wagner, A., DeTomaso, D., Ngai, J., Purdom, E., Dudoit, S., and Yosef, N. (2019). Performance Assessment and Selection of Normalization Procedures for Single-Cell RNA-Seq. Cell Syst *8*, 315–328.e8.

Covarrubias, M., Wei, A.A., and Salkoff, L. (1991). Shaker, Shal, Shab, and Shaw express independent K+ current systems. Neuron *7*, 763–773.

Davie, K., Janssens, J., Koldere, D., De Waegeneer, M., Pech, U., Kreft, Ł., Aibar, S., Makhzami, S., Christiaens, V., Bravo González-Blas, C., et al. (2018). A Single-Cell Transcriptome Atlas of the Aging Drosophila Brain. Cell *174*, 982–998.e20.

DiAntonio, A., Burgess, R.W., Chin, A.C., Deitcher, D.L., Scheller, R.H., and Schwarz, T.L. (1993). Identification and characterization of Drosophila genes for synaptic vesicle proteins. J. Neurosci. *13*, 4924–4935.

Dillard, C., Narbonne-Reveau, K., Foppolo, S., Lanet, E., and Maurange, C. (2018). Two distinct mechanisms silence chinmo in Drosophila neuroblasts and neuroepithelial cells to limit their self-renewal. Development *145*.

Elkins, T., and Ganetzky, B. (1988). The roles of potassium currents in Drosophila flight

muscles. J. Neurosci. *8*, 428–434.

Elkins, T., Ganetzky, B., and Wu, C.F. (1986). A Drosophila mutation that eliminates a calcium-dependent potassium current. Proc. Natl. Acad. Sci. U. S. A. *83*, 8415–8419.

Fujioka, M., Lear, B.C., Landgraf, M., Yusibova, G.L., Zhou, J., Riley, K.M., Patel, N.H., and Jaynes, J.B. (2003). Even-skipped, acting as a repressor, regulates axonal projections in Drosophila. Development *130*, 5385–5400.

Garces, A., and Thor, S. (2006). Specification of Drosophila aCC motoneuron identity by a genetic cascade involving even-skipped, grain and zfh1. Development *133*, 1445–1455.

Goodman, C.S. (1996). Mechanisms and molecules that control growth cone guidance. Annu. Rev. Neurosci. *19*, 341–377.

Guan, Z., Saraswati, S., Adolfsen, B., and Littleton, J.T. (2005). Genome-wide transcriptional changes associated with enhanced activity in the Drosophila nervous system. Neuron *48*, 91–107.

Halpern, M.E., Chiba, A., Johansen, J., and Keshishian, H. (1991). Growth cone behavior underlying the development of stereotypic synaptic connections in Drosophila embryos. J. Neurosci. *11*, 3227–3238.

Homem, C.C.F., and Knoblich, J.A. (2012). Drosophila neuroblasts: a model for stem cell biology. Development *139*, 4297–4310.

Jacobs, K., Todman, M.G., Allen, M.J., Davies, J.A., and Bacon, J.P. (2000). Synaptogenesis in the giant-fibre system of Drosophila: interaction of the giant fibre and its major motorneuronal target. Development *127*, 5203–5212.

Jan, L.Y., and Jan, Y.N. (1976). L-glutamate as an excitatory transmitter at the Drosophila larval neuromuscular junction. J. Physiol. *262*, 215–236.

Johansen, J., Halpern, M.E., Johansen, K.M., and Keshishian, H. (1989). Stereotypic morphology of glutamatergic synapses on identified muscle cells of Drosophila larvae. J. Neurosci. *9*, 710–725.

Kim, B., Shortridge, R.D., Seong, C., Oh, Y., Baek, K., and Yoon, J. (1998). Molecular characterization of a novel Drosophila gene which is expressed in the central nervous system. Mol. Cells *8*, 750–757.

Komiyama, T., Johnson, W.A., Luo, L., and Jefferis, G.S.X.E. (2003). From lineage to wiring specificity. POU domain transcription factors control precise connections of Drosophila olfactory projection neurons. Cell *112*, 157–167.

Kulik, Y., Jones, R., Moughamian, A.J., Whippen, J., and Davis, G.W. (2019). Dual separable

feedback systems govern firing rate homeostasis. Elife *8*.

Lacin, H., and Truman, J.W. (2016). Lineage mapping identifies molecular and architectural similarities between the larval and adult Drosophila central nervous system. Elife *5*, e13399.

Lai, S.-L., Miller, M.R., Robinson, K.J., and Doe, C.Q. (2012). The Snail family member Worniu is continuously required in neuroblasts to prevent Elav-induced premature differentiation. Dev. Cell *23*, 849–857.

Landgraf, M., Roy, S., Prokop, A., VijayRaghavan, K., and Bate, M. (1999). even-skipped determines the dorsal growth of motor axons in Drosophila. Neuron *22*, 43–52.

Li, H., Watson, A., Olechwier, A., Anaya, M., Sorooshyari, S.K., Harnett, D.P., Lee, H.-K.P., Vielmetter, J., Fares, M.A., Garcia, K.C., et al. (2017). Deconstruction of the beaten Path-Sidestep interaction network provides insights into neuromuscular system development. Elife *6*.

Li, X., Xie, Y., and Zhu, S. (2016). Notch maintains Drosophila type II neuroblasts by suppressing expression of the Fez transcription factor Earmuff. Development *143*, 2511–2521.

Lin, D.M., and Goodman, C.S. (1994). Ectopic and increased expression of Fasciclin II alters motoneuron growth cone guidance. Neuron *13*, 507–523.

Lin, W.-H., Wright, D.E., Muraro, N.I., and Baines, R.A. (2009). Alternative splicing in the voltage-gated sodium channel DmNav regulates activation, inactivation, and persistent current. J. Neurophysiol. *102*, 1994–2006.

Lin, W.-H., He, M., and Baines, R.A. (2015). Seizure suppression through manipulating splicing of a voltage-gated sodium channel. Brain *138*, 891–901.

Liu, Z., Yang, C.-P., Sugino, K., Fu, C.-C., Liu, L.-Y., Yao, X., Lee, L.P., and Lee, T. (2015). Opposing intrinsic temporal gradients guide neural stem cell production of varied neuronal fates. Science *350*, 317–320.

Lnenicka, G.A., and Keshishian, H. (2000). Identified motor terminals in Drosophila larvae show distinct differences in morphology and physiology. J. Neurobiol. *43*, 186–197.

Lun, A.T.L., Bach, K., and Marioni, J.C. (2016). Pooling across cells to normalize single-cell RNA sequencing data with many zero counts. Genome Biol. *17*, 75.

McCarthy, D.J., Campbell, K.R., Lun, A.T.L., and Wills, Q.F. (2017). Scater: pre-processing, quality control, normalization and visualization of single-cell RNA-seq data in R. Bioinformatics *33*, 1179–1186.

Melom, J.E., Akbergenova, Y., Gavornik, J.P., and Littleton, J.T. (2013). Spontaneous and evoked release are independently regulated at individual active zones. J. Neurosci. *33*,

17253–17263.

Meng, J.L., Marshall, Z.D., Lobb-Rabe, M., and Heckscher, E.S. (2019). How prolonged expression of Hunchback, a temporal transcription factor, re-wires locomotor circuits. Elife *8*.

Meng, J.L., Wang, Y., Carrillo, R.A., and Heckscher, E. (2020). Temporal transcription factors determine circuit membership by permanently altering motor neuron-to-muscle synaptic partnerships. Elife *9*.

Mitchell, K.J., Doyle, J.L., Serafini, T., Kennedy, T.E., Tessier-Lavigne, M., Goodman, C.S., and Dickson, B.J. (1996). Genetic analysis of Netrin genes in Drosophila: Netrins guide CNS commissural axons and peripheral motor axons. Neuron *17*, 203–215.

Monastirioti, M., Giagtzoglou, N., Koumbanakis, K.A., Zacharioudaki, E., Deligiannaki, M., Wech, I., Almeida, M., Preiss, A., Bray, S., and Delidakis, C. (2010). Drosophila Hey is a target of Notch in asymmetric divisions during embryonic and larval neurogenesis. Development *137*, 191–201.

Newman, Z.L., Hoagland, A., Aghi, K., Worden, K., Levy, S.L., Son, J.H., Lee, L.P., and Isacoff, E.Y. (2017). Input-Specific Plasticity and Homeostasis at the Drosophila Larval Neuromuscular Junction. Neuron *93*, 1388–1404.e10.

Nishino, J., Kim, S., Zhu, Y., Zhu, H., and Morrison, S.J. (2013). A network of heterochronic genes including Imp1 regulates temporal changes in stem cell properties. Elife *2*, e00924.

Nose, A., Mahajan, V.B., and Goodman, C.S. (1992). Connectin: a homophilic cell adhesion molecule expressed on a subset of muscles and the motoneurons that innervate them in Drosophila. Cell *70*, 553–567.

Özkan, E., Carrillo, R.A., Eastman, C.L., Weiszmann, R., Waghray, D., Johnson, K.G., Zinn, K., Celniker, S.E., and Garcia, K.C. (2013). An extracellular interactome of immunoglobulin and LRR proteins reveals receptor-ligand networks. Cell *154*, 228–239.

Packard, M., Jokhi, V., Ding, B., Ruiz-Cañada, C., Ashley, J., and Budnik, V. (2015). Nucleus to Synapse Nesprin1 Railroad Tracks Direct Synapse Maturation through RNA Localization. Neuron *86*, 1015–1028.

Parrish, J.Z., Kim, C.C., Tang, L., Bergquist, S., Wang, T., Derisi, J.L., Jan, L.Y., Jan, Y.N., and Davis, G.W. (2014). Krüppel mediates the selective rebalancing of ion channel expression. Neuron *82*, 537–544.

Pavlidis, P., and Tanouye, M.A. (1995). Seizures and failures in the giant fiber pathway of Drosophila bang-sensitive paralytic mutants. J. Neurosci. *15*, 5810–5819.

Peled, E.S., and Isacoff, E.Y. (2011). Optical quantal analysis of synaptic transmission in wild-type and rab3-mutant Drosophila motor axons. Nat. Neurosci. *14*, 519–526.

Peng, I.-F., and Wu, C.-F. (2007). Differential contributions of Shaker and Shab K+ currents to neuronal firing patterns in Drosophila. J. Neurophysiol. *97*, 780–794.

Pérez-Gómez, R., Slováková, J., Rives-Quinto, N., Krejci, A., and Carmena, A. (2013). A Serrate-Notch-Canoe complex mediates essential interactions between glia and neuroepithelial cells during Drosophila optic lobe development. J. Cell Sci. *126*, 4873–4884.

Pérez-Moreno, J.J., and O'Kane, C.J. (2019). GAL4 Drivers Specific for Type Ib and Type Is Motor Neurons in Drosophila. G3 *9*, 453–462.

Pipes, G.C., Lin, Q., Riley, S.E., and Goodman, C.S. (2001). The Beat generation: a multigene family encoding IgSF proteins related to the Beat axon guidance molecule in Drosophila. Development *128*, 4545–4552.

Ren, Q., Yang, C.-P., Liu, Z., Sugino, K., Mok, K., He, Y., Ito, M., Nern, A., Otsuna, H., and Lee, T. (2017). Stem Cell-Intrinsic, Seven-up-Triggered Temporal Factor Gradients Diversify Intermediate Neural Progenitors. Curr. Biol. *27*, 1303–1313.

Risso, D., Ngai, J., Speed, T.P., and Dudoit, S. (2014). Normalization of RNA-seq data using factor analysis of control genes or samples. Nat. Biotechnol. *32*, 896–902.

Risso, D., Purvis, L., Fletcher, R.B., Das, D., Ngai, J., Dudoit, S., and Purdom, E. (2018). clusterExperiment and RSEC: A Bioconductor package and framework for clustering of single-cell and other large gene expression datasets. PLoS Comput. Biol. *14*, e1006378.

Robinow, S., Campos, A.R., Yao, K.M., and White, K. (1988). The elav gene product of Drosophila, required in neurons, has three RNP consensus motifs. Science *242*, 1570–1572.

Rossi, A.M., and Desplan, C. (2020). Extrinsic Activin signaling cooperates with an intrinsic temporal program to increase mushroom body neuronal diversity.

Ruiz‐Cañada, C., and Budnik, V. (2006). Introduction on The Use of The Drosophila Embryonic/Larval Neuromuscular Junction as A Model System to Study Synapse Development and Function, and A Brief Summary of Pathfinding and Target Recognition. In International Review of Neurobiology, (Academic Press), pp. 1–31.

Samson, M.-L., and Chalvet, F. (2003). found in neurons, a third member of the Drosophila elav gene family, encodes a neuronal protein and interacts with elav. Mech. Dev. *120*, 373–383.

Sánchez-Soriano, N., and Prokop, A. (2005). The influence of pioneer neurons on a growing motor nerve in Drosophila requires the neural cell adhesion molecule homolog FasciclinII. J. Neurosci. *25*, 78–87.

Sanyal, S. (2009). Genomic mapping and expression patterns of C380, OK6 and D42 enhancer trap lines in the larval nervous system of Drosophila. Gene Expr. Patterns *9*, 371–380.

Schmid, A., Chiba, A., and Doe, C.Q. (1999). Clonal analysis of Drosophila embryonic

neuroblasts: neural cell types, axon projections and muscle targets. Development *126*, 4653–4689.

Schwarz, T.L., Tempel, B.L., Papazian, D.M., Jan, Y.N., and Jan, L.Y. (1988). Multiple potassium-channel components are produced by alternative splicing at the Shaker locus in Drosophila. Nature *331*, 137–142.

Scott, K., Brady, R., Jr, Cravchik, A., Morozov, P., Rzhetsky, A., Zuker, C., and Axel, R. (2001). A chemosensory gene family encoding candidate gustatory and olfactory receptors in Drosophila. Cell *104*, 661–673.

Seeger, M., Tear, G., Ferres-Marco, D., and Goodman, C.S. (1993). Mutations affecting growth cone guidance in Drosophila: genes necessary for guidance toward or away from the midline. Neuron *10*, 409–426.

Syed, M.H., Mark, B., and Doe, C.Q. (2017). Steroid hormone induction of temporal gene expression in Drosophila brain neuroblasts generates neuronal and glial diversity. Elife *6*.

Takizawa, E., Komatsu, A., and Tsujimura, H. (2007). Identification of common excitatory motoneurons in Drosophila melanogaster larvae. Zoolog. Sci. *24*, 504–513.

Tan, L., Zhang, K.X., Pecot, M.Y., Nagarkar-Jaiswal, S., Lee, P.-T., Takemura, S.-Y., McEwen, J.M., Nern, A., Xu, S., Tadros, W., et al. (2015). Ig Superfamily Ligand and Receptor Pairs Expressed in Synaptic Partners in Drosophila. Cell *163*, 1756–1769.

Thor, S., Andersson, S.G., Tomlinson, A., and Thomas, J.B. (1999). A LIM-homeodomain combinatorial code for motor-neuron pathway selection. Nature *397*, 76–80.

Toledano, H., D'Alterio, C., Czech, B., Levine, E., and Jones, D.L. (2012). The let-7-Imp axis regulates ageing of the Drosophila testis stem-cell niche. Nature *485*, 605–610.

Tsunoda, S., and Salkoff, L. (1995). The major delayed rectifier in both Drosophila neurons and muscle is encoded by Shab. J. Neurosci. *15*, 5209–5221.

Wickham, H. (2010). ggplot2: Elegant Graphics for Data Analysis (Use R!) (Springer).

Winberg, M.L., Mitchell, K.J., and Goodman, C.S. (1998). Genetic analysis of the mechanisms controlling target selection: complementary and combinatorial functions of netrins, semaphorins, and IgCAMs. Cell *93*, 581–591.

Wolfram, V., Southall, T.D., Brand, A.H., and Baines, R.A. (2012). The LIM-homeodomain protein islet dictates motor neuron electrical properties by regulating K(+) channel expression. Neuron *75*, 663–674.

Wolfram, V., Southall, T.D., Günay, C., Prinz, A.A., Brand, A.H., and Baines, R.A. (2014). The transcription factors islet and Lim3 combinatorially regulate ion channel gene expression. J.

Neurosci. *34*, 2538–2543.

Wreden, C.C., Meng, J.L., Feng, W., Chi, W., Marshall, Z.D., and Heckscher, E.S. (2017). Temporal Cohorts of Lineage-Related Neurons Perform Analogous Functions in Distinct Sensorimotor Circuits. Curr. Biol. *27*, 1521–1528.e4.

Xiao, Q., Komori, H., and Lee, C.-Y. (2012). klumpfuss distinguishes stem cells from progenitor cells during asymmetric neuroblast division. Development *139*, 2670–2680.

Yang, C.-P., Samuels, T.J., Huang, Y., Yang, L., Ish-Horowicz, D., Davis, I., and Lee, T. (2017). Imp and Syp RNA-binding proteins govern decommissioning of Drosophila neural stem cells. Development *144*, 3454–3464.

Yu, H.H., Araj, H.H., Ralls, S.A., and Kolodkin, A.L. (1998). The transmembrane Semaphorin Sema I is required in Drosophila for embryonic motor and CNS axon guidance. Neuron *20*, 207–220.

Zacharioudaki, E., Magadi, S.S., and Delidakis, C. (2012). bHLH-O proteins are crucial for Drosophila neuroblast self-renewal and mediate Notch-induced overproliferation. Development *139*, 1258–1269.

Zarin, A.A., Asadzadeh, J., Hokamp, K., McCartney, D., Yang, L., Bashaw, G.J., and Labrador, J.-P. (2014). A transcription factor network coordinates attraction, repulsion, and adhesion combinatorially to control motor axon pathway selection. Neuron *81*, 1297–1311.

Appendix 1:
Identification of housekeeping genes in *Drosophila melanogaster* tissues for the normalization of RNA-sequencing data sets

Abstract

Normalization is an important step in the RNA-sequencing data analysis pipeline for accurate determination of gene expression levels and for making comparisons between biological conditions of interest. Two popular approaches for normalizing RNA-seq rely on using External RNA Control Consortium (ERCC) spike-in controls or the use of housekeeping genes, whose expression should be consistent between samples. Selection of housekeeping genes can vary depending on tissue type or experimental condition. Here, we present a method for identifying housekeeping genes from unembargoed RNA-seq libraries from the modENCODE project and measure their performance in correcting complex, unwanted technical effects. Housekeeping genes identified from these independent data sets perform similarly to housekeeping genes modeled *in silico* for correcting technical effects, but are more stable in controlling type I error in differential expression (DE) inference.

Background

RNA-seq experiments rely on accurate quantification of and normalization so that differences in gene expression reflect relevant differences in the biological origin of the sample (Bullard et al., 2010; Dillies et al., 2013; Risso et al., 2011). Many normalization methods have been developed to reduce experimental noise by correcting for global variation between RNA-seq samples as well as gene-specific variation (Anders and Huber, 2010; Bullard et al., 2010; Li et al., 2012; Robinson and Oshlack, 2010). Sequencing depth, gene length, and GC content are well-documented sources of such variation (Bullard et al., 2010; Hansen et al., 2012; Risso et al., 2011; Robinson and Oshlack, 2010). However, RNA-seq experiments with complicated preparations (e.g. cell sorting, laser capture microdissection) or unbalanced batches may need more correction beyond what can be accounted for by sequencing depth. Techniques such as removal of unwanted variation (RUV) adjust these nuisance technical effects using negative control genes (RUVg), negative control samples (RUVs), or residuals of a first-pass GLM regression (RUVr).

Many normalization methods for RNA-seq data were adapted from those developed for microarray, including quantile normalization and RUV (Bolstad et al., 2003; Gagnon-Bartsch and Speed, 2012). External controls, such as synthetic spike-ins, were also originally developed for microarrays, and have been successfully ported for use in mRNA array and microRNA array experiments (Oshlack et al., 2007; Wu et al., 2013; Yang et al., 2002). Sets of spike-in standards have been developed by the External RNA Controls Consortium for use in RNA-seq experiments (Baker et al., 2005; Jiang et al., 2011), but with mixed results (Lovén et al., 2012; Mortazavi et al., 2008; Qing et al., 2013; Risso et al., 2014). Evidence suggests that the effectiveness of spike-in controls in RNA-seq is dependent on the mRNA selection protocol (e.g polyA+ or RiboZero), presumably due to the fact that ERCC spike-ins have a different structure than endogenous mRNAs (Grün and van Oudenaarden, 2015; Qing et al., 2013). However, in cases where a global change in gene expression is expected between biological conditions, spike-in controls may be the most appropriate external control.

On the other hand, the use of housekeeping genes in normalization rests on the assumption that the expression of housekeeping genes does not change between samples regardless of the biological covariate of interest. While such an assumption is valid for many experiments, care must be taken when selecting housekeeping genes for normalization, as the expression of some of commonly used housekeeping genes can change depending on cell type, cancer status, or metabolic state (Caradec et al., 2010; Gong et al., 2016; de Kok et al., 2005; Mahoney et al., 2004; Panina et al., 2018; Thellin et al., 1999).

Here we explore an evidence-based approach for identifying housekeeping genes in *Drosophila melanogaster* tissues for use in the normalization of RNA-seq data, similar to the approach taken by Wang et al. and Zhou et al. (Wang et al., 2019; Zhou et al., 2017). We employ these housekeeping genes in the RUVg framework and assess its effect on normalization and DE inference on a data set of sorted motor neurons from *Drosophila* larvae containing transgenes for knock-down of synaptic gene expression. We demonstrate that independently-identified housekeeping genes used with RUV provides a stable method for correcting technical variation in RNA-seq experiments and controlling type I error in DE testing.

Results

Selection and characterization of housekeeping genes from dissected *Drosophila* tissues

To identify genes that can serve as housekeeping genes in the 3rd instar *Drosophila* larva, we consider public RNA-seq data sets prepared from various dissected tissues at this developmental stage. Data sets from the modENCODE project (Boley et al., 2014; Celniker et al., 2009) are ideal for identifying housekeeping genes because they satisfy the following conditions: (i) have a large variety of tissues by embryological origin, (ii) use the same protocol for cDNA and library preparation, and (iii) use the same sequencing format. With these criteria we identified 16 RNA-seq libraries from 6 different larval tissues from the modENCODE project that are suitable for housekeeping gene selection (Supplementary Table 1, Figure 5.1A).

This strategy for identifying housekeeping genes operates on the assumption that gene expression differences between ensembles of cells from the same tissue are greater than those between cell types within the tissue. To that end we select genes that have the lowest variance between each data set by first removing genes with expression below 1 CPM in any sample and an average expression below 2^7 CPM (Figure 5.1A). We then select the 600 genes with lowest variance for the housekeeping gene set.

The housekeeping gene set contains canonical housekeeping genes used in microarray or qPCR normalization, including metabolic genes (e.g. *Gapdh1* and *Gapdh2*), cytoskeletal proteins (e.g. *αTub84B* and *Act5C*), ribosomal proteins (e.g. *RpS18*, *RpL32*, and *RpS20*), and other translational machinery (e.g. *eIF1FA* and *eEF1α1*) (Ling and Salvaterra, 2011; Ponton et al., 2011). To further characterize our housekeeping gene set we performed Gene Ontology enrichment analysis on the biological process (BP), molecular function (MF), and cellular component (CC) subontologies (Figure 5.1B-D). The terms with the greatest enrichment in each of the BP, MF, and CC categories pertain to the ribosome and translational machinery (Figure

5.1B-D). Other terms enriched across these categories include those pertaining to protein quality control and autophagy, cytoskeleton components, and cellular respiration (Figure 5.1B-D).

Evaluation of housekeeping genes in removing unwanted variation in RNA-seq data

To validate our independently-selected housekeeping genes as suitable negative controls for the removal of unwanted variation, we consider an RNA-sequencing data set derived from FACS-purified motor neurons from the 3rd *Drosophila* larval central nervous system representing different genetic models of altered synaptic physiology via RNA interference (see Methods). An ideal normalization method should reduce technical variation between samples and increase the sensitivity of differential expression. For this data set, standard methods do not lead to adequate normalization (Figure 5.2). Principal component (PC) analysis shows that unnormalized samples cluster poorly by biological condition (Figure 5.2A). While upper-quartile (UQ) normalization improves clustering by biological condition, PC2 reveals a batch effect between two groups of replicates of *OK6>empty(attP2*) libraries (Figure 5.2A'). Relative log expression (RLE) distributions of unnormalized libraries further demonstrate the need for normalization (Figure 5.2B). Libraries of unnormalized counts from each sample type have replicates with RLE distributions that are not centered around zero (Figure 5.2B). UQ normalization attenuates these deviations, albeit with a few outstanding samples (Figure 5.2B').

In contrast, RUVg with either housekeeping genes or empirical negative controls identified *in silico* correct for many of these unwanted technical effects. All 600 housekeeping genes selected from the modENCODE larval dissected tissue data set are expressed in the test data set of FACS-purified larval motor neurons. Libraries normalized with RUVg cluster by biological condition in PC space (Figure 5.2A''-A'''). RUVg normalization also corrects for deviations in RLE (Figure 5.2B''-B'''), with the RUVg routine with housekeeping genes offering the best correction for the outlying second *OK6>empty(attP40)* replicate.

The effectiveness of normalization can also be assessed by analyzing trends between the average expression of a gene with the difference in expression across two samples of the same biological condition. We expect that the difference in expression between two normalized libraries with no expected DE to be scattered about zero. Such mean-difference (MD) plots of unnormalized counts and UQ-normalized counts from two *OK6>empty(attP2)* libraries trend away from zero (Figure 5.3A-B). Genes with moderate or very high expression have overestimated differences in expression between the two libraries, and would likely be erroneously identified as being differentially expressed between the two samples. RUVg normalizations with housekeeping genes or *in silico* empirical controls correct this deviation, and have MD trends that are centered around zero (Figure 5.3C-D).

Effect of RUVg normalization with housekeeping genes on differential expression

To understand the impact of RUVg normalization with housekeeping genes on DE, we compared the distribution of *p*-values obtained from DE analysis of each normalization method. We performed DE testing with two popular DE testing methods, edgeR and DESeq2, on two batches of *OK6>empty(attP2)* libraries. Both edgeR and DESeq2 assume gene counts obey a negative

binomial distribution and control the false discovery of DE genes by implementing the Benjamini-Hochberg procedure (Love et al., 2014; Robinson et al., 2010). However, they differ in their calculation of gene-wise dispersion, estimation of expression fold change, and methods for calling a gene DE, which produces trade-offs in sensitivity and precision (Love et al., 2014; Robinson et al., 2010).

In the null experiment of comparing *OK6>empty(attP2)* replicates, no genes should be DE. To test the reliability of empirical control genes in normalization we used both the control genes identified from the full data set along with control genes calculated by comparing the *OK6>empty(attP2)* replicates by date of FACS sort. Ideal negative control genes, whether they are modeled *in silico* or identified from independent experiments, should be robust (e.g. in the null experiment technical variation between different batches of the reference condition should be similar to that of the full data set). We therefore expect successful normalization to remove technical variation between the two batches, and produce a uniform *p*-value distribution. We find that all normalization methods produced a rightward shift of the empirical cumulative distribution of *p*-values towards the theoretical distribution compared to unnormalized counts for both DE testing paradigms (Figure 5.4, Supplementary Figure 5.1). However, we also find that empirical control genes modeled *in silico* are sensitive to the comparison made, with the *OK6>empty(attP2)*-only control genes performing worse than either the housekeeping genes or empirical control genes identified from the full data set (Figure 5.4, Supplementary Figure 5.1).

Conclusions

Normalization and control of technical variation are essential steps in assessing biological covariates of interest in RNA-seq experiments, especially as sequencing technology is being used in large collaborative projects that span multiple research groups (e.g. The Cancer Genome Atlas, ENCODE, Atlas of Normal Tissue Expression), in translational research and diagnostics, and applied low-input samples and individual cells (Cancer Genome Atlas Research Network, 2008; ENCODE Project Consortium, 2004; Gonorazky et al., 2019; Hawrylycz et al., 2012; Suntsova et al., 2019). Such technical variation often cannot be fully explained by documented sources of variation, such as in differences in gene length, GC content or sequencing depth. Therefore, normalization methods that can model more complex effects are desirable. Previous work in this area has shown that RUV can correct for these effects using negative control genes or negative control samples (Risso et al., 2014).

Using RNA-seq data sets from the modENCODE project, we have identified a set of 600 housekeeping genes with high expression and low variance across 6 different tissue types in the *Drosophila* 3rd instar larva (Celniker et al., 2009). These 600 housekeeping genes are involved in core biological processes such as translation, metabolism, and cytoskeletal structure (Figure 5.1), and are in agreement with reference genes used for RT-qPCR experiments in Drosophila.

We have shown that using these housekeeping genes with RUV on a test data set of FACS-sorted motor neurons from larval *Drosophila* improves normalization compared to standard routines and performs similarly to RUVg with empirical controls modeled *in silico* (Figures 5.2-5.3). While RUVg with empirical controls identified across the entire data set best controlled type I

error in the null experiment comparing two groups of technical replicates of the reference condition (*OK6>empty(attP2)*), the effectiveness of empirical control genes is dependent on the comparison made in the first-pass DE test used to curate the genes (Figure 5.4). While RUVg with empirical controls performs well with a larger number of replicates and has a lower computational time investment, RUVg with housekeeping genes may have an advantage in analyzing RNA-seq experiments involving low-input samples where biological replicates must inevitably be pooled, imbalanced designs, or limited replicates.

Another potential strength of housekeeping genes is that one can expand this concept of identifying negative controls for cell type by comparing RNA-seq data sets derived from different tissues to negative controls for developmental stage. For example, if one wishes to normalize RNA-seq libraries from *Drosophila* CNS tissue at different developmental time points, one could make use of the modENCODE RNA-seq libraries derived from CNS tissue from larval, pupal and adult flies for determining a housekeeping gene set.

Controlling confounding effects is of even greater importance to single-cell RNA-sequencing experiments for two distinct reasons. Firstly, library preparation effects can be magnified by stochasticity of mRNA capture and reverse transcription on such a small amount of starting material. Heterogenous mixtures of cells subjected to identical library preparation protocols could still produce cDNA amplification bias and differences in sequencing depth dependent on cell type or cell size. While use of unique molecular identifiers in the mRNA capture step can ameliorate this somewhat, normalization will still be critical for correcting technical noise between cells. Secondly, since each sample corresponds to an individual cell, these experiments are performed in a single, discrete batch that cannot be repeated. RUV is suited to modeling technical variation in confounded RNA-seq experiments (Risso et al., 2014). Suitability of housekeeping genes for denoising single-cell RNA-sequencing data is readily testable, as RUV is already implemented in software packages aimed at finding ideal normalization parameters for single-cell data (Cole et al., 2019).

Methods

Identification of Housekeeping Genes

Negative control genes to aid with normalization were obtained by comparing the expression of genes from 3rd instar larval tissues. Sequence Read Archive accession numbers and sample descriptions are described in Supplementary Table 1 and the pertinent .fastq files were obtained with SRA Toolkit (ver 2.9.4.1, http://ncbi.github.io/sra-tools/) fastq-dump function. Read quality was examined with FastQC (ver 0.11.7, Andrews, 2010) and reads were trimmed with Trimmomatic (ver 0.38, Bolger et al., 2014). Reads were mapped to the Berkeley Drosophila Genome Project (dm6, release 95) genome assembly with HISAT2 (ver 2.1.0, (Kim et al., 2019).

featureCounts (ver 1.6.4, Liao et al., 2014) output was imported to R for biological analysis.To identify stably expressed genes across all samples and all tissues, genes with at least 1 CPM in 10 or more samples were considered undetectable and removed from the data set. Counts were normalized with the upper-quartile (UQ) normalization procedure described by Bullard et al

(Bullard et al., 2010). When selecting housekeeping genes, we prefer genes with high, stable expression across all samples. To that end genes with 1 CPM or fewer in any sample were removed from consideration. The remaining genes with high expression (average expression above 2^7 CPM) were ranked by increasing variance. The top 600 genes were selected as housekeeping genes.

Gene Ontology Enrichment Analysis

Housekeeping genes were characterized by testing for enriched Gene Ontology terms (Ashburner et al., 2000; The Gene Ontology Consortium, 2019) with the clusterProfiler implementation of the hypergeometric test (ver 3.10.1, Yu et al., 2012). The rate of false discovery controlled with a *q*-value cutoff of 0.01, and *p*-values were adjusted for multiple hypothesis testing with the Benjamini-Hochberg procedure. Redundant GO terms were reduced by analyzing semantic similarity with GOSemSim (Yu et al., 2010).

Low-input RNA-seq on purified motor neurons

Samples of the test data set are the same as those described in Chapters 2 and 3 from *Drosophila* larvae of the following genotypes:

UAS-Dcr2;OK6-Gal4/+;UAS-mCherry-NLS/(attP2) (abbr. OK6>empty(attP2))
UAS-Dcr2;OK6-Gal4/+;UAS-mCherry-NLS/UAS-Rbp^{RNAi}(attP2) (abbr. OK6>Rbp^{RNAi}(attP2))
UAS-Dcr2;OK6-Gal4/+;UAS-mCherry-NLS/UAS-unc-13^{RNAi}(attP2) (abbr. OK6>unc-13^{RNAi}(attP2))
w^{1118};OK6-Gal4/(attP40);UAS-mCherry-NLS/+ (abbr.OK6>empty(attP40))
w^{1118};OK6-Gal4/UAS-Rbp^{RNAi}(attP40);UAS-mCherry-NLS/+ (abbr.OK6>Rbp^{RNAi}(attP40))

Removing Unwanted Variation with Housekeeping Genes

The effectiveness of the removal of unwanted variation with housekeeping genes between RNA-seq libraries from the test data set was compared to unnormalized data, UQ normalized data, and UQ normalized data with empirical control genes using the RUVSeq package (ver 1.14.0, Risso et al., 2014). Empirical control genes were identified by a first-pass DE analysis and selecting the 500 least significant DE genes, as determined by edgeR *p*-values for UQ-normalized data.

Unwanted variation was estimated using the log-linear regression model described in Risso *et al.*:

$$logE[Y|W,X,O] = W\alpha + X\beta + O$$

Y is an $n \times J$ gene-level count matrix, where n represents the samples in the data set and J represents the genes expressed. X is an $n \times p$ matrix representing the p covariates of wanted variation (i.e. biological variation), W is an $n \times k$ matrix representing unwanted variation, and O is a $n \times J$ matrix of offsets. The α and β terms are unobserved coefficients that represent the influence of a factor on a given gene. In the case of β, this factor is the biological covariates of

interest, p, whereas for α, this factor is k, the unobserved, unwanted factors of variation. If one identifies a set of negative control genes, J_c, which are not differentially-expressed between biological conditions, the equation above simplifies to:

$$logE[Y_c|W, X, O] = W\alpha_c + O_c$$

W can be estimated as described in Risso et al., and substituted into the first equation to estimate α and obtain normalized read counts ($W\alpha$). This process was performed with either empirical controls or housekeeping genes identified in the previous section representing J_c.

Evaluation Criteria

We measure the effectiveness of normalization procedures using the following methods:

1. Principal Component Analysis: Effectiveness of the removal of unwanted variation was qualitatively assessed by calculating the first two PCs and plotting each library in low-dimensional space. Effective normalization should reduce the influence of technical effects on each sample in PCA space.

2. Relative Log Expression: The relative log expression (RLE) for each gene was determined by taking the log-ratio of the counts for each gene to the median counts of that gene across all samples. Effective normalization should center the distribution of RLE of all genes within a given sample about zero. RLE distributions with means far from zero could indicate the presence of technical effects or libraries of poor quality.

3. Mean-Difference Analysis: Mean-difference analysis compares the average expression of a gene to log fold-change in expression between two groups of samples. Samples of the same biological origin should have heteroscedastic distribution, as genes with low average read counts should have greater log fold-change between samples than genes with high read counts. A loess-fit of the mean-difference trend of a well-normalized data set should be centered about zero.

4. Differential Expression Analysis: DE genes were identified using the negative binomial GLMs of the edgeR package (ver 3.22.5, Robinson et al., 2010) and the DESeq2 (ver 1.20.0, Love et al., 2014). RUVg normalization was performed by supplying the W matrix determined using either the housekeeping genes or empirical controls in the design matrix for DE analysis. DE genes were determined from a likelihood ratio test (edgeR) or a Wald test (DESeq2) for the effect of interest. A gene is DE if the null hypothesis (that the difference in expression between the two groups is zero) was rejected with a false discovery rate of 0.05. Two batches of libraries of the same genetic background, in this case *OK6>empty(attP2)*, were subjected to each normalization procedure and then tested for DE genes using either edgeR or DESeq2. Adjusted p-values from DE testing were compared to a theoretical distribution. An ideal normalization method should have few DE genes between two different libraries of the same biological condition. To accurately compare p-values between edgeR and DESeq2, the negative binomial Wald tests were performed without independent filtering or applying a Cook's distance cutoff.

Code availability

Code used for all data analysis steps are available in a Github repository at https://github.com/cypranowska/dmel_housekeeping.

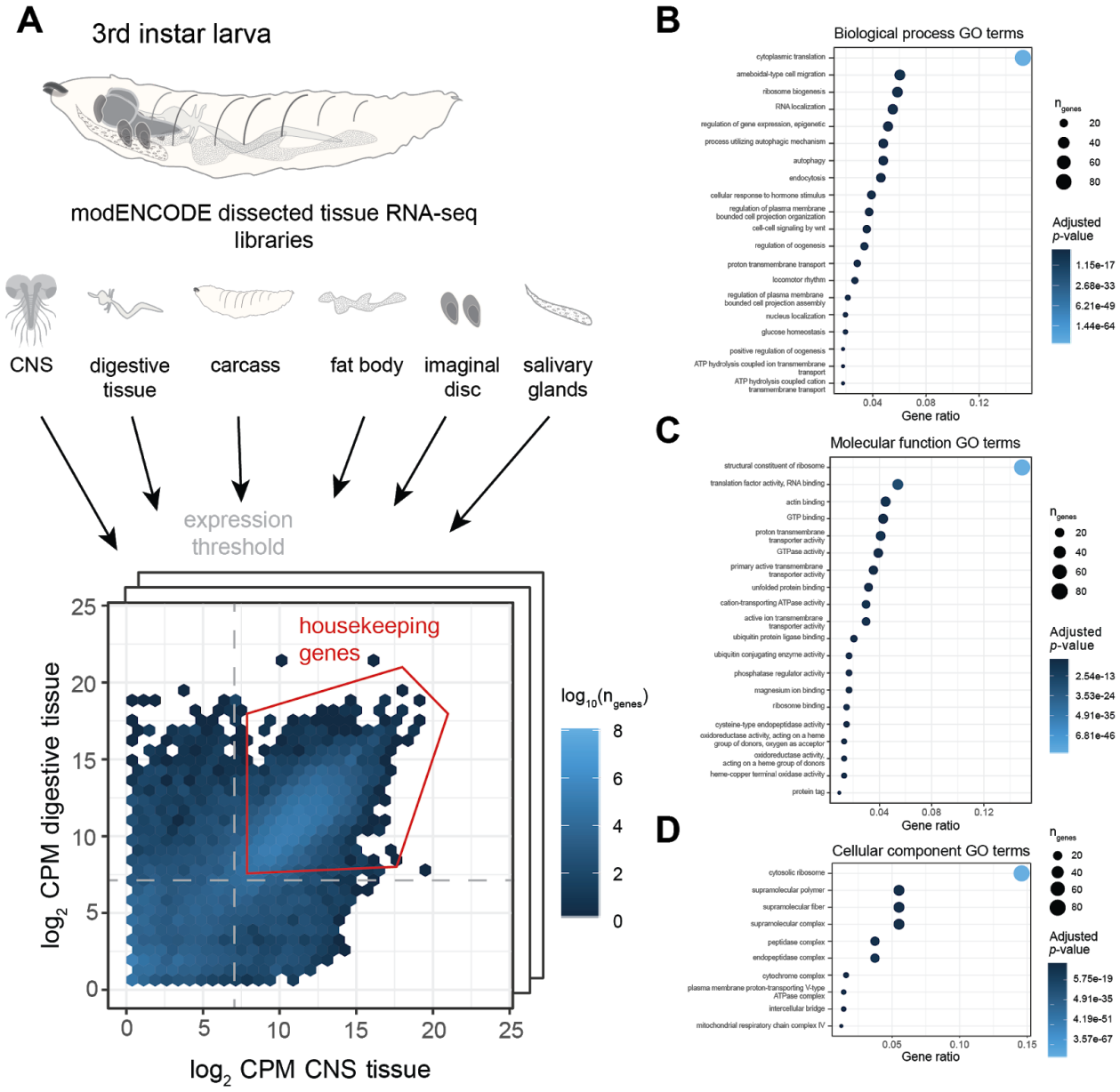

Figure 5.1) Selection and characterization of *Drosophila* housekeeping genes from modENCODE RNA-sequencing libraries. **A)** Scheme for identifying housekeeping genes. RNA-sequencing libraries from six different dissected tissues preparations were aligned to a reference genome and normalized. Genes detected with at least 1 CPM in all samples and an average expression of 2^7 CPM were selected as candidate housekeeping genes. The 600 genes with the lowest variance were selected for the final housekeeping gene set. **B-D)** GO term enrichment of housekeeping genes of the top 20 biological process (BP) terms (**B**), top 20 molecular function (MF) terms (**C**), and top 10 cellular component (CC) terms (**D**). Terms are ranked by their adjusted *p*-value and percentage of genes present in the GO term.

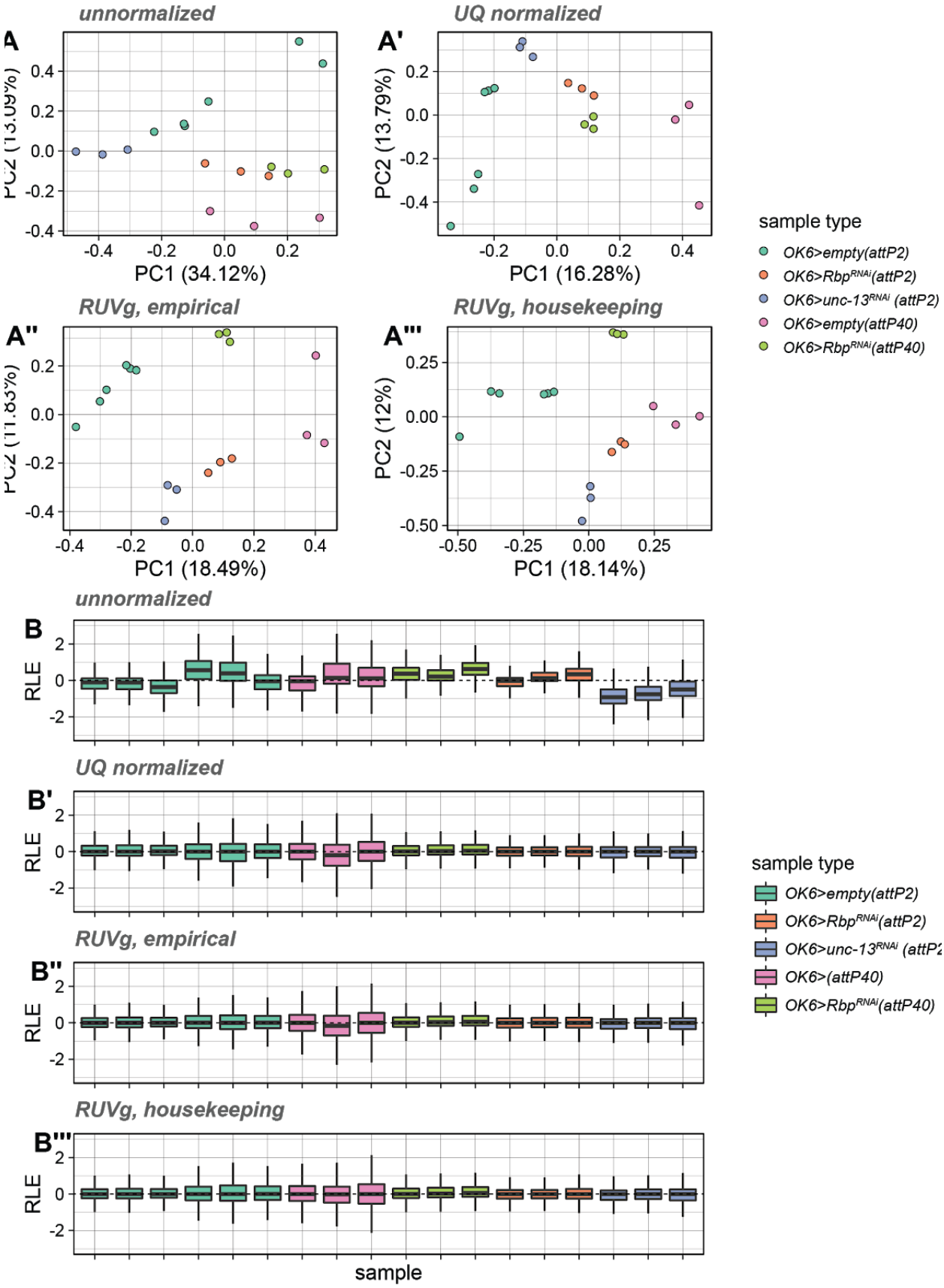
unnormalized
A
PC2 (13.09%)
PC1 (34.12%)
UQ normalized
A'
PC2 (13.79%)
PC1 (16.28%)
RUVg, empirical
A''
PC2 (11.83%)
PC1 (18.49%)
RUVg, housekeeping
A'''
PC2 (12%)
PC1 (18.14%)
sample type
OK6>empty(attP2)
OK6>Rbp^RNAi(attP2)
OK6>unc-13^RNAi (attP2)
OK6>empty(attP40)
OK6>Rbp^RNAi(attP40)
unnormalized
B
RLE
UQ normalized
B'
RLE
RUVg, empirical
B''
RLE
RUVg, housekeeping
B'''
RLE
sample
sample type
OK6>empty(attP2)
OK6>Rbp^RNAi(attP2)
OK6>unc-13^RNAi (attP2)
OK6>(attP40)
OK6>Rbp^RNAi(attP40)

Figure 5.2) Removal of unwanted variation (RUVg) with housekeeping genes identified in independent RNA-seq data sets performs as well as RUVg with empirical controls. **A-A'''')** PCA plots of unnormalized counts (**A**), upper-quartile (UQ) normalized counts (**A'**), RUVg with housekeeping genes (**A''**), and RUVg with empirical controls (**A'''**). **B-B'''')** Genewise relative-log expression (RLE) per sample of unnormalized counts (**B**), UQ normalized counts (**B'**), RUVg with housekeeping genes (**B''**), and RUVg with empirical controls (**B'''**) for each sample. The dotted line represents a relative log expression of zero.

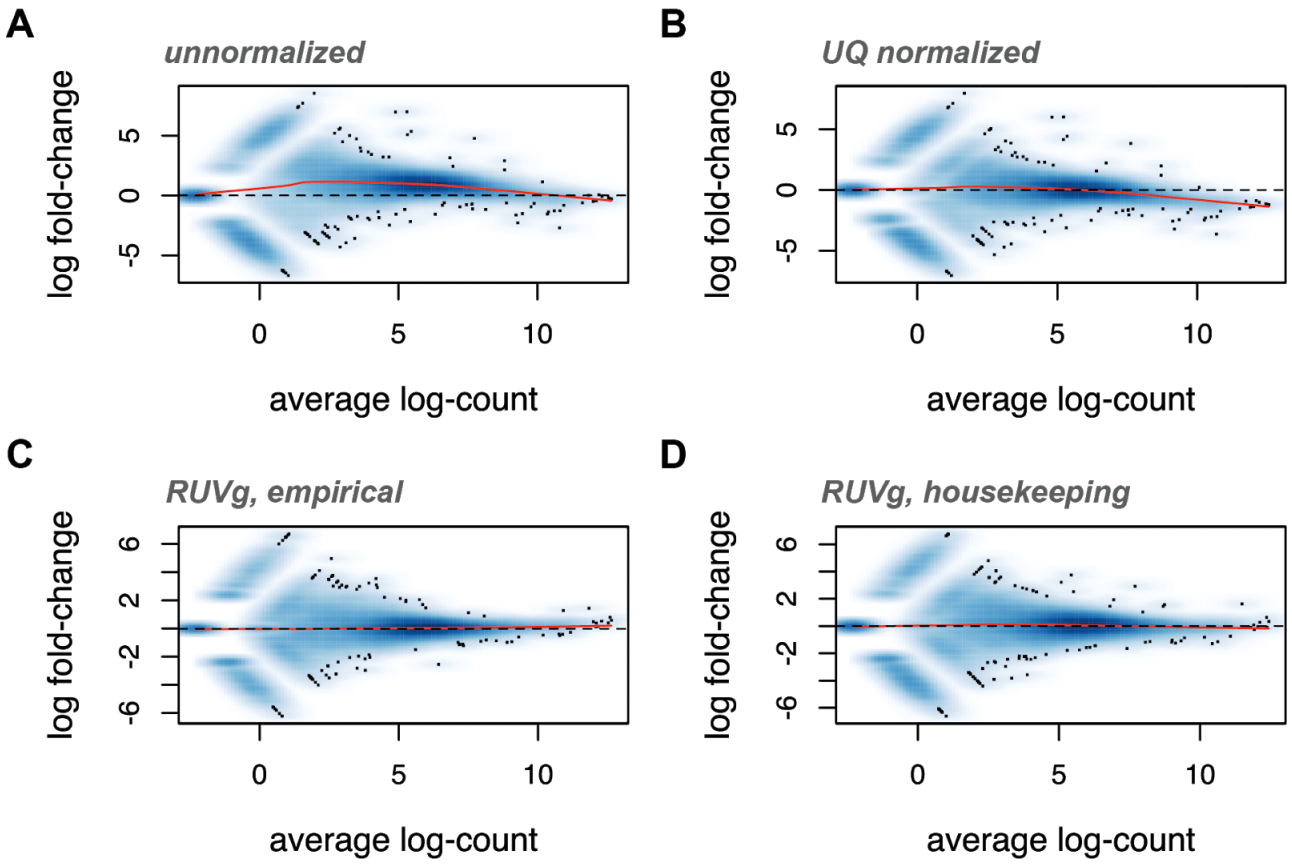

Figure 5.3) Removal of unwanted variation with housekeeping genes or empirical controls correct the mean-difference trend. **A-D)** Mean-difference plots of unnormalized (**A**), UQ normalized (**B**), RUVg-normalized with empirical controls (**C**), and RUVg-normalized with housekeeping genes (**D**) of two *OK6>empty(attP2)* control libraries. Dotted lines represent a $\log_2$-fold-change of zero. Red lines represent a loess fit of the mean-difference trend.

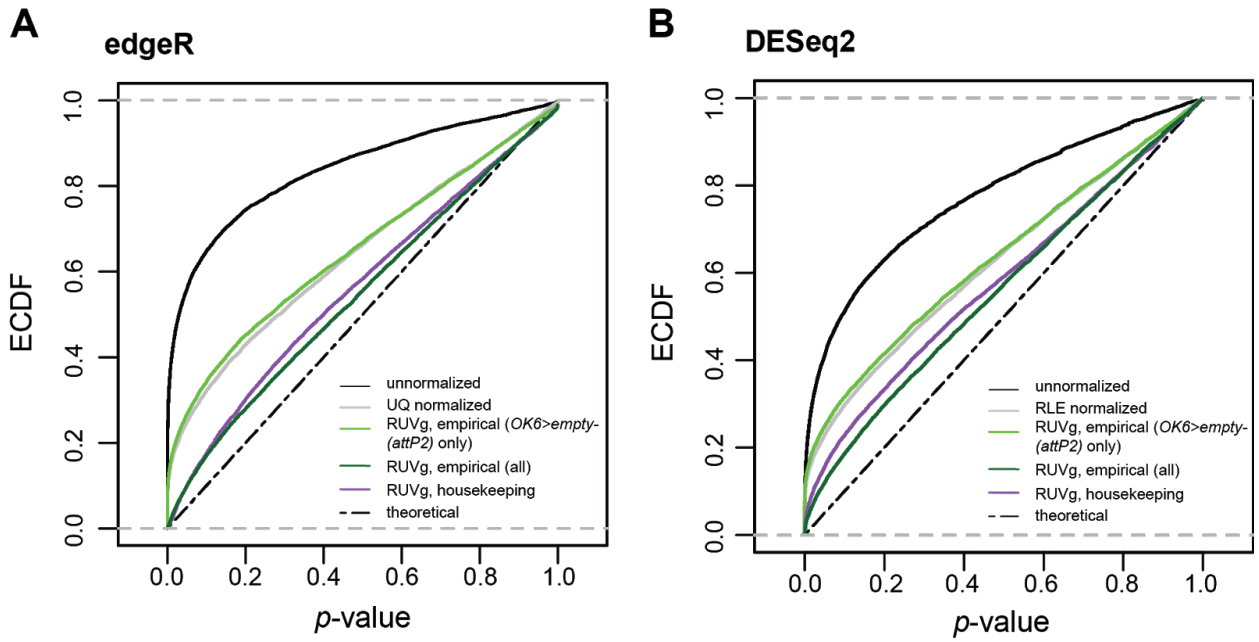

Figure 5.4) RUVg corrections with housekeeping genes and empirical controls from the full data set best control type I error compared to standard normalization routines. **A-B)** Empirical cumulative distribution of *p*-values from differential expression testing between two batches of *OK6>empty(attP2)* replicates for unnormalized counts (black), normalized counts (grey; UQ in **A**, RLE in **B**), and counts normalized using RUVg with either empirical controls identified comparing only *OK6>empty(attP2)* libraries (light green), all libraries (dark green), or housekeeping genes (purple) compared to the theoretical distribution (dotted line). Distributions were calculated using edgeR (**A**) or DESeq2 (**B**).

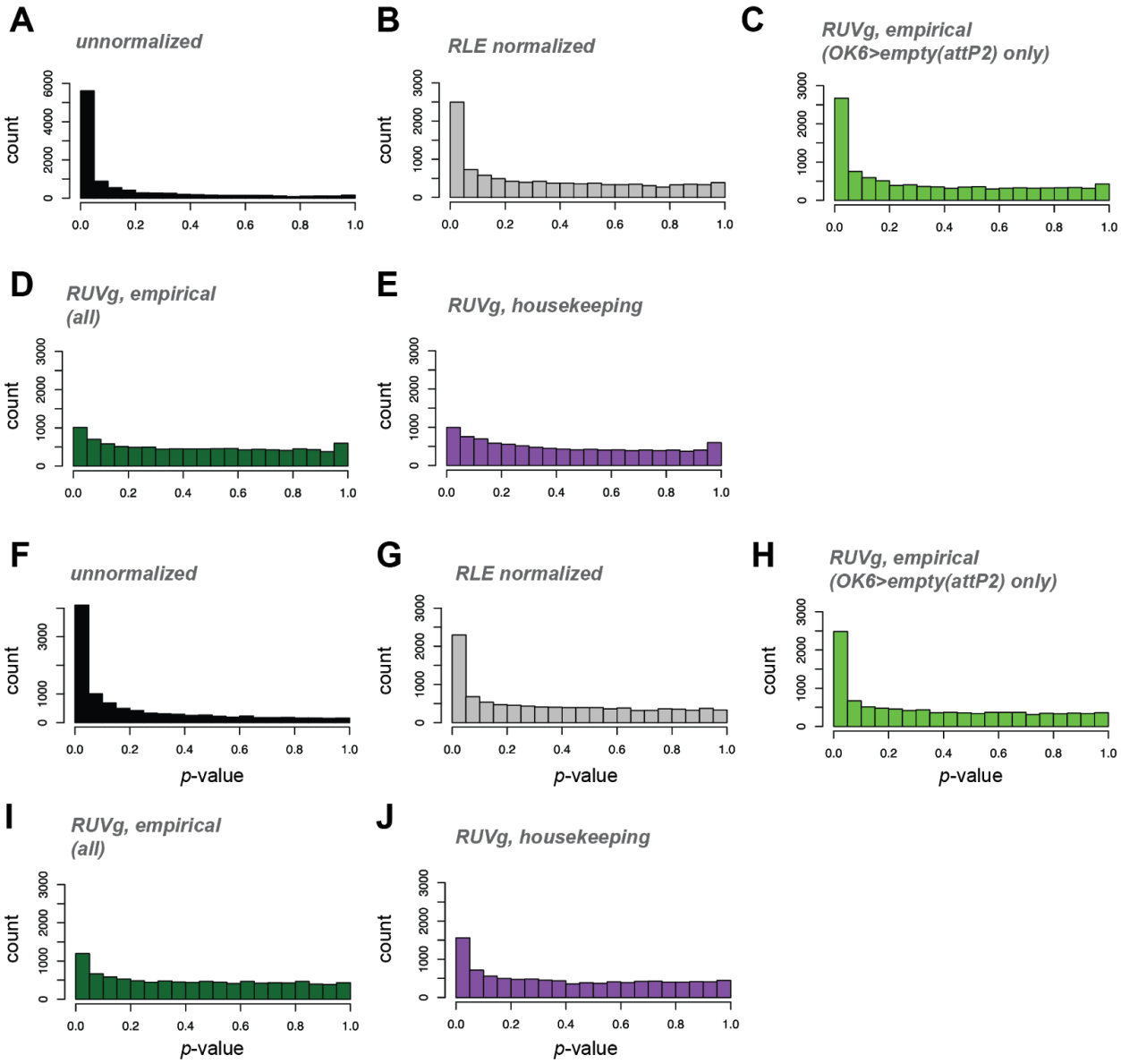

Supplementary Figure 5.1) *p*-value distributions of edgeR and DESeq2 DE testing by normalization method. **A-E)** *p*-value distributions of edgeR DE testing of unnormalized counts (**A**), UQ normalized counts (**B**), and counts normalized using RUVg with either empirical controls from *OK6>empty(attP2)* replicates only (**C**), empirical controls from the full data set (**D**), and housekeeping genes (**E**). **F-J)** *p*-value distributions of DESeq testing using the same methods described in **A-E**.

Supplementary Table 5.1 RNA-seq libraries of *Drosophila melanogaster* L3 dissected tissues

Tissue origin	SRR numbers	modENCODE accession
L3, wandering stage, carcass	SRR070426, SRR100269	modENCODE_4258
L3, CNS	SRR070409, SRR070410	modENCODE_4257
L3, digestive system	SRR070408, SRR100268	modENCODE_4259
L3, salivary glands	SRR070407, SRR070425	modENCODE_4262
L3, fat body	SRR070405, SRR070406	modENCODE_4260
L3, wandering stage, imaginal discs	SRR070392, SRR070393, SRR111884, SRR111885, SRR350962, SRR350963	modENCODE_4261

References

Anders, S., and Huber, W. (2010). Differential expression analysis for sequence count data. Genome Biol. *11*, R106.

Andrews, S. (2010). FastQC: a quality control tool for high throughput sequence data.

Ashburner, M., Ball, C.A., Blake, J.A., Botstein, D., Butler, H., Cherry, J.M., Davis, A.P., Dolinski, K., Dwight, S.S., Eppig, J.T., et al. (2000). Gene ontology: tool for the unification of biology. The Gene Ontology Consortium. Nat. Genet. *25*, 25–29.

Baker, S.C., Bauer, S.R., Beyer, R.P., Brenton, J.D., Bromley, B., Burrill, J., Causton, H., Conley, M.P., Elespuru, R., Fero, M., et al. (2005). The External RNA Controls Consortium: a progress report. Nat. Methods *2*, 731–734.

Boley, N., Wan, K.H., Bickel, P.J., and Celniker, S.E. (2014). Navigating and mining modENCODE data. Methods *68*, 38–47.

Bolger, A.M., Lohse, M., and Usadel, B. (2014). Trimmomatic: a flexible trimmer for Illumina sequence data. Bioinformatics *30*, 2114–2120.

Bolstad, B.M., Irizarry, R.A., Astrand, M., and Speed, T.P. (2003). A comparison of normalization methods for high density oligonucleotide array data based on variance and bias. Bioinformatics *19*, 185–193.

Bullard, J.H., Purdom, E., Hansen, K.D., and Dudoit, S. (2010). Evaluation of statistical methods for normalization and differential expression in mRNA-Seq experiments. BMC Bioinformatics *11*, 94.

Cancer Genome Atlas Research Network (2008). Comprehensive genomic characterization defines human glioblastoma genes and core pathways. Nature *455*, 1061–1068.

Caradec, J., Sirab, N., Keumeugni, C., Moutereau, S., Chimingqi, M., Matar, C., Revaud, D., Bah, M., Manivet, P., Conti, M., et al. (2010). "Desperate house genes": the dramatic example of hypoxia. Br. J. Cancer *102*, 1037–1043.

Celniker, S.E., Dillon, L.A.L., Gerstein, M.B., Gunsalus, K.C., Henikoff, S., Karpen, G.H., Kellis, M., Lai, E.C., Lieb, J.D., MacAlpine, D.M., et al. (2009). Unlocking the secrets of the genome. Nature *459*, 927–930.

Cole, M.B., Risso, D., Wagner, A., DeTomaso, D., Ngai, J., Purdom, E., Dudoit, S., and Yosef, N. (2019). Performance Assessment and Selection of Normalization Procedures for Single-Cell RNA-Seq. Cell Syst *8*, 315–328.e8.

Dillies, M.-A., Rau, A., Aubert, J., Hennequet-Antier, C., Jeanmougin, M., Servant, N., Keime, C., Marot, G., Castel, D., Estelle, J., et al. (2013). A comprehensive evaluation of normalization methods for Illumina high-throughput RNA sequencing data analysis. Brief. Bioinform. *14*,

671–683.

ENCODE Project Consortium (2004). The ENCODE (ENCyclopedia Of DNA Elements) Project. Science *306*, 636–640.

Gagnon-Bartsch, J.A., and Speed, T.P. (2012). Using control genes to correct for unwanted variation in microarray data. Biostatistics *13*, 539–552.

Gong, H., Sun, L., Chen, B., Han, Y., Pang, J., Wu, W., Qi, R., and Zhang, T.-M. (2016). Evaluation of candidate reference genes for RT-qPCR studies in three metabolism related tissues of mice after caloric restriction. Sci. Rep. *6*, 38513.

Gonorazky, H.D., Naumenko, S., Ramani, A.K., Nelakuditi, V., Mashouri, P., Wang, P., Kao, D., Ohri, K., Viththiyapaskaran, S., Tarnopolsky, M.A., et al. (2019). Expanding the Boundaries of RNA Sequencing as a Diagnostic Tool for Rare Mendelian Disease. Am. J. Hum. Genet. *104*, 466–483.

Grün, D., and van Oudenaarden, A. (2015). Design and Analysis of Single-Cell Sequencing Experiments. Cell *163*, 799–810.

Hansen, K.D., Irizarry, R.A., and Wu, Z. (2012). Removing technical variability in RNA-seq data using conditional quantile normalization. Biostatistics *13*, 204–216.

Hawrylycz, M.J., Lein, E.S., Guillozet-Bongaarts, A.L., Shen, E.H., Ng, L., Miller, J.A., van de Lagemaat, L.N., Smith, K.A., Ebbert, A., Riley, Z.L., et al. (2012). An anatomically comprehensive atlas of the adult human brain transcriptome. Nature *489*, 391–399.

Jiang, L., Schlesinger, F., Davis, C.A., Zhang, Y., Li, R., Salit, M., Gingeras, T.R., and Oliver, B. (2011). Synthetic spike-in standards for RNA-seq experiments. Genome Res. *21*, 1543–1551.

Kim, D., Paggi, J.M., Park, C., Bennett, C., and Salzberg, S.L. (2019). Graph-based genome alignment and genotyping with HISAT2 and HISAT-genotype. Nat. Biotechnol. *37*, 907–915.

de Kok, J.B., Roelofs, R.W., Giesendorf, B.A., Pennings, J.L., Waas, E.T., Feuth, T., Swinkels, D.W., and Span, P.N. (2005). Normalization of gene expression measurements in tumor tissues: comparison of 13 endogenous control genes. Lab. Invest. *85*, 154–159.

Li, J., Witten, D.M., Johnstone, I.M., and Tibshirani, R. (2012). Normalization, testing, and false discovery rate estimation for RNA-sequencing data. Biostatistics *13*, 523–538.

Liao, Y., Smyth, G.K., and Shi, W. (2014). featureCounts: an efficient general purpose program for assigning sequence reads to genomic features. Bioinformatics *30*, 923–930.

Ling, D., and Salvaterra, P.M. (2011). Robust RT-qPCR data normalization: validation and selection of internal reference genes during post-experimental data analysis. PLoS One *6*, e17762.

Love, M.I., Huber, W., and Anders, S. (2014). Moderated estimation of fold change and dispersion for RNA-seq data with DESeq2. Genome Biol. *15*, 550.

Lovén, J., Orlando, D.A., Sigova, A.A., Lin, C.Y., Rahl, P.B., Burge, C.B., Levens, D.L., Lee, T.I., and Young, R.A. (2012). Revisiting global gene expression analysis. Cell *151*, 476–482.

Mahoney, D.J., Carey, K., Fu, M.-H., Snow, R., Cameron-Smith, D., Parise, G., and Tarnopolsky, M.A. (2004). Real-time RT-PCR analysis of housekeeping genes in human skeletal muscle following acute exercise. Physiol. Genomics *18*, 226–231.

Mortazavi, A., Williams, B.A., McCue, K., Schaeffer, L., and Wold, B. (2008). Mapping and quantifying mammalian transcriptomes by RNA-Seq. Nat. Methods *5*, 621–628.

Oshlack, A., Emslie, D., Corcoran, L.M., and Smyth, G.K. (2007). Normalization of boutique two-color microarrays with a high proportion of differentially expressed probes. Genome Biol. *8*, R2.

Panina, Y., Germond, A., Masui, S., and Watanabe, T.M. (2018). Validation of Common Housekeeping Genes as Reference for qPCR Gene Expression Analysis During iPS Reprogramming Process. Sci. Rep. *8*, 8716.

Ponton, F., Chapuis, M.-P., Pernice, M., Sword, G.A., and Simpson, S.J. (2011). Evaluation of potential reference genes for reverse transcription-qPCR studies of physiological responses in Drosophila melanogaster. J. Insect Physiol. *57*, 840–850.

Qing, T., Yu, Y., Du, T., and Shi, L. (2013). mRNA enrichment protocols determine the quantification characteristics of external RNA spike-in controls in RNA-Seq studies. Sci. China Life Sci. *56*, 134–142.

Risso, D., Schwartz, K., Sherlock, G., and Dudoit, S. (2011). GC-content normalization for RNA-Seq data. BMC Bioinformatics *12*, 480.

Risso, D., Ngai, J., Speed, T.P., and Dudoit, S. (2014). Normalization of RNA-seq data using factor analysis of control genes or samples. Nat. Biotechnol. *32*, 896–902.

Robinson, M.D., and Oshlack, A. (2010). A scaling normalization method for differential expression analysis of RNA-seq data. Genome Biol. *11*, R25.

Robinson, M.D., McCarthy, D.J., and Smyth, G.K. (2010). edgeR: a Bioconductor package for differential expression analysis of digital gene expression data. Bioinformatics *26*, 139–140.

Suntsova, M., Gaifullin, N., Allina, D., Reshetun, A., Li, X., Mendeleeva, L., Surin, V., Sergeeva, A., Spirin, P., Prassolov, V., et al. (2019). Atlas of RNA sequencing profiles for normal human tissues. Sci Data *6*, 36.

The Gene Ontology Consortium (2019). The Gene Ontology Resource: 20 years and still GOing

strong. Nucleic Acids Res. *47*, D330–D338.

Thellin, O., Zorzi, W., Lakaye, B., De Borman, B., Coumans, B., Hennen, G., Grisar, T., Igout, A., and Heinen, E. (1999). Housekeeping genes as internal standards: use and limits. J. Biotechnol. *75*, 291–295.

Wang, Z., Lyu, Z., Pan, L., Zeng, G., and Randhawa, P. (2019). Defining housekeeping genes suitable for RNA-seq analysis of the human allograft kidney biopsy tissue. BMC Med. Genomics *12*, 86.

Wu, D., Hu, Y., Tong, S., Williams, B.R.G., Smyth, G.K., and Gantier, M.P. (2013). The use of miRNA microarrays for the analysis of cancer samples with global miRNA decrease. RNA *19*, 876–888.

Yang, Y.H., Dudoit, S., Luu, P., Lin, D.M., Peng, V., Ngai, J., and Speed, T.P. (2002). Normalization for cDNA microarray data: a robust composite method addressing single and multiple slide systematic variation. Nucleic Acids Res. *30*, e15.

Yu, G., Li, F., Qin, Y., Bo, X., Wu, Y., and Wang, S. (2010). GOSemSim: an R package for measuring semantic similarity among GO terms and gene products. Bioinformatics *26*, 976–978.

Yu, G., Wang, L.-G., Han, Y., and He, Q.-Y. (2012). clusterProfiler: an R package for comparing biological themes among gene clusters. OMICS *16*, 284–287.

Zhou, Z., Cong, P., Tian, Y., and Zhu, Y. (2017). Using RNA-seq data to select reference genes for normalizing gene expression in apple roots. PLoS One *12*, e0185288.

Concluding Remarks

This dissertation has surveyed the transcriptional landscape of *Drosophila* type I MNs using RNA-sequencing at the single-cell resolution and in bulk. The major contributions of this dissertation are: (1) Knockdown of core active zone components results in a presynaptic homeostatic compensatory mechanism that increases activity by altered voltage-gated K+ channel expression; (2) Presynaptic homeostatic potentiation is induced by a commonly-used transgenic fly line bearing a mutation in the *Msp300* gene, and results in altered expression of cell-adhesion molecules known to directly regulate vesicular release; and (3) Transcriptional diversity in type I MNs is dominated by temporal identity and is correlated with cell-adhesion molecule expression and activity-regulated genes.

We have developed a two-pronged approach combining the granularity of functional experiments with the exploratory power of RNA-sequencing. These methods have laid the groundwork for investigating other homeostatic processes involving long-term changes in gene expression, and such a framework can also be used to study neurodevelopmental, psychiatric, and neurodegenerative disorders featuring synaptic dysfunction. The future is bright in the field of synaptic physiology. As the integration of single-cell RNA-sequencing, electrophysiology methods, and superresolution microscopy of neural tissues matures, we will be able to appreciate the remarkable resilience of the neuron in ways that seemed impossible in bygone years.